UNIVERSITÀ
DEGLI STUDI
DI TRIESTE

UNIVERSITÀ DEGLI STUDI DI TRIESTE

XXXV CICLO DEL DOTTORATO DI RICERCA IN

SCIENZE DELLA TERRA, FLUIDODINAMICA E MATEMATICA.
INTERAZIONI E METODICHE

URBASIS-EU project (H2020-MSCA-ITN-2018, 473 grant number 813137)

Innovative approach for soil-structure interaction assessment

Settore scientifico-disciplinare: GEO/10 GEOFISICA DELLA TERRA SOLIDA

DOTTORANDA
Anna Maria Skłodowska A. M. Skłodowska

COORDINATORE
PROF. Stefano Maset Stefano Maset

SUPERVISORE DI TESI
PROF. Stefano Parolai

CO-SUPERVISORE DI TESI
PROF. Fabio Romanelli

CO-SUPERVISORE DI TESI
DR. Bojana Petrovic B. Petrović

ANNO ACCADEMICO 2022/2023

Abstract

The severe damage caused by the Ms 8.1 Michoaćan earthquake in Mexico City in 1985 highlighted the potential effects of soil-structure interactions (SSI) during strong ground motion. Although SSI studies have been carried out for years, so far little attention has been paid to the analysis of the polarization of the wavefield radiated from a vibrating structure into its surroundings, which is necessary for a better characterization of the seismic wavefield.

In the framework of this thesis, a novel approach for soil-structure interaction assessment based on waveform analysis is proposed. The approach is an innovative combination of deconvolution and polarization analysis of earthquakes recorded in a building and its surroundings. It allows the identification of the wave types of the radiated waves and the estimation of the energy of the radiated wavefield. The approach consists of four main steps: 1) evaluation of the dynamic behavior of the building, 2) deconvolution of the data recorded in the building and its surroundings using recording from the top of the building as the reference, 3) identification of the seismic phase associated with the energy transmitted from the building to the ground and reconstruction of the radiated wavefield, and 4) polarization analysis.

The proposed approach was tested using earthquake recordings from two experiments conducted in Italy. The first was carried out in 2019 in Matera, Italy, where a 7-story building and a nearby sports field were instrumented with three-component sensors. The second was conducted in 2022 at the test site in Piana di Toppo, Italy, where a single-degree-of-freedom (SDOF) structure was built to validate the approach in a simpler and more controlled environment.

The frequency band containing most of the vibrational energy of the building in the Matera building was estimated using the spectral ratio method. Then, the earthquake data were deconvolved using a sensor at the top of the building as a reference. In order to identify the seismic phases of the complex deconvolved wavefield, a simple analytical transfer function was calculated based on a simplified geometry of the test site. In the analytical deconvolved wavefield, a peak related to the energy transmitted from the building to its surroundings was identified. The reconstructed radiated wavefield was significant compared to the signal recorded in the surroundings of the building and its energy was calculated to be up to 59 % of the field signal. The polarization of the wavefield transmitted from the building to its surroundings was estimated as mostly linear in the analyzed frequency band. This could be explained, for example, by quasi-Rayleigh waves characterized by three planes in which radial and transverse components have a phase shift and the particle motion in the horizontal plane is elliptical.

The built structure of the Piana di Toppo experiment did not transmit shaking energy back to the ground. This prevented the successful identification of the types of waves radiated and the amount of related energy amount. The results suggest that such an experimental design may not be suitable for an SSI experiment.

The wavefield radiated from the building in Matera consisted of unconventionally polarized surface waves. Moreover, the energy radiated back from the building showed that the influence of the building on the ground motion was significant for the horizontal components in the considered frequency band. However, for the second experiment, no wavefield radiated from the built structure could be identified, and the results obtained in this thesis are limited to the recordings of only one earthquake. Therefore, more data need to be analyzed to confirm these observations. Further analysis with different data sets will be performed in the future to validate the proposed approach and the obtained results.

Glossary

Acausal part of the deconvolved wavefield Part of the deconvolved wavefield before the reference time $t = 0$ (i.e., $t \leq 0$).

Causal part of the deconvolved wave field Part of the deconvolved wavefield after the reference time $t = 0$ (i.e., $0 \geq t$).

Deconvolution approach Often called also deconvolution interferometry. Waveform approach for reconstructing waves propagating from one receiver to another. By deconvolving one recorded wavefield with another, the response between receivers is extracted.

Deconvolved wavefield The output of the deconvolution interferometry in the time domain.

Frequency Domain Decomposition (FDD) A frequency domain technique for the modal identification of output-only systems. The technique is based on the decomposition of the spectral density function matrix into a set of auto spectral density functions, each corresponding to a single degree of freedom system.

Power Spectral Density (PSD) matrix Describes the power distribution of the signal over the frequency. In the frequency domain, this is given by the square of the magnitude after the Fourier transform of the input signal.

S-transform Also known as Stockwell transform is a time-frequency spectral localization that combines elements of short-time Fourier transform and wavelet transform. In S-transform, the width of the analyzing window scales inversely with frequency.

Single degree of freedom system (SDOF system) A system for which only a single coordinate described by a single differential equation is required to completely specify the configuration of the system.

Site-city interaction (SCI) Interaction between the whole city and the soil.

Soil-structure interaction (SSI) Interaction between built structures (e.g., buildings) and the soil.

Spectral ratio method A method used for identification of the resonant frequency of a structure based on the spectral division of the same components of different sensors. In buildings, the spectra of the recording on different floors are divided by the spectra of the recording from the bottom.

Structure-soil-structure interaction (SSSI) Interaction between adjacent buildings and the soil.

Transfer function A mathematical function that theoretically models the system's output for each possible input.

Acknowledgements

First, I would like to thank my supervisor Stefano Parolai for the opportunity of doing this PhD, for his guidance and support, and for his encouragement to pursue my own research interests. I would also like to thank my co-supervisors Fabio Romanelli, Bojana Petrovic and Dimitirs Pitilakis for their support and helpful comments and suggestions throughout the duration of my PhD.

I would like to thank my dear friends and colleagues from the URBASIS-EU ITN. It was a truly amazing experience to be part of such a project (thanks Philippe!) and that we made the most of it, even in the times of Covid. Not only did the project allow me to develop as a researcher, but I also had the opportunity to meet amazing people and make great friendships. Chiara, thank you so much for all your help, both on a professional and personal level. I am so grateful to have met you and to be able to call you my friend. I enjoyed so much working with you and I really hope we will have more opportunities in the future. Thank you, Sri, for the great time we spent together and for letting me experience Milano-da-bere with you. Thank you, Karina, for great walking tours, for letting me be your roomie and for making me believe that the big-fat-cat exists. And to all the other ESRs I did not mention by name, but I am so glad we had shared moments and experiences during this PhD.

But most of all, I want to thank my family and friends who have always supported me on this journey. Thank you so much Amo and Jonny for being there for me in the most difficult moments and patiently listening to my (rare) complaints. Thank you Deniz and Selen for your friendship and for the cat-swap, that saved me so many times. Thank you, Sam, Gal, Lorenzo for the wonderful time we spent together. Thank you, Wiczi, for the long-lasting friendship that has survived the greatest distances, and your constant support and visits wherever I moved. Thank you, Maja, Maryjka and Ania, for all the nice chit-chats, visits, and support during these three years. Thank you, Daniel, for the development of this friendship that no one expected, but ended up being so important for me! Thank you, Babciu, for the weekly calls and for checking up on me. And thank you, Tato, for all the support even from the far away. And Oskarq, without your daily morning dose of motivation, who knows if I would make it! And last but not least, thank you, Karl, for making the last few years definitely extraordinary.

Contents

Chapter 1

Introduction

1.1 Overview

In densely populated urban areas in seismic-prone regions, earthquakes are one of the most significant natural hazards which can have a tremendous impact on the urban built environment and cause potential human and economic losses (e.g., De Risi et al., 2019; Silva et al., 2019; Reinoso et al., 2022). Therefore, mitigation of seismic risk, which describes the potential damage to a building, system, or other entity caused by such a hazard, in large urban areas is one of the main challenges in engineering seismology. Despite years of research, it is impossible to predict or prevent an earthquake, however, it is possible to mitigate its effects on society. One way to reduce potential losses is early warning systems (EWS), which have gained a lot of attention in seismology research. These systems alert people about waves generated by an earthquake before strong shaking arrives (e.g., Bindi et al., 2015a; Cremen and Galasso, 2020; Münchmeyer et al., 2021). Even though years of research have greatly improved the effectiveness of EWS to the point where in some regions of the world earthquake warning alerts have been successfully delivered to the public, in the best-case scenario EWS only provides information up to tens of seconds before shaking.

Currently, the most reliable way to reduce damage, particularly human losses, in urban areas is to improve the design of the buildings in seismically active areas. To do so, it is necessary to properly estimate the variability of ground shaking during an earthquake. Modifications of ground shaking are due to, for example, changes in local site conditions known as site effects (e.g., Seed et al., 1988, 1991; Parolai, 2012; Michel et al., 2014; Kaklamanos et al., 2021; Janusz et al., 2022) or interaction between built structures and the ground (e.g., Seed et al., 1988; Bard et al., 1996; Guéguen et al., 2000; Petrovic and Parolai, 2016), which is still not fully understood.

The severe destruction in Mexico City caused by the Ms8.1 Michoacán earthquake in 1985 (Singh et al., 1988) highlighted the importance of the interaction between built structures and soil in the case of strong ground motion. Based on the example of Mexico City, Wirgin and Bard (1996) demonstrated that in densely urbanized areas, the so-called "free-field" strong-motion recordings include the possible effects of the nearby located buildings. In one of the studies, conducted over 50 years ago, Jennings (1970) showed that a structure itself can have a significant impact on the surface ground motion in its surroundings. In his study, the author found that vibrations from the Millikan Library Building could still be observed at a distance of up to 10 km from the source. Since then, understanding the interaction between structures and soil has been of interest to many researchers, but the soil-structure interaction is still generally not taken into account for the seismic design of ordinary buildings (Fares et al., 2019).

The interactions between soil-structure (SSI), site-city (SCI), and structure-soil-structure (SSSI) in engineering seismology have been extensively investigated using analytical models (e.g., Paolucci, 1993; Guéguen et al., 2002), numerical simulations (e.g., Kham et al., 2006; Liang et al., 2013b; Isbiliroglu et al., 2013; Kumar and Narayan, 2017) and laboratory experiments (e.g., Pitilakis et al., 2008; Chandra and Guéguen, 2019). However, in the published literature regarding SSI, SCI, and SSSI research there are few examples involving real data, necessary to validate and supplement the aforementioned types of studies (e.g., Jennings, 1970; Wirgin and Bard, 1996; Guéguen and Bard, 2005; Parolai et al., 2005; Petrovic and Parolai, 2016; Petrovic et al., 2018).

Although SSI and SCI studies have been performed for years, analysis of the polarization of the wavefield radiated from a vibrating structure to its surroundings has gained limited attention so far. Even though the importance of polarization in earthquake data analysis has been underlined since Vidale (1986), there are only a few studies focused on SSI/SCI assessment concerning that matter. Recently, Kumar and Narayan (2019) modeled polarization of the incident S-waves in site-city effects, however, there are very few studies on the polarization of the wavefield radiated back from built structures to the ground (e.g, Chávez-García and Cárdenas-Soto, 2002). In one such study, Cardenas et al. (2000) concluded that, in the case of the Jalapa building in Mexico City, the polarization analysis of the wavefield radiated from the structure to the ground did not provide clear results due to the influence of the incident wavefield on the recorded motion. Therefore this area of research still requires more research to understand better the physics behind this important phenomenon.

1.2 Objectives and structure of the thesis

The main goal of the Ph.D. project was to identify and quantify the soil-structure interaction effects by using a new methodology for SSI assessment from a wave propagation point of view and to address the following open questions in the field of engineering seismology:

- Is it possible to estimate the impact of the building on the surroundings? How does a vibrating building interact with its surrounding? Is the footprint of the shaking, in terms of wave propagation, significant?
- Is it possible to retrieve the seismic wavefield radiated from a building to its surroundings in an urban area?
- What types of waves are released from a vibrating building?
- Can polarization analysis of the radiated wavefield improve the understanding of SSI/SCI effects?

- Could the characterization of the wavefield transmitted from a vibrating building into its surroundings be useful for improving the seismic design of structures in the future?

In the framework of this thesis, I propose a novel method for soil-structure interaction assessment based on waveform analysis. In contrast to other approaches proposed so far, the focus of this study is on the polarization analysis of a wavefield radiated from a building to its surroundings using the deconvolution approach. The approach enables the identification of wave types (e.g., P-, S-, Rayleigh and Love waves) and has an application for qualitative (types of radiated waves) and quantitative (energy) estimation of the wave types composing the radiated wavefield. The analysis to test the proposed approach is based on earthquake data coming from two experiments carried out in Italy.

Therefore, in this thesis, I:

- introduce and explain in detail the proposed approach,
- apply the new methodology to the real data:
  - I analyze data from an existing building and its surroundings instrumented during an experiment carried out in Matera (Italy),
  - I present the design and performance of the experiment in the Piana di Toppo test site (Italy) to obtain a second database in controlled and much simpler conditions
  - I analyze the data from the Piana di Toppo experiment.

The thesis is structured into seven chapters. After the Introduction containing the overview of the subject and the description of the objectives and structure of the thesis, in Chapter 2 I present the theoretical background of this study. I focus on the main topics necessary to understand the idea behind the proposed methodology, i.e.: in the first part, I describe the concept of wave propagation within a layered medium. Secondly, I give a brief explanation of the theory behind wave polarization. Next, I focus on the explanation of the methods used in engineering seismology for the estimation of the dynamic behavior of the building. Then, I present the concept and the state of the art of soil-structure interaction studies. Finally, I explain the concept of deconvolution used for engineering seismology studies.

In Chapter 3 I present the methods used in the proposed approach and the information that they provide. I explain in detail each step of the approach and its importance for obtaining the final goal of the analysis.

In Chapter 4 I describe the two test sites where the data used for this study was collected. The presentation of the test sites includes a description of the geology, the analyzed structures, and a description of the experimental setup and the data.

In Chapter 5 and Chapter 6, I present and discuss the results from the analyses of the two test sites. The organization of the results follows the methodology described in Chapter 3.

In Chapter 7 I conclude by presenting the major findings of the study. I discuss the potential limitations of this research and finalize the thesis with the outlook for further work.

The overall objective of this thesis is to improve the understanding of the interaction between the building and the soil during shaking, especially the relation between the building and the energy released to the ground caused by its vibration.

Chapter 2

Theoretical background

2.1 Seismic wave propagation through media

2.1.1 Body and surface waves

Ground shaking registered by an instrument such as a seismometer is a combination of different types of waves. The recorded energy radiated from a seismic source (e.g., an earthquake) is composed of body and surface waves. There are two types of body waves: P and S waves. The main difference is in the type of displacement they produce. In the case of P waves, the particle motion is parallel to the wave direction (compression and dilatation), and in the case of S waves, perpendicular (shear) (Figure 2.1). S waves have two components: SH (polarized in the horizontal plane) and SV waves (transverse to the wave propagation but in the vertical plane). In a $x - z$ plane (where z is vertical direction) P and SV waves form a coupled system, which gives rise to two components of displacement (x and z) (Figure 2.1b). SH wave contributes only to the y component of displacement, and therefore, is decoupled from P and SV waves.

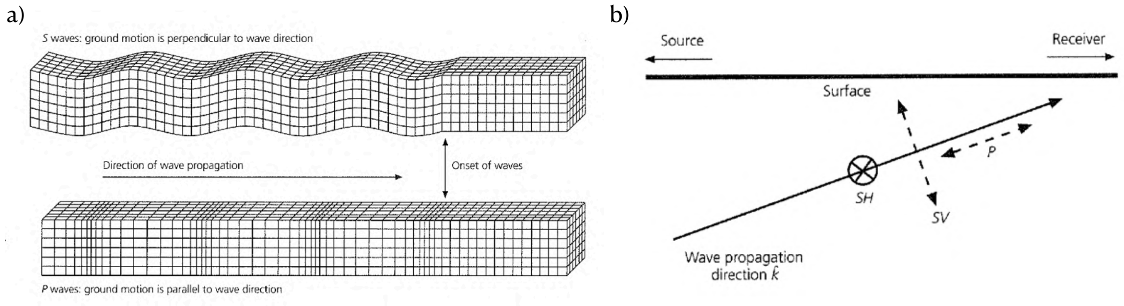

Figure 2.1: Displacement produced by S and P waves. a) Top: particle motion of S wave. Ground motion is perpendicular to the wave direction. Bottom: particle motion of P wave. Ground motion is parallel to the wave direction. Figure 2.4-3 on page 57 from Stein and Wysession (2003). b) Displacement fields for plane P and S waves. The P wave displacement is along the wave vector k. The S wave displacement is decomposed in two polarizations: SV and SH - both perpendicular to the vector k). Figure 2.4-4 on page 58 from Stein and Wysession (2003).

The other group of elastic wave types is surface waves, such as Rayleigh and

Love waves, whose energy is concentrated near the Earth's surface. Rayleigh waves are due to the interference of P and SV waves which can satisfy the free surface boundary conditions and do not interact with SH waves (Figure 2.2). In the case of the homogeneous halfspace, the particle motion of Rayleigh waves is in the radial (i.e. normal to the surface and parallel to the direction of propagation) and vertical planes moving with a retrograde ellipsoidal motion. Love waves are a result of the interaction of SH waves which are trapped near the surface. In contrast to Rayleigh waves, which can exist in a homogeneous medium, Love waves are generated only in a layered medium structure where the material velocity varies with depth. The particle motion of Love waves is perpendicular to the direction of propagation. The amplitude of both types of surface waves decays with depth.

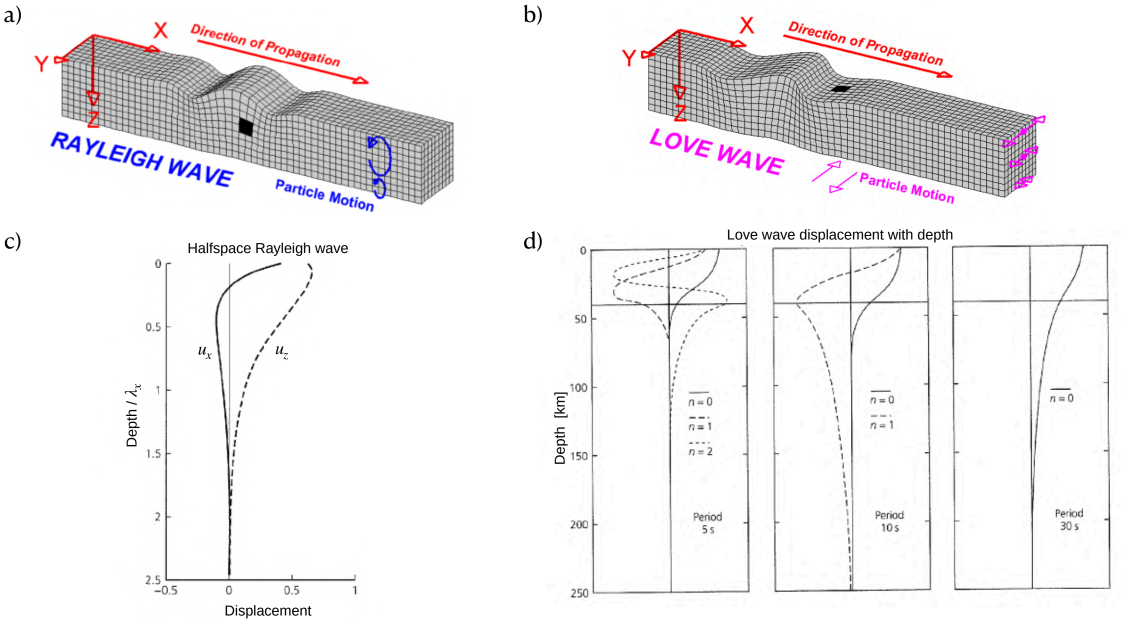

Figure 2.2: a) Particle motion of a Rayleigh wave in a homogenous halfspace. b) Particle motion of a Love wave in a layer over a halfspace. a) and b) modified from Braile, L. (2022). c) Variation with the depth of the radial (x) and vertical (z) components of displacement for a Rayleigh wave in a halfspace. Both components decay with depth. The plot is normalized by the horizontal wavelength. Figure 2.7-5 modified from Stein and Wysession (2003). d) Variation in displacement as a function of depth for Love waves in a layer over a halfspace of the modes (n) for the three periods (5 s, 10 s, 30 s). Figure 2.7-10 modified from Stein and Wysession (2003).

Based on Stein and Wysession (2003), when energy is released from a source such as an earthquake, seismic waves are generated and propagate through the Earth's structure which is neither homogeneous nor composed of uniform layers. If the analyzed region is small compared with the radius of Earth, the curvature of Earth can be neglected and it can be approximated as a laterally homogeneous halfspace. In the case of a stratified medium, velocities and densities vary with depth. In such a scenario, the Earth can be treated as finite thickness layers in the upper part, each with uniform properties (velocity, density) overlaying a halfspace. Additionally, if the energy source is far enough, the wavefront becomes flat enough to be locally approximated as a plane wave. Such an approximation assumes that displacement is constant orthogonal to the propagation direction and varies only in the direction of propagation.

When a wavefront approximated by a plane wave is passing through a layered medium, at the interface of each layer (i.e., at the junction of two horizontal layers), the energy is transmitted and/or reflected (Figure 2.3). Both transmitted and reflected waves move away from the interface, however, the difference is that the reflected wave stays in the same medium as the incident wave, and the transmitted one propagates on the other side of the boundary from the incident wave.

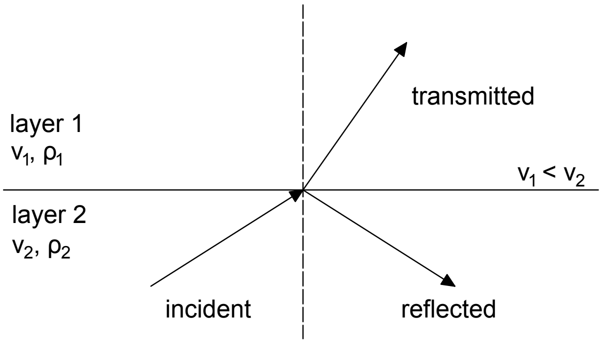

Figure 2.3: A schematic drawing of an incident wave propagating through two different solid layers with a transmitted and reflected part at the interface. v is the wave propagation velocity and ρ is the density of a layer.

How much of the energy is transmitted and how much is reflected depends on the acoustic impedance of each layer defined as

$$Z = \rho v \tag{2.1}$$

where ρ is the density and v is the wave propagation velocity of a layer. The impedance contrast between two layers is defined as the ratio between their impedance as follows

$$IC = \frac{\rho_1 v_1}{\rho_2 v_2} = \frac{Z_1}{Z_2}. \tag{2.2}$$

A large impedance contrast, IC, supports reflection while small IC favors the transmission of the energy. The amount of energy reflected at the interface for the incident wave propagating from medium 1 (characterized by ρ_1 and v_1) to medium 2 (characterized by ρ_2 and v_2) can be estimated from the reflection coefficient defined as

$$R_{12} = \frac{\rho_1 v_1 - \rho_2 v_2}{\rho_1 v_1 + \rho_2 v_2} = \frac{Z_1 - Z_2}{Z_1 + Z_2} = \frac{1 - IC}{1 + IC}. \tag{2.3}$$

The amount of energy transmitted at the interface can be estimated from the transmission coefficient defined as

$$T_{12} = \frac{2\rho_1 v_1}{\rho_1 v_1 + \rho_2 v_2} = \frac{2Z_1}{Z_1 + Z_2} = \frac{2IC}{1 + IC} = 1 - R_{12}. \tag{2.4}$$

In the case where the medium properties are interchanged, the polarity of the reflection coefficient reverses, i.e.: $R_{12} = -R_{21}$ and the transmission coefficients satisfy

$T_{12}+T_{21}=2$. In the case of the interface between two identical media, all the energy is transmitted (i.e. $T_{12}=1$) and nothing is reflected (i.e. $R_{12}=0$).

2.1.2 Quasi-Rayleigh and quasi-Love waves

The classical P, S, Rayleigh, and Love waves mainly describe the particle motion in an isotropic medium. However, when deformed, many rocks develop anisotropic elastic properties (Park and Yu, 1993). Anisotropy means that the seismic velocity depends on the direction of wave propagation and particle motion polarization (in the case of shear waves). In their study of the Earth's upper mantle, Park and Yu (1992) showed, using theoretical calculation, that anisotropic structure contributes to the occurrence of the quasi-Love and quasi-Rayleigh waves.

In an isotropic medium, the surface particle motion of Love waves is linear in the transverse direction. Tanimoto (2004) showed that in the case of an anisotropic medium, the particle motion is no longer linear, and due to the small vertical component with a phase lag, the motion is elliptical (Figure 2.4a). Additionally, they suggested that the particle motion in the horizontal plane is no longer strictly transverse and is not perpendicular to the direction of the wave propagation (however, in the case of weak anisotropy it should be close to 90°).

Similarly to the particle motion of Rayleigh waves in an isotropic medium, the quasi-Rayleigh waves can be also described by an ellipse (Figure 2.4b). The difference between the two wave types is that the plane of polarization of the quasi-Rayleigh waves deviates from the radial direction (Tanimoto, 2004). Yanovskaya and Savina (2004) demonstrated that, unlike the Rayleigh wave, the quasi-Rayleigh has three components - vertical, radial, and transverse. They suggested that due to the phase shift of the radial and transverse components, the particle motion of the quasi-Rayleigh waves is elliptical in the horizontal plane. Additionally, they showed that the quasi-Rayleigh wave has the same phase at all depths at 90 °azimuth. The phase varies with depth in an isotropic medium for all other azimuths. Yanovskaya and Savina (2004) concluded, that such observation can be interpreted as propagation of the wave in both the vertical and horizontal directions.

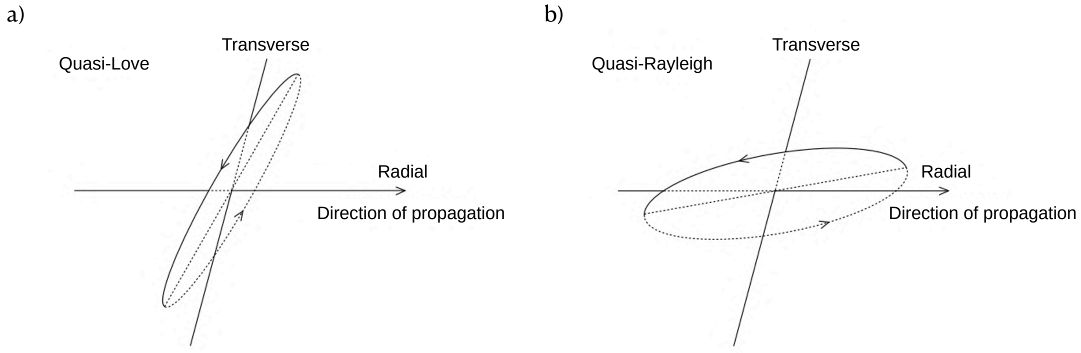

Figure 2.4: Particle motion trajectory of a) quasi-Love and b) quasi-Rayleigh waves. Modified from Tanimoto (2004).

According to Park and Yu (1993), toroidal modes of the Earth sum to form Love waves on the transverse component of motion, and spheroidal modes form Rayleigh waves on the vertical and radial components. However, due to the strong spheroidal-toroidal coupling, this separation is broken and quasi-Love waves manifest on the vertical and radial components, and quasi-Rayleigh on the transverse component. Park and Yu (1992) and Park and Yu (1993) suggested that in real data since the quasi-Love wave, in addition to radial components of motion, has a vertical component it can be easier distinguished from the principal Love wave than the quasi-Rayleigh waves from the principal Rayleigh waves.

2.2 Polarization ellipse parameters

Based on Fourier theory, a signal can be expressed as the superposition of sinusoidal oscillations in time. The Fourier amplitude and phase spectra of each sinusoid describe their contribution to the total signal. In their studies, Pinnegar (2006) extended this assumption to the three-component signal. They defined the three-component signal as the superposition of sinusoids oscillating in x, y, and z directions, which, when considered one frequency at a time, trace out elliptical motion in 3D space. Therefore, when analyzing one frequency at a time, this approach allows the representation of a signal as a superposition of the ellipses in 3D space. The elements of these ellipses, visually presented in Figure 2.5, uniquely describe the contribution of the f-th frequency to the total signal (Pinnegar, 2006). These are:

- a – the semi-major axis of the ellipse ($a \geq 0$),
- b – the semi-minor axis of the ellipse ($a \geq b \geq 0$),
- I – the inclination of the ellipse to the horizontal plane ($0 < I < \pi$),
- Ω – the azimuth of the ascending node (p in Figure 2.5) ($-\pi < \Omega < \pi$),
- ω – the angle between the ascending node (p in Figure 2.5) and the position of maximum displacement ($0 < \omega < \pi$),
- ϕ – the phase, measured with respect to the time of maximum displacement ($-\pi < \phi < \pi$).

The polarization analysis method proposed by Pinnegar (2006) is based on the analysis of three-component signals by means of the time-frequency Stockwell transform (S-transform) (Stockwell et al., 1996) - a time-frequency spectral localization method that is similar to the short-time Fourier transform, however, its windows are scaled with frequency. Each of the polarization ellipse parameters is calculated using real and imaginary parts of the spectra obtained using S-transform (S-spectra).

Using the decomposition of the signal proposed by Pinnegar (2006), it is possible to describe the whole signal by linear and circular parts. The circular part of the elliptical motion is defined by the semi-minor axis, and the linear part by the difference between the semi-major and semi-minor axes. Additionally, since each wave type has its own polarization pattern, the polarization ellipse parameters can be used to construct signal-adaptive time-frequency filters targeting specific types of particle motion that select certain types of waves (e.g., Rayleigh wave) or part of the ellipse (e.g., linear part of the polarization ellipse) for separate analysis (Pinnegar, 2006; Kazemnia Kakhki et al., 2020).

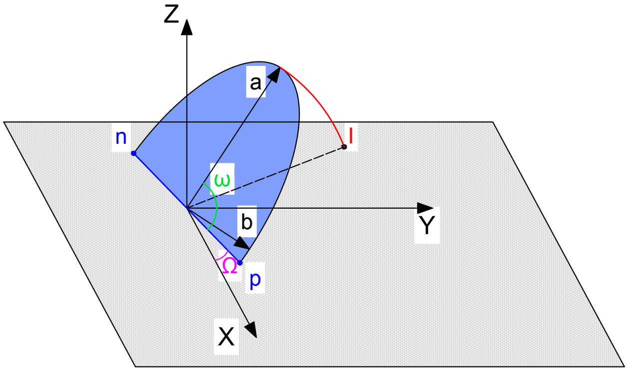

Figure 2.5: Graphic representation of the polarization ellipse parameters. a and b are the semi-major and semi-minor axes; Ω is the azimuth of the ascending mode; ω is the angle between the ascending node and the position of maximum displacement; I is the inclination of the ellipse to the horizontal plane. n and p are the nodes indicating the intersection of the ellipse with the horizontal plane.

2.3 Dynamic behavior of the building

For seismic engineering purposes, the dynamic response of a structure can be described by its vibration characteristics such as damping, modal shapes, and resonant frequencies (Clotaire et al., 2008). Damping decreases the vibration amplitudes by dissipating the energy. The modal shape is the deformation of a structure when it is vibrating at its resonant frequencies. Finally, the resonant frequency is the frequency at which the structure will tend to oscillate when subjected to certain external forces characterized by the same dominant frequency. Evaluation of the dynamic properties of a structure is known as modal analysis.

There are two main groups of methods used for the estimation of building dynamic behavior in engineering seismology studies. The first one, called frequency domain methods, is based on the estimation of the dynamic properties of a building using seismic data analyses in the frequency domain. The second is based on wave propagation analyses and is referred to as the waveform approach.

2.3.1 Frequency domain methods

Since it is expected that the resonant frequencies of a structure dominate the frequency content of the wavefield radiated from the structure to the ground (Petrovic and Parolai, 2016), in soil-structure interaction analysis, identification of the resonant frequency allows the definition of the frequency range over which this interaction might occur. There are different ways to estimate the resonant frequency of a building. In engineering seismology, the estimation of the resonant frequency can be done by using the Basic Frequency Domain (BFD) technique, also called peak picking (PP). As the name suggests, the PP method is based on simple signal processing using the Fourier transform and picking the peaks of the spectra. This method assumes that it is possible to estimate the frequencies of the well-separated modes directly from the power spectral density (PSD) matrix (e.g., Bindi et al., 2015b). This method however has limitations if the modes are close to each other and their detection might be difficult or biased. Additionally, if there is a soil-structure interaction effect, the picked frequency represents the soil-structure system and not purely the behavior of a building (Wolf, 1985), due to the shift of the fixed-base fundamental frequency, f_1, to the flexible-base frequency of the system, f_s (Stewart et al., 1999).

Another method widely used in literature for evaluation of the resonant frequencies of the building is the spectral ratio (SR) method (e.g., Guéguen and Bard, 2005; Parolai et al., 2005; Astorga et al., 2018; Skłodowska et al., 2021). The method is based on calculating the simple ratio in the frequency domain between the same component recordings collected at the top and bottom of the structure (Figure 2.6). The outcome of the spectral ratio is a transfer function of the analyzed structure and contains information about its resonant frequencies (e.g., Paolucci, 1993; Guéguen and Bard, 2005; Snieder, 2009). Similarly to the PP method, the resonant frequencies are picked from the peaks of the SR, however, the SR provides the fixed-base building response. The SR method can be used both with noise and earthquake data.

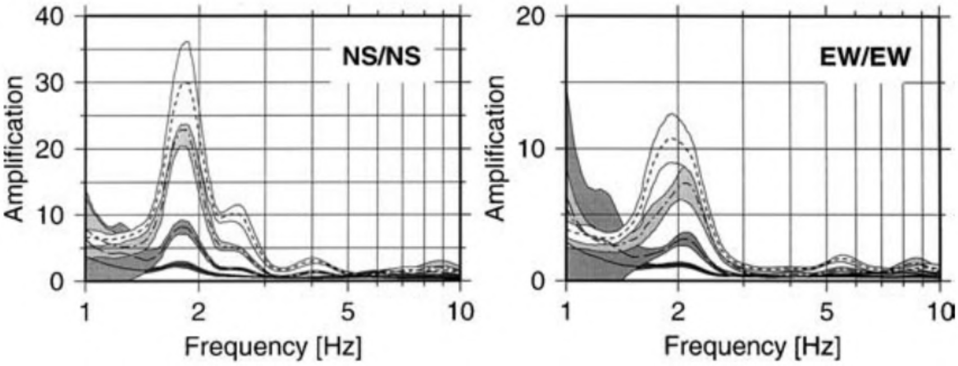

Figure 2.6: Example of the spectral ratio from Holweide Hospital used for resonant frequencies estimation. Modified afetr Parolai et al. (2005).

Since both PP and SR methods can be biased if the modes are close, Brincker et al. (2001) proposed another method called frequency domain decomposition (FDD) for the modal identification of output-only systems. In the FDD method, all three components of motion are considered together to estimate the mode shapes related to the resonant frequencies. First, the singular value decomposition (SVD) of the PSD matrix is calculated from noise recordings. By decomposing PSD into a set of auto spectral density functions, Brincker et al. (2001) showed that each corresponds to a single degree of freedom (SDOF) system.

The relationship of the unknown inputs and the measured output can be expressed as

$$G_{yy}(j\omega) = \bar{H}(j\omega)G_{xx}(j\omega)H(j\omega)^T \tag{2.5}$$

where $G_{xx}(j\omega)$ is the $(r \times r)$ power spectral density (PSD) matrix of the input, r is the number of inputs, $G_{yy}(j\omega)$ is the $(m \times m)$ PSD matrix of the responses, m is the number of responses, and $H(j\omega)$ is the $(m \times r)$ frequency response function matrix. The bar above H indicates the complex conjugate and the superscript T - matrix transpose.

The first step in the FDD method is the estimation of the PSD matrix. The estimated output of PSD $\hat{G}_{yy}(j\omega)$, known at discrete frequencies $\omega = \omega_i$, is defined as

$$\hat{G}_{yy}(j\omega_i) = U_i S_i U_i^H \tag{2.6}$$

where $U_i = [u_{i1}, u_{i2}, ..., u_{im}]$ is a unitary matrix of the singular vectors u_{ij}, and S_i is a diagonal matrix holding the scalar singular values s_{ij}. In the second step $\hat{G}_{yy}(j\omega)$ is decomposed by SVD.

If the k-th mode is dominating, the peak of this mode is dominating in the spectrum (as in Figure 2.7) and the first singular vector u_{i1} is an estimate of the mode shape ($\hat{\phi}$).

$$\hat{\phi} = u_{i1}. \tag{2.7}$$

The auto-PSD function of the corresponding SDOF system is defined by the corresponding singular value. This method enables the identification of both the natural frequency and the damping of a structure from the SDOF density function estimated near the peak of the PSD. By taking the SDOF PSD around the chosen peak and transforming it to the time domain by an inverse Fourier transform, damping can be estimated from crossing times and the logarithmic decrement of the corresponding SDOF autocorrelation function (Brincker et al., 2001). The FDD method has been widely used in the literature (e.g., Michel et al., 2008, 2010; Bindi et al., 2015b) for the modal identification of different structures.

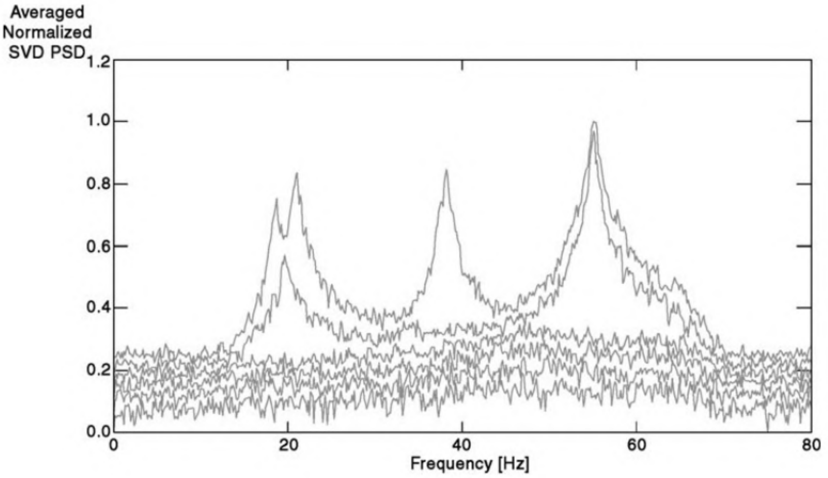

Figure 2.7: Singular values of the PSD matrix of the response. Figure 2 from Brincker et al. (2001)

.

2.3.2 Waveform approach

Estimation of the dynamic behavior of a building using the deconvolution method is a wave propagation approach and provides information on the structure decoupled from the soil. Estimation of the properties of a building using the waveform approach was proposed by Kanai (1965) and later popularized by Snieder and Şafak (2006) in a form of seismic interferometry by deconvolution (SIbyD). In the following years, SIbyD has become a widely used approach to evaluate the response of a building to an impulse input (Figure 2.8). With the assumption of the building behaving as a shear beam, the wave propagation velocity, β, and the distance between the position of the receivers, d, are related to the resonant frequency of a structure, f, by

$$f = \frac{\beta}{4d}. \tag{2.8}$$

The method characterizes the dynamic response of a fixed-base-type structure, assuming equivalent shear behavior and it is not applicable to low-rise buildings with a large plan.

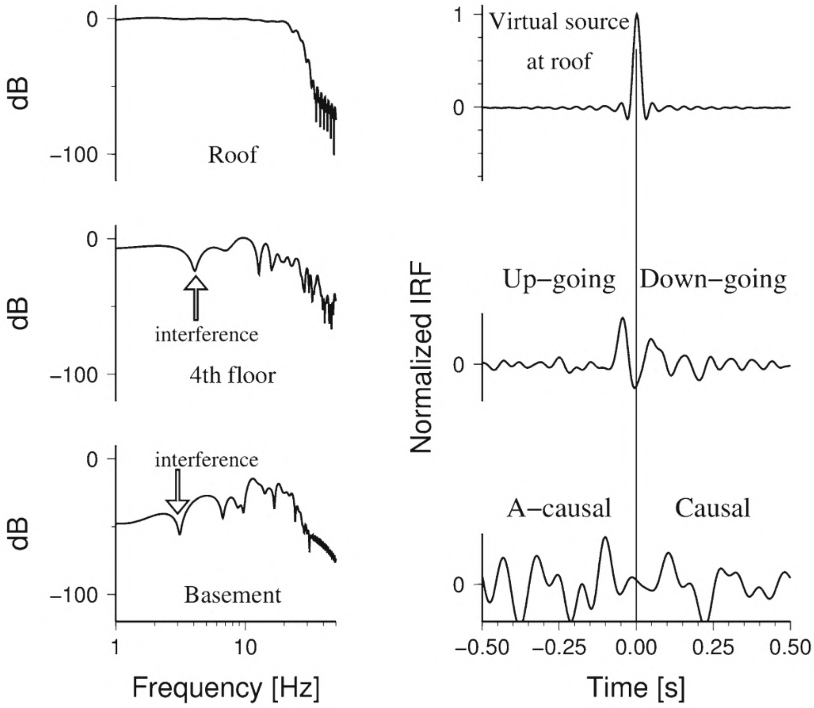

Figure 2.8: Example of the application of the waveform approach. In the given example, three signals coming from three different stations located on different floors were deconvolved by the reference signal coming from a sensor installed on the roof of the building. On the left deconvolved wavefield in the frequency domain. The throughs in the spectra caused by the negative interference of the propagating waves are indicated on the plots with arrows. On the right is the deconvolved wavefield in the time domain. The vertical line indicates the time 0. On the left from the vertical line, with a time below 0 is the acausal part of the wavefield, and on the right (with a time above 0) - is the causal part. Figure from Bindi et al. (2015b).

Nowadays, SIbyD is a standard procedure for estimating the dynamic response of a building and can be applied to both seismic noise (e.g., Nakata and Snieder, 2013; Bindi et al., 2015b; Mordret et al., 2017) and earthquake recordings (e.g., Nakata et al., 2013; Pianese et al., 2018; Guéguen et al., 2019; Skłodowska et al., 2021). Moreover, since under the SDOF assumption the fundamental frequency (and, therefore, the wave propagation velocity) is closely related to the structural stiffness (Guéguen et al., 2014; Rahmani and Todorovska, 2021), changes in the time delay of the peaks obtained from SIbyD can be used as a proxy for structural damage assessment (Todorovska and Trifunac, 2008; Skłodowska et al., 2021).

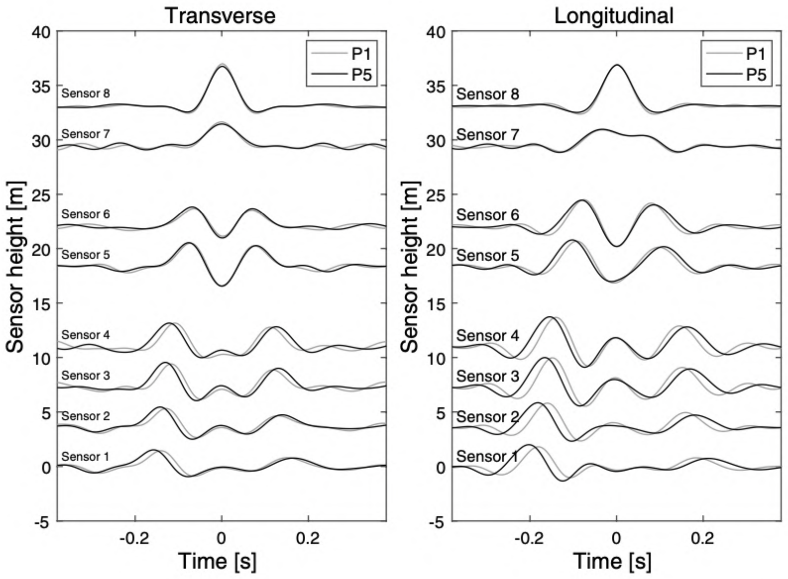

Figure 2.9: An example of SIbyD for structural damage assessment using data from eight sensors distributed along the vertical axis of a building. The change in the time delay of the peaks from two different periods (P1 and P2) is related to changes in the stiffness of the structure. Modified from Skłodowska et al. (2021)

.

2.3.3 Modes of a building

Modes of the dynamic behavior of a building can be either bending (flexural) or torsional. The behavior of the building subjected to an external load applied perpendicularly to its vertical axis is defined as the bending mode. When the building rotates around the vertical axis due to an applied torque it is called a torsional mode. When a structure is excited at multiple resonant frequencies, the dynamic behavior of the building is characterized by the mode shapes associated with each resonant frequency. The modal shapes of the resonant frequencies are a superposition of all contributing normal modes and they form the characteristic shape of the structure. An example of the first four modes of a building during the 2004 Santa Monica Bay earthquake calculated from horizontal-displacement recordings (Kohler et al., 2007) is presented in Figure 2.10.

2.4 Soil-structure interaction

As described by Snieder (2009), the motion of a structure is a combination of the excitation of the building (e.g, by an earthquake), the coupling of the building to the subsurface, and the mechanical properties of the building.

The evaluation of the joint response of the structure, the foundation, and the soil underlying and surrounding the foundation, to a specified free-field ground motion, is called seismic soil-structure interaction analysis (Stewart et al., 2012). The free-field ground motion refers to motions that are not impacted by structural oscillations or the scattering of waves at the foundation. In the theoretical case of a rigid structure built on rigid soil, the SSI effects are absent. Consequently, not only does the presence of the structure affect the free-field motion at the site, but it also changes

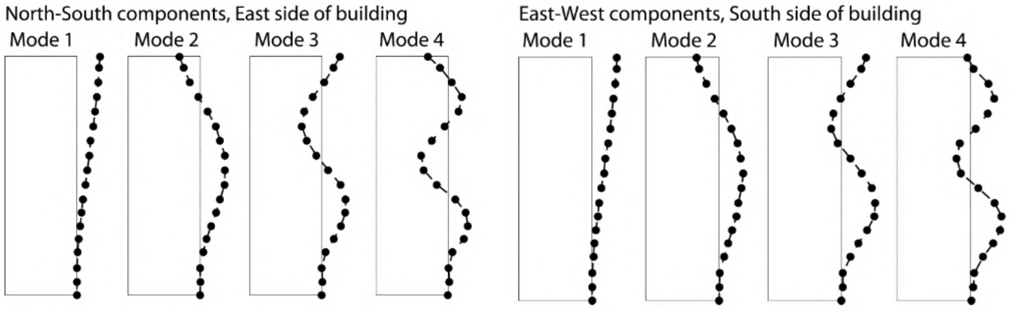

Figure 2.10: Mode shapes estimated from displacements recorded from the 2004 Santa Monica Bay earthquake. Filled circles represent actual sensor locations along the height of the building that contributed to the mode-shape measurements. Modified from Kohler et al. (2007)

.

the dynamic of the system from the fixed-base condition (Wolf, 1985; Stewart et al., 2012). This is one of the effects that constitute the soil-structure interaction phenomenon. Simply, soil-structure interaction is a phenomenon in which a structure interacts with the ground and the ground interacts with the structure (Kramer, 1996). SSI can have significant positive or negative consequences on seismic resilience and cannot be neglected. SSI can be analyzed from different perspectives such as geotechnical, engineering, or seismology. Since the focus of this thesis is on the wave propagation approach, the theoretical background on SSI presented in this chapter is mostly seismology-oriented.

Years of research showed that during an earthquake, the SSI effect is influenced by dynamic properties and the number of buildings, their separation, and their impedance contrast with respect to the soil (e.g., Chávez-García and Cárdenas-Soto, 2002; Kham et al., 2006; Isbiliroglu et al., 2015). The effect of SSI is more significant when the resonant frequency of the building is near the characteristics of the site (e.g., Guéguen et al., 2000; Liang et al., 2013a,b). Due to the SSI effects, it has been observed, that the resonance frequency of a system shifts to lower values (e.g., Liang et al., 2013a,b). SSI effects cause also modification of the wavefield due to the presence of the buildings, which can be significant (e.g., Jennings, 1970; Stewart et al., 1999; Guéguen et al., 2000; Chávez-García and Cárdenas-Soto, 2002; Guéguen and Bard, 2005; Petrovic and Parolai, 2016; Schwan et al., 2016; Petrovic et al., 2018; Chandra and Guéguen, 2019; Varone et al., 2020).

Some studies showed that the amplitude of the seismic ground motion in a city is strongly reduced when the fundamental frequencies of buildings and soil match (e.g., Semblat et al., 2008). However, many authors suggested that, in the case of a seismic event, the buildings may be not only considered as victims of the event but, since they modify seismic ground, also as part of the seismic hazard (e.g., Wirgin and Bard, 1996; Guéguen et al., 2000).

2.4.1 Numerical modeling approach

SSI can be studied using many different approaches. One such approach is numerical modeling. By analyzing SSI using numerical modeling, researchers can test the influence of different parameters and different geometries. Additionally, the constant development of technology decreases the computation time of evermore complex analyses. However, for the numerical simulations, usually simplified models, which might not adequately represent reality, are used. Additionally, even though researchers might model infinite setups for SSI analysis using numerical modeling, it is not always possible to validate the obtained results against real data.

Since it is possible to analyze multiple setups, the analyses using numerical modeling can study the seismic response of the clusters of buildings, their effects on the ground motion, or the impact of individual buildings on the soil and other structures (e.g., Wirgin and Bard, 1996; Guéguen et al., 2000; Guéguen et al., 2002; Kham et al., 2006; Semblat et al., 2008; Isbiliroglu et al., 2015; Varone et al., 2020). Moreover, analysis of multiple parameters in the SSI studies allows the study of the influence of the dynamic characteristic of the site on the SSI effects using different e.g. different incident waves (e.g., Liang et al., 2013a,b).

2.4.2 Laboratory experiments

Analyses based on laboratory experiments, similar to numerical simulations, are effective in testing different scenarios at relatively low costs. They still are, however, based on simplified models and have constraints of non-linear scaling. Additionally, in SSI problems analyzed in a laboratory environment, due to the limited size of the container (e.g. using a centrifuge) the radiation damping cannot be realistically simulated.

In the experiments performed in the laboratory environment, usually a shaking table (e.g., Kitada et al., 1999; Pitilakis et al., 2008; Schwan et al., 2016) or a centrifuge (e.g. Chazelas et al., 2001; Pitilakis and Clouteau, 2010; Chandra and Guéguen, 2019) are used. In case of a lack of data coming from real buildings, such experiments can be used in addition to numerical models for the validation of the results obtained using both methods (Pitilakis et al., 2008). By performing laboratory tests, it is possible to induce significant SSI effects using strong ground motion (Pitilakis et al., 2008; Pitilakis and Clouteau, 2010; Chandra and Guéguen, 2019).

2.4.3 Analyses based on real data

To overcome the mentioned limitations of numerical modeling or laboratory experiments, researchers study SSI using real data. In addition to the numerical simulations, some studied the effects of vibrating structure on the free-field motion by using data coming from field experiments (e.g., Guéguen et al. (2000) at the Euro-Seistest located near Thessaloniki, Greece (Figure 2.11a) (Manos et al., 1995; Euro-Seistest, 1995)).

Real data for the SSI studies is collected either from existing buildings (e.g., Chávez-García and Cárdenas-Soto, 2002; Petrovic and Parolai, 2016; Petrovic et al., 2018) or structures built especially for the need of the study (e.g., Guéguen et al., 2000; Guéguen and Bard, 2005; Amendola et al., 2021). The input signal causing vibration of a structure can be either coming from seismic noise (e.g., Chávez-García and Cárdenas-Soto, 2002; Massa et al., 2010), active source (Guéguen and Bard, 2005; Amendola et al., 2021) or earthquakes (e.g., Guéguen and Bard, 2005; Petrovic and Parolai, 2016; Petrovic et al., 2018).

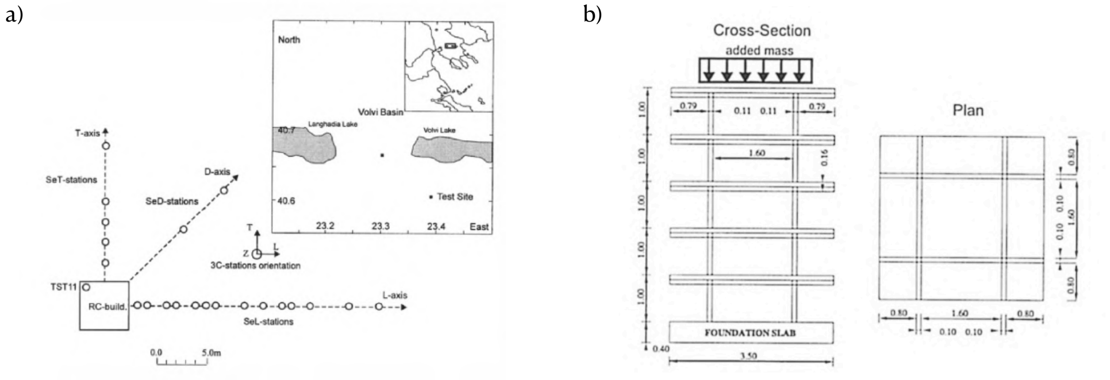

Figure 2.11: a) Location of the temporary network used for SSI study at Euro-Seistest facility in Volvi basin near Thessaloniki, Greece. The rectangle indicates the location of the building, and the circles indicate installed sensors. b) Multistory reinforced concrete building model constructed for the experiment at the Euro-Siestest test site. Figures reproduced from Guéguen et al. (2000).

2.4.4 Wave polarization in SSI studies

A basic polarization analysis is based on the rotation of the three-component motion to obtain the vertical, radial, and transverse components and their visual inspection (Vidale, 1986). In SSI studies, the polarization of the wavefield radiated from a vibrating structure has received little attention so far. Even though the importance of polarization aspects in seismic data analysis has been underlined for many years (e.g., Vidale, 1986) and has the potential to provide important information on the nature of the analyzed waves, it has gained limited attention in terms of SSI assessment.

Cardenas et al. (2000) analyzed particle motion polarization of recordings from the Jalapa building in Mexico City, Mexico, to identify the wavefield radiated from the structure to the ground. In their study, they observed that it is very difficult to identify SSI effects on the surrounding soil. They connected this observation with possible energy diffraction by the structure due to the SSI phenomenon. Additionally, merging with the incident wavefield propagating around the fundamental frequency of the soil made polarization analysis difficult. Therefore to perform the polarization identification, they filtered the data around the coupled system frequency, but despite this, the polarization analysis did not provide satisfying results.

Another approach was proposed by Kumar and Narayan (2019) who studied site-city interaction effects using numerical models with a focus on the analysis of the polarization of the incident S-waves. They observed that the spectral amplification at the top of a structure is more significant for the SV-wave than for the SH-wave.

Chapter 3

Methods

In the framework of this thesis, I propose a novel approach for estimating the effect of soil-structure interaction in terms of radiated wavefield. The proposed approach enables the identification of wave arrivals, the wave types (e.g., P-, S-, Rayleigh, and Love waves), and the estimation of their relative contribution to the wavefield radiated by the building to its surroundings. The basic assumptions for the suggested approach are the following:

- the recordings used for the analysis are earthquake data coming from an event located far enough away that the input can be assumed to be a vertically propagating wave,
- the earthquake data is coming from an instrumented building ideally with two sensors installed at the bottom and at the top of the building and at least one sensor installed in the surroundings of the structure at the surface.

The proposed approach is an innovative combination of deconvolution of the earthquake data from a building and its surroundings, application of constrained deconvolution for wavefield component separations, and polarization analysis for wavefield characterization. It consists of four major steps:

1. assessment of the dynamic behavior of the building,
2. deconvolution of the earthquake data recorded in the building and in the free field around it using recording from the top of the building as the reference,
3. identification of the phase related to the energy transmitted from the building to the ground, wavefield decomposition and energy estimation,
4. polarization analysis.

The major steps of the proposed methodology are presented in Figure 3.1 and shown schematically in Figures 3.2, 3.3, 3.4 and 3.5.

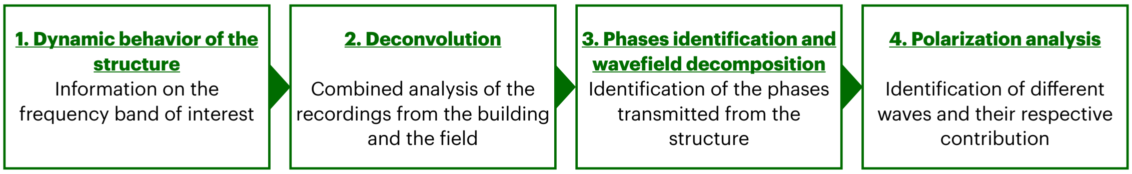

Figure 3.1: The general scheme of the major steps of the proposed approach.

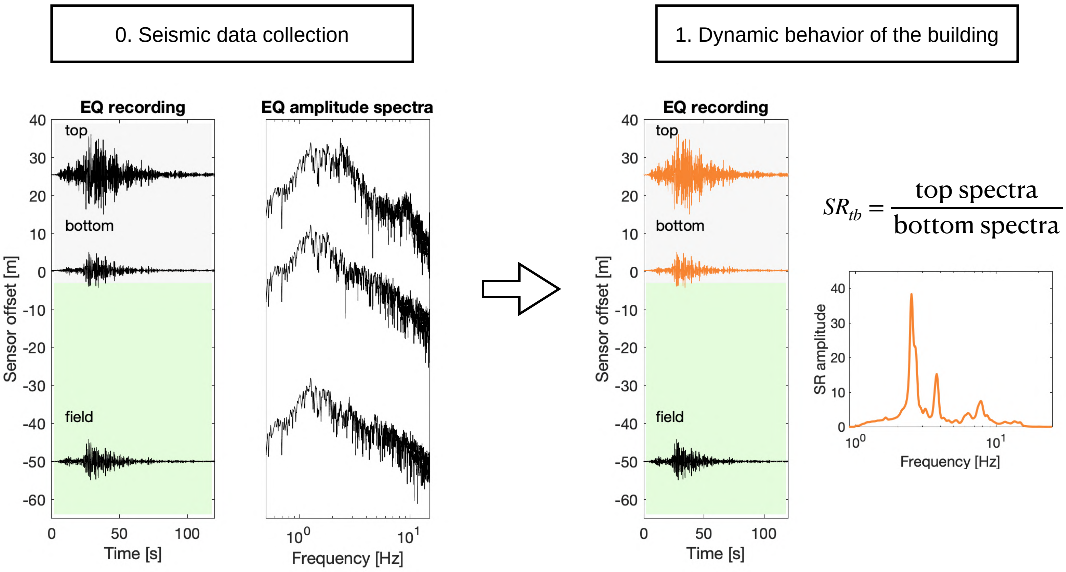

Figure 3.2: Scheme showing the steps of the methodology. Step 0. Seismic data collection: an example of the earthquake data recorded at the top and bottom of a building as well as in the field, as required for this analysis, and their corresponding Fourier amplitude spectra. Step 1. Estimation of the dynamic behavior of the building: the recordings from the top and the bottom of the building are used for the estimation of the frequency range where most of the vibrational energy of the building is located. Grey background: vertical distance in the building; green background: horizontal distance from the building

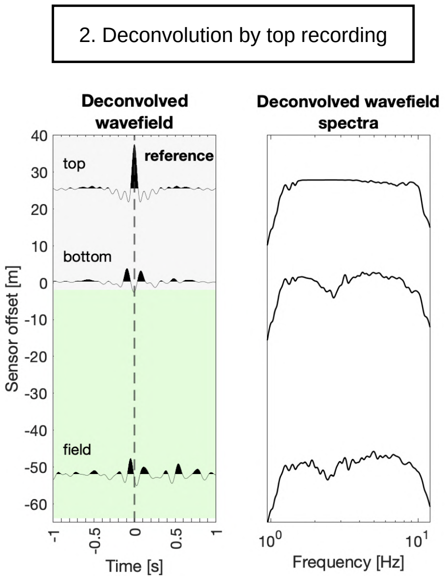

Figure 3.3: Step 2. Deconvolution of the recordings from the building and its surroundings using the recording from the top of the building as a reference. On the right, are the results in the time domain, and on the left are the corresponding amplitude spectra. Grey background: vertical distance in the building; green background: horizontal distance from the building

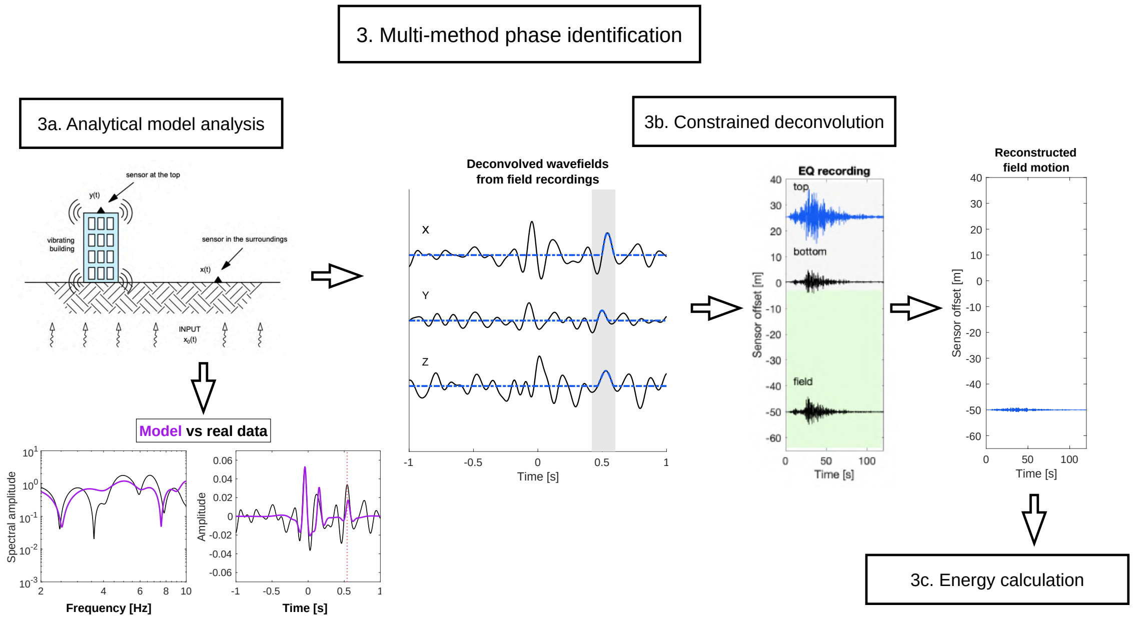

Figure 3.4: Step 3. Phase identification. In the first part (3a.), based on the analytical model fit in the frequency domain (left), the phases related to the energy radiated back from the building to the ground are identified in the time domain (right). In the second part (3b.), using the constrained deconvolution approach, the identified phases of the deconvolved wavefield are separated, and the field motion related to the transmitted energy is reconstructed by convolving the constrained spectra with the spectra of the recording from the top of the building (blue trace in the middle plot). The energy of the signal is then calculated as the integral of the power density spectrum (3c).

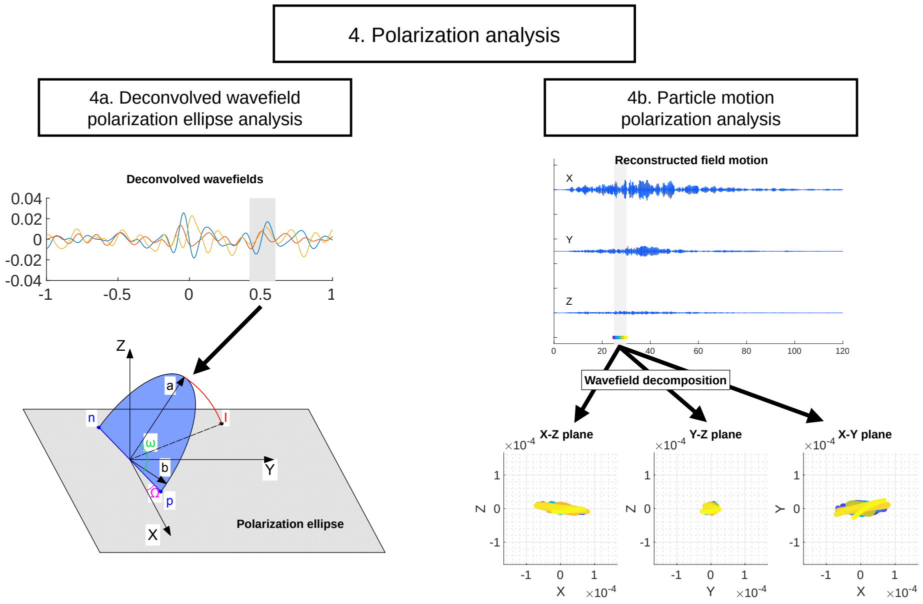

Figure 3.5: Step 4. Polarization analysis. It consists of two separate analyses. 4a is the analysis of the polarization ellipse parameters of the deconvolved wavefield. Using the S-transform of all three components of motion, the polarization ellipse parameters related to the selected phase in step 3. are extracted and analyzed. 4b is the analysis of the particle motion of the reconstructed wavefield radiated from the building to the ground based on the decomposition of the three components' time history into three planes of motion - radial, transverse and horizontal.

3.1 Dynamic behavior of the building

The frequency content of the wavefield radiated from the structure to the ground is expected to be dominated by the resonance frequencies of the building (Guéguen et al., 2000; Petrovic and Parolai, 2016). This step (Figure 3.2), therefore, provides information about the frequency band where most of the vibrational energy of the building is located, and which would be used for further analysis. Moreover, information about the resonant frequencies of the structure is important for the interpretation and validation of the results in the final stage of the analysis, if the radiated wavefield is indeed dominated by the resonance frequencies of the building.

As described in chapter 2, there are several ways to estimate the dynamic behavior of the structure. The spectral ratio method, where the quotient of the Fourier spectra of the same component recordings from sensors at the top of the building and those at the bottom, is sufficient to estimate the frequency band in which the possible interaction between a building and soil might be anticipated (Parolai et al., 2005). Therefore, due to its simplicity and the small amount of data (bottom and top) necessary to estimate the dynamic behavior of the building, this method is suggested for the first step of the proposed methodology.

In the case of the very close modes and availability of the noise recordings from the building, the FDD analysis could provide additional information about the dynamic behavior of the building, which could be useful for the interpretation of the results. Therefore, if there are available noise recordings necessary for the FDD analysis, it is recommended to perform this analysis as an additional step, however, it is not essential for the proposed methodology.

3.2 Deconvolution of the recordings from the building and the field

As a mathematical operation, convolution is a mathematical operation on two functions (f and g) that produces a third function ($f * g$) that describes how the shape of one is altered by the other. Deconvolution is the opposite operation of convolution, widely used in signal processing. Using the deconvolution method it is possible to recover the original signal after the application of a filter (convolution). The first application of the deconvolution approach to seismology research can be found in reflection seismology in the ”convolutional model” proposed by Enders Robinson and his colleagues in the 1950s. In the model they assumed that the recorded seismogram $s(t)$ is the convolution of an Earth-reflectivity function $e(t)$ and a seismic wavelet $w(t)$ from a point source, where t represents recording time

$$s(t) = (e(t) * w(t)) \tag{3.1}$$

Using the convolution theorem, it is possible to rewrite this equation in the Fourier domain as the product of those two functions

$$S(f) = E(f) \cdot W(f) \tag{3.2}$$

This operation as a method for seismic data analysis in engineering seismology has been widely popularized by e.g. Snieder and Şafak (2006). They proposed wave propagation analysis using a deconvolution approach to seismic data recorded in a building.

When using a signal $u_1(t)$ recorded at a location (x_1, z_1) and a reference signal $u_2(t)$ recorded at the location x_2, z_2 (usually the recording from a sensor installed either at the top or the bottom of a building) deconvolution in the frequency domain is defined as

$$S(f) = \frac{u_1(x_1, z_1, f)}{u_2(x_1, z_2, f)}. \tag{3.3}$$

where $u_1(x_1, z_1, f)$ and $u_2(x_2, z_2, f)$ are the Fourier transforms of the recordings at locations $u_1(t)$ and $u_2(t)$, respectively. x and z indicate the horizontal and vertical positions, correspondingly, of the considered sensor. To avoid instabilities coming from division by very small values, Snieder and Şafak (2006) used a regularization technique (based on Clayton and Wiggins, 1976) defined as

$$S(f) = \frac{u_1(x_1, z_1, f) u_2^*(x_2, z_2, f)}{|u_2(x_2, z_2, f)|^2 + \varepsilon} \tag{3.4}$$

where the asterisk indicates the complex conjugate. ε is the regularization parameter referring to the constant added to the denominator, defined as a percentage of the average spectral power. The inverse Fourier transform of $S(f)$ is called the deconvolved wavefield.

In the second step, the earthquake recordings collected simultaneously by the sensors installed in a building and in the field are deconvolved using recording at the top of the building as the reference (i.e. $u_2(x_2, z_2, f)$ in equation 3.4). This step provides the virtual response of the soil-structure system to a unit impulse applied to the top of the building (Figure 3.3). Differently to a similar method proposed by Petrovic and Parolai (2016), in which they used a vertical array of sensors in the building and nearby borehole for the wave propagation analysis, the deconvolution presented in this approach allows for the combined analysis of the earthquake recordings in two dimensions: vertical (in the instrumented building) and horizontal (in the surroundings of the building).

Data analyzed using the deconvolution approach projects the characteristics of the building to the deconvolved wavefield of the surface sensors. The deconvolved wavefield of the sensors in the surroundings of the building could be complex and may contain many phases originating from sources other than the analyzed structure that are hard to analyze separately (input waves, waves reflected at impedance contrasts, etc., Figure 3.3 left). Complementary to the results in the time domain, the troughs in the deconvolved spectra (Figure 3.3 right) provide information on positive or negative interference caused by the propagating, transmitted, and reflected waves.

3.3 Phase identification

3.3.1 Analytical model

If a limited amount of earthquake data is available for the analysis, the stacking of the results to emphasize the repetitive phases of the deconvolved wavefield is not possible. In such a case, the deconvolved wavefield may be relatively hard to interpret by visual analysis. To facilitate the identification of the different seismic phases composing the wavefield and, in particular, that related to the energy transmitted from the building to the ground, an analytical model is developed. The model describes the propagation of the wave within the analyzed system, described in a simplified way.

The analytical model defines the case-specific transfer function between the field sensors, $x(t)$, and the reference sensor at the top of the building, $y(t)$, and is based on a simplified geometry of the analyzed test site (Figure 3.6). The assumption in the developed model is that the input, $x_0(t)$, is the vertically propagating plane wave, which is consistent with the wavefield incidence for earthquake recordings (generally nearly vertical due to the source depth and the velocity structure of the crust).

There are many inversion techniques to find the best fitting model (e.g., regression, genetic algorithms, the grid search method). In this approach, the grid search method is preferred due to its simplicity and short calculation time. Using the grid search method, the search for the parameters defining the best fitting transfer function, performed in the frequency domain, is based on finding the minimal value of the Root Mean Squared Logarithmic Error $RMSLE$ between the real data and the solution, defined as

$$RMSLE = \sqrt{\frac{1}{n}\sum_{i=1}^{n}(log(p_i) - log(a_i))^2/exp(f_i)} \tag{3.5}$$

where n is the number of data points, p_i is the predictions (in this case - the analytical transfer function), and a_i are the real data values (the deconvolved spectra). Since

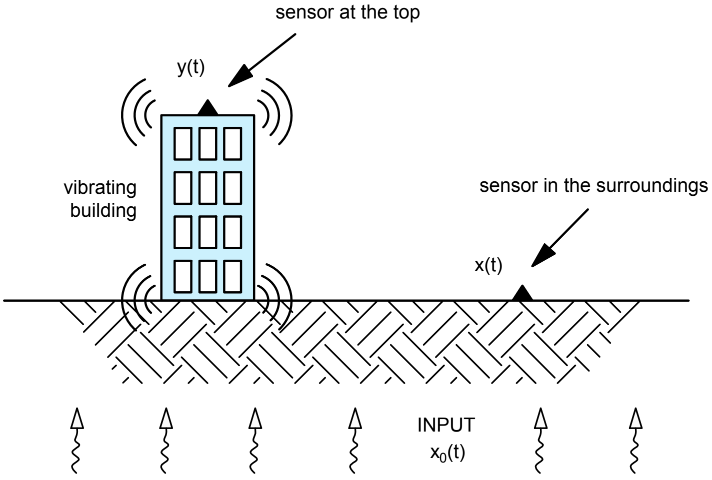

Figure 3.6: The general simplified geometry of the model developed for the seismic phase identification. $x(t)$ is the signal recorded by the sensor installed on the top of the building. $y(t)$ is the signal recorded by a sensor installed in the surroundings of the vibrating building. $x_0(t)$ is the earthquake input approximated as a vertically propagating plane wave. Drawing not to scale.

the frequency spectrum is analyzed on a logarithmic scale, to avoid spurious large errors at high frequencies it is recommended to normalize the $RMSLE$ by the frequency.

The model described by the parameters, which provided the minimum $RMSLE$ in the grid search, is then converted to the time domain using the inverse Fourier transform. Therefore the phase related to the energy transmitted from the building to the ground is identified in the time domain from the real data by comparison to the obtained analytical transfer function. The identified seismic phase is therefore used for further analysis (Figure 3.4a).

The model is used to identify the relevant seismic phases in both horizontal components by selecting the closest peak of the real data deconvolved wavefield to the one indicated by the analytical model. Since the vertical component is mainly dominated by pulses propagating with velocities similar to the P-wave velocity (Parolai et al., 2009), the spatial resolution and/or sampling rate of the recordings are often not sufficient to clearly analyze such high velocities. Therefore the outcome of this part of the analysis is the time window of the deconvolved wavefield analysis estimated by fitting the model to the two horizontal components. This window is later applied also for the vertical component phase selection to analyze all three components together.

3.3.2 Constrained deconvolution

Bindi et al. (2010) proposed a constrained deconvolution approach, for the separation of the seismic input from two sensors installed at the surface and at depth. In the approach proposed in this thesis, the constrained deconvolution step (Figure 3.4b) is used to reconstruct the motion in the surroundings of the building that relate only to the energy transmitted to the ground by the vibrating building.

If one peak of the deconvolved wavefield is analyzed, an assumption for the constrained deconvolution method is that if the propagation medium has small impedance contrasts between the layers (i.e. is almost homogeneous) no information on the soil properties (e.g. the velocity profile) is needed to perform the analysis. The problem considered in constrained deconvolution is presented by the schematic drawing in Figure 3.7a. The idea behind this approach is to find the seismic input motion, $I(t)$ by using an iterative method to constrain the solution a priori. In this way, the down-going waves are filtered out, and the up-going part related to the seismic input is retrieved. Results of the synthetic test using the method by Bindi et al. (2010) are presented in Figure 3.7b. By applying constraints of positivity and the acausal (before time 0) time domain, they selected only the up-going part of the deconvolved wavefield (gray shade in Figure 3.7b). Bindi et al. (2010) based on the analysis of the synthetic data showed that the real input and the reconstructed one using the constrained deconvolution method are almost the same.

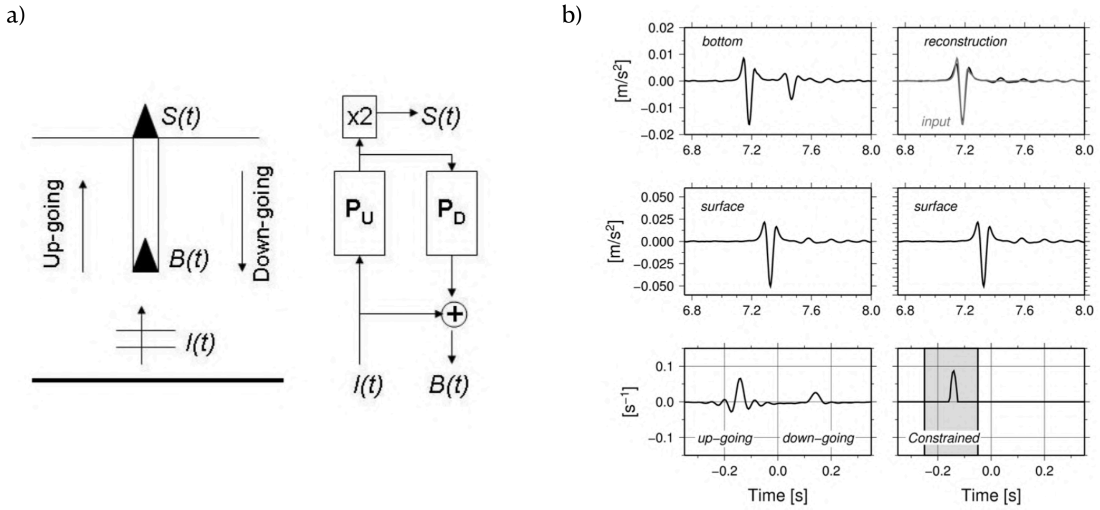

Figure 3.7: a) Schematic drawing of the problem considered in the constrained deconvolution approach. $S(t)$ is the surface recording, $B(t)$ the down-hole recording, and $I(t)$ the searched input recording. On the right, the up- and down-going waves are presented as the transfer functions (P_U and P_D, respectively) of a linear system. b) Results from the synthetic test using a constrained deconvolution approach. On the left, the classical deconvolution results, and on the right, the constrained deconvolution with the positivity and acausal-domain constraints. Figures modified from Bindi et al. (2010).

In the proposed approach, the constrained wavefield is obtained by keeping the positive amplitude values of the deconvolved wavefield within the estimated time interval (defined from the model fit in the previous step) and setting the negative amplitudes values of the deconvolved wavefield to zero outside the interval. The constrained deconvolved wavefields of all three components are then converted to the Fourier domain and convolved with the Fourier spectra of the recordings registered at the top of the building. After going back to the time domain (using the inverse

Fourier transform), the obtained time history represents the motion at the ground surface that is solely related to the desired phase from the deconvolved wavefield. With the assumption that this phase represents the energy transmitted from the building to the ground, the new time history is therefore a reconstructed motion in the surroundings of the building related to its vibration during the analyzed earthquake. In addition, by removing the impact of the vibrating buidling from the motion recorded by sensors installed in the surroundings of the building, it is possible to retrieve the real input ground motion, as if the building did not exist.

3.3.3 Spectral energy calculation

To estimate the spectral energy of the signal, the integral of the power spectral density (PSD) function within the analyzed frequency band is calculated. In the case of the discrete signal, that is simply a sum of the PSD values from the frequency interval used for the previous analyses (deconvolution, analytical model fit, etc.). In this way, the energy of each signal of interest (i.e., the radiated wavefield, the ground motion, and the real input motion) can be compared and it is possible to quantify the impact of the vibrating building on its surroundings.

3.4 Polarization analysis

The last step of the proposed methodology is the polarization analysis of the signal corresponding to the energy transmitted from the building to the ground. It is composed of two independent, yet supplementary, analyses described in the following sections. Knowing that different types of seismic waves have different polarization, this step is needed for the final analysis of the wavefield composition and identification of different wave types and their respective contribution to the radiated wavefield.

3.4.1 Polarization ellipse parameters

The first part of the polarization analysis (Figure 3.5a) is based on the method proposed by Pinnegar (2006) for polarization analysis of three-component signals with the time-frequency S-transform (Stockwell et al., 1996), described in detail in Section 2.2. The method based on the S-transform enables the study of the polarization for each frequency separately, which is particularly useful in cases where the analyzed signal is expected to be a narrow band.

In this step, firstly the discrete S-transforms of all the deconvolved wavefields of all three components, $X(\tau, f)$, $Y(\tau, f)$ and $Z(\tau, f)$, are calculated. Like the Fourier transform of a signal, S-transform has real and imaginary parts ($X_R(\tau, f)$, $X_I(\tau, f)$, $Y_R(\tau, f)$, $Y_I(\tau, f)$ and $Z_R(\tau, f)$, $Z_I(\tau, f)$). Following the mathematical steps described in detail by Pinnegar (2006), it is possible to express the six polarization ellipse elements (the semi-major axis, the semi-minor axis, the inclination, the azimuth, the angle between the ascending node and the position of the maximum displacement and the phase) in terms of $X_R(\tau, f), ..., Z_I(\tau, f)$.

The polarization analysis in the proposed study is based on the evaluation of the three polarization ellipse parameters: semi-major, a, and semi-minor axes, b, and their difference $a - b$, since they define the shape of the ellipse. The semi-major and semi-minor axes are defined as

$$a = \frac{1}{\sqrt{2}}\sqrt{A + \sqrt{B^2 + C^2}} \tag{3.6}$$

and

$$b = \frac{1}{\sqrt{2}}\sqrt{A - \sqrt{B^2 + C^2}} \tag{3.7}$$

where

$$A = X_R^2 + X_I^2 + Y_R^2 + Y_I^2 + Z_R^2 + Z_I^2 \tag{3.8}$$

$$B = X_R^2 - X_I^2 + Y_R^2 - Y_I^2 + Z_R^2 - Z_I^2 \tag{3.9}$$

$$C = -2(X_R X_I + Y_R Y_I + Z_R + Z_I) \tag{3.10}$$

For brevity, arguments (τ, f) has been omitted from Equations 3.8, 3.9 and 3.10. The outcome of those calculation are the time-frequency spectra of the selected polarization characteristics of three-component seismic signals.

The semi-minor axis defines a spectrum of the "circular" part of the elliptical motion, and the difference between semi-major and semi-minor axes defines a spectrum of the "linear" component of the elliptical motion. An estimate of the energy density that considers all three orthogonal components of the signal is defined by the total power S-spectrum expressed by $\sqrt{a^2 + b^2}$.

In order to focus only on the results describing the most energetic part of the wavefield, the total power S-spectrum threshold is used to focus the study on the energy density of interest. This can be achieved by creating a filter for polarization analysis that considers only ellipse parameter values larger than a selected percentage (e.g. 50 %) of the maximum of the total power S-spectrum.

These results provide quantitative information on the distribution and amplitude of the selected polarization ellipse parameters of the deconvolved wavefield.

3.4.2 Particle motion polarization

The second part of the polarization analysis is based on the evaluation of the particle motion of the reconstructed signal related to the energy radiated from the building into the ground. For this purpose, the three-component reconstructed field motion (Figure 3.4b) is decomposed into three planes: radial (X-Z), transverse (Y-Z), and horizontal (X-Y) (Figure 3.8) in which particle motion is analyzed (Figure 3.5b).

The proposed analysis is similar to the surface waves analysis of Yoshida and Sasatani (2008). For selected time windows (e.g. at the beginning of the signal, the most energetic part, or the coda) the particle motion of the reconstructed wavefield transmitted form a vibrating building is decomposed and analyzed in each of the three planes. The estimation of the decomposed particle motion provides information about the polarization of the signal and allows for the evaluation of different wave types (e.g. P, S, and surface waves) that compose the reconstructed wavefield radiated from the building into its surroundings.

The final step of the proposed approach for soil-structure interaction assessment aims at providing an estimation of the wave type of the radiated wavefield. By analyzing the results of a case study, it is possible to compare them with the common assumption in engineering seismology, that during the shaking of a building mainly

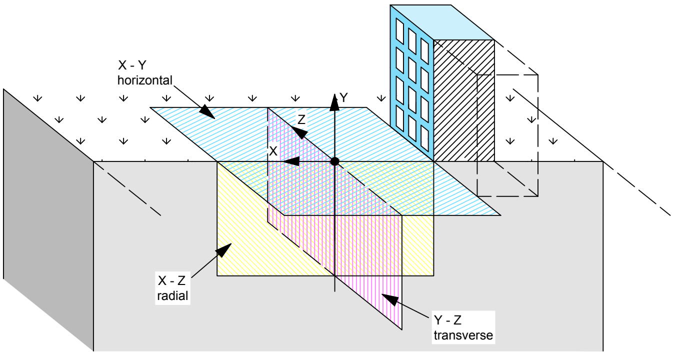

Figure 3.8: Schematic drawing of the polarization planes of the wavefield decomposition. The yellow color indicates the radial plane X-Y, the pink color indicates the transverse plane Y-Z, and the blue color indicates the horizontal plane X-Y.

surface waves are radiated. The information on polarization and amplitudes of the radiated motion could provide important information on the modification of the wavefield in its surroundings by a built structure.

Chapter 4

Test sites

The data used in this thesis comes from two experiments carried out at two different test sites. The list of experiments with the collected data type is presented in Table 4.1. A description of each test site is given in the following paragraphs.

Table 4.1: Test sites and data types collected during the experiments

Test site	Type of data
Matera	noise, earthquake
Piana di Toppo	noise, active source, earthquake

4.1 Matera test site

In October 2019 an SSI experiment was carried out in Matera in the Basilicata region, Southern Italy (Figure 4.1a). During five consecutive days, from 22.10.2019 until 26.10.2019, a dense network of sensors was installed both in a building and on a nearby athletic field (Figure 4.1b). The experiment was designed to study and better understand the interaction between the building and the soil by studying the wave propagation from buildings acting as a secondary source.

4.1.1 Site description

The test site chosen for the experiment consisted of a 7-floor reinforced concrete residential building and a nearby athletic field (Figure 4.1b). The instrumented building was composed of three very similar rectangular units (two external and one in the middle) connected with joints (Figure 4.3 and 4.2a). The length of each unit was 23 m, making in total 69 m in the longitudinal direction (Y). The width of each unit was 12 m in the transverse direction (X). An example of the floor cross-section is presented in Figure 4.3. The average floor height was 3 m.

Matera is an interesting test site because the resonant frequency of the soil is relatively close to the first resonant frequency of most of the built structures in the city as shown by Gallipoli et al. (2020) who made extensive single-station measurements of seismic noise during the CLARA project (CLARA project, 2020) with Horizontal-to-Vertical Noise Spectral Ratio. The resonant frequency in the area of the test site was evaluated as approximately 1.6 Hz (CLARA project, 2020). The average shear wave velocities for each subsoil layer of the test site were estimated

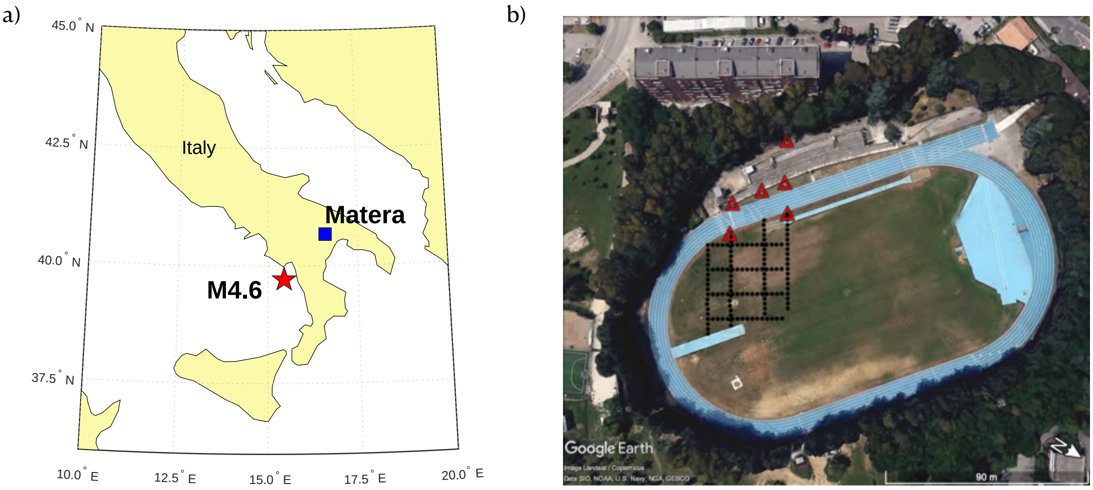

Figure 4.1: (a) Location of Matera test site (blue square) and the epicenter of the M4.6 Catanzaro earthquake on 25.10.2019 (red star). (b) Satellite view of Matera test site. Athletic field instrumentation deployment is indicated with red triangles (three-component sensors) and black dots (vertical geophones).

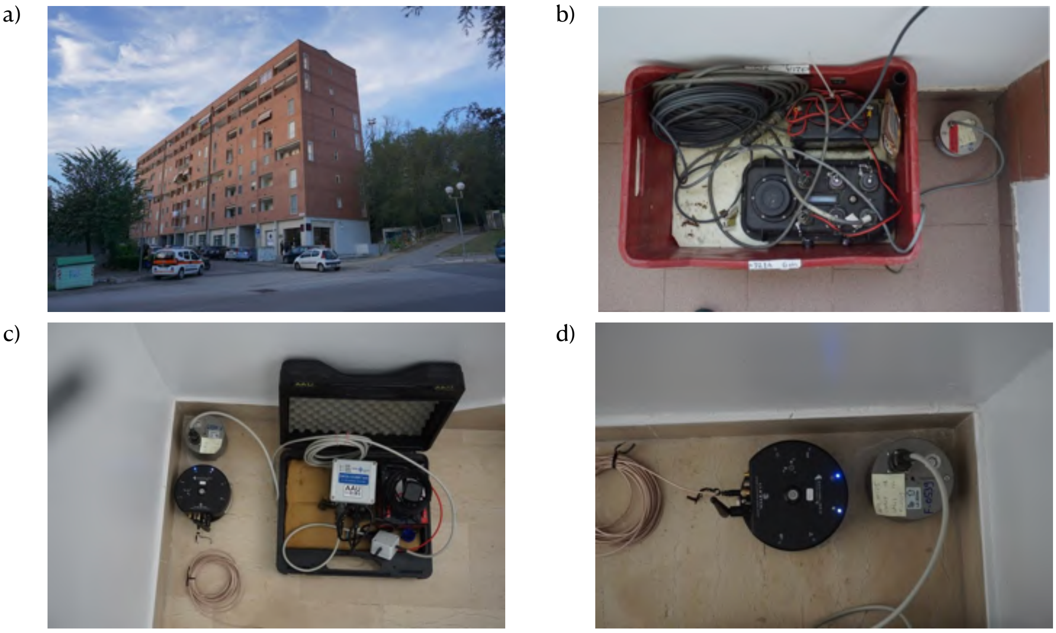

Figure 4.2: a) The building instrumented during the Matera experiment. b) Reftek digitizer connected to LE-3Dlite 1 s sensor. c) CUBE digitizer connected to LE-3Dlite 1 s sensor. d) Lunitek Sentinel Geo. Photographs author: Bojana Petrovic.

by Gallipoli and Lupo (2012) by down-hole tests. The depth of each layer (Lorenzo Petronio, personal communication) is presented in Table 4.2. The geology of the test site and its area with the location of the instrumented building and the athletic field composed of sands overlaying Subappenine clays, Garvina calcarenite, and Altamura limestone is shown in Figure 4.4.

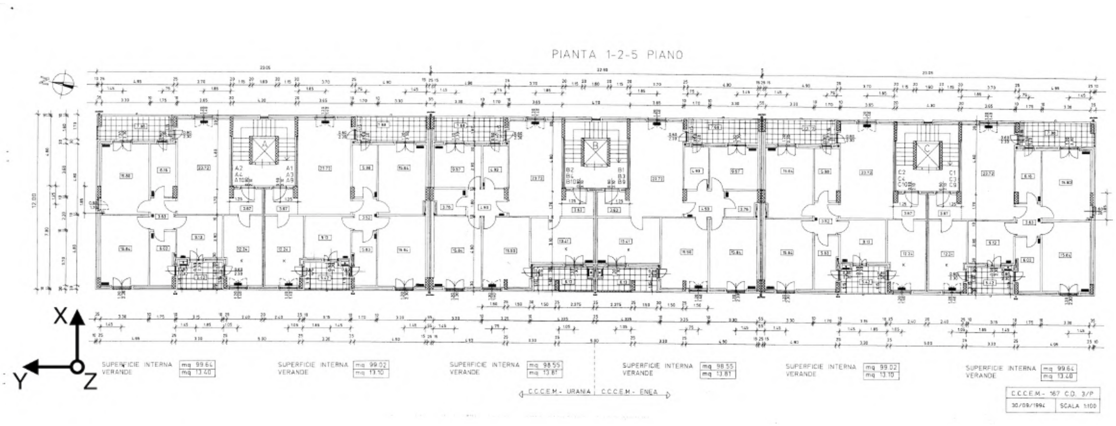

Figure 4.3: An example floor plan of the building instrumented during the Matera experiment.

Table 4.2: The average shear wave velocities obtained by down-hole tests (Gallipoli and Lupo, 2012) of the soil layers in Matera (from the top downwards). The last column presents the depth of each layer in the area of the experiment test site.

Type of soil	S-wave velocity [m/s]	Layer depth [m]
Sand	261 ± 113	0 - 10
Subappenine clay	367 ± 156	10 - 70
Garvina calcarenite	914 ± 324	70 - 130
Altamura limestone	1052 ± 130	from 130

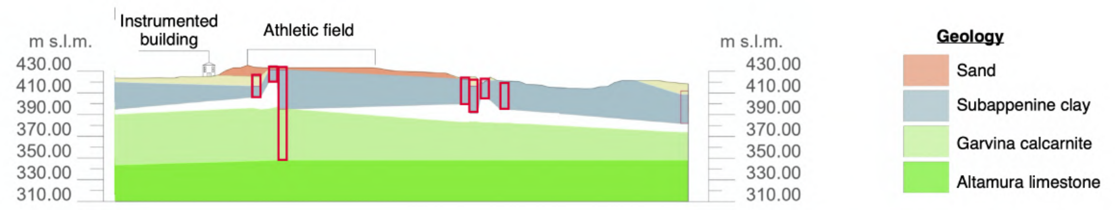

Figure 4.4: Geological cross-section of the test site and its area with location of the instrumented building and the athletic field indicated. Red rectangles show positions where the geological measurements were performed. Colors indicate different geological units described on the right. Data owner: OGS

4.1.2 Experimental setup and data description

Instrumentation

A dense array of seismometers was installed both in the building and on the athletic field. Two experimental setups were used: the first one was designed for the SSI analysis (Figure 4.5a), and the second aimed at a better understanding of the structure's dynamic behavior (Figure 4.5b). The total experimental instrumentation consisted of three three-component digitizer-sensor combinations (hereon referred to simply as ”sensors”) listed in Table 4.3 and an array of 139 vertical geophones (black dots in Figure 4.1b). The approach presented in this thesis is based on the analysis of three-component data, therefore the recordings registered by vertical geophones array were not considered in this study.

The location of the sensors in the building was designed to analyze the wave propagation in the structure, therefore the vertical arrays in each unit had at least sensors on the highest possible floor and in the basement. The locations of the sensors on the athletic field were designed to be horizontally aligned with the vertical arrays in the building. The highest sensors in the building were installed in the stairwells or in the apartments on the 7th floor because it was not possible to install sensors on the pitched roof of the building.

Table 4.3: List of three-component digitizer-sensor combinations and the total number of sensors used during both experimental setups.

Digitizer	Sensor	Sampling freq. [Hz]	Nb of instruments
CUBE	LE-3Dlite 1s	200	3
Reftek	LE-3Dlite 1s	250	8
Lunitek	Sentinel Geo	250	14

At the top and bottom of the building, different sensors were installed to compare the recordings and the possible influence of the types of sensors on the results. Therefore, wherever there were two types of sensors next to each other, in this study, only data from Reftek or CUBE sensors was used. To make the data uniform for the analysis, signals recorded at a sampling rate of 250 Hz (Reftek and Lunitek sensors) were resampled to 200 Hz (the sampling rate of CUBE sensors).

Sensor arrays

As mentioned in Section 3, ideally, a minimum of three sensors are required for the analysis: one on the top of the building, one at the bottom, and one in its surroundings. Taking advantage of the array of sensors installed during the experiment in Matera, the data used in this study come from additional sensors (both in the building and on the athletic field).

Array 1 (Figure 4.5c,d, yellow triangles) was composed of three sensors installed in the stairwell of unit 46 (one on the 7th floor - 101, one between the 3rd and 4th floors - 102, and one in the building's basement - 103) and two sensors installed on the athletic field at distances of 20 m and 50 m from the building, perpendicular to the building's vertical array and the longer side of the building (104 and 105, respectively).

Array 2 (Figure 4.5c,d, pink triangles) consisted of four building sensors installed in the stairwell of unit 44 (one on the 7th floor - 201, one between the 4th and 5th - 202, one between the 2nd and 3rd floors - 203, and one in the basement - 204) and one field sensor around 60 m from the building (205). The athletic field level was elevated around 7.5 m above the level of the lowest sensors installed in the building.

Array 1A and Array 2A (green and blue triangles in Figure 4.5c) were composed of the sensors installed in the apartments on the left side of units 44 and 46. The recordings from the sensors installed at the highest floors in those arrays (7th floor) were used for the spectral ratio calculation.

Data

During the experiment, seismic noise recordings were carried out for five consecutive days (22.10.2019-26.10.2019). During this measurement period, an M4.6 Catanzaro

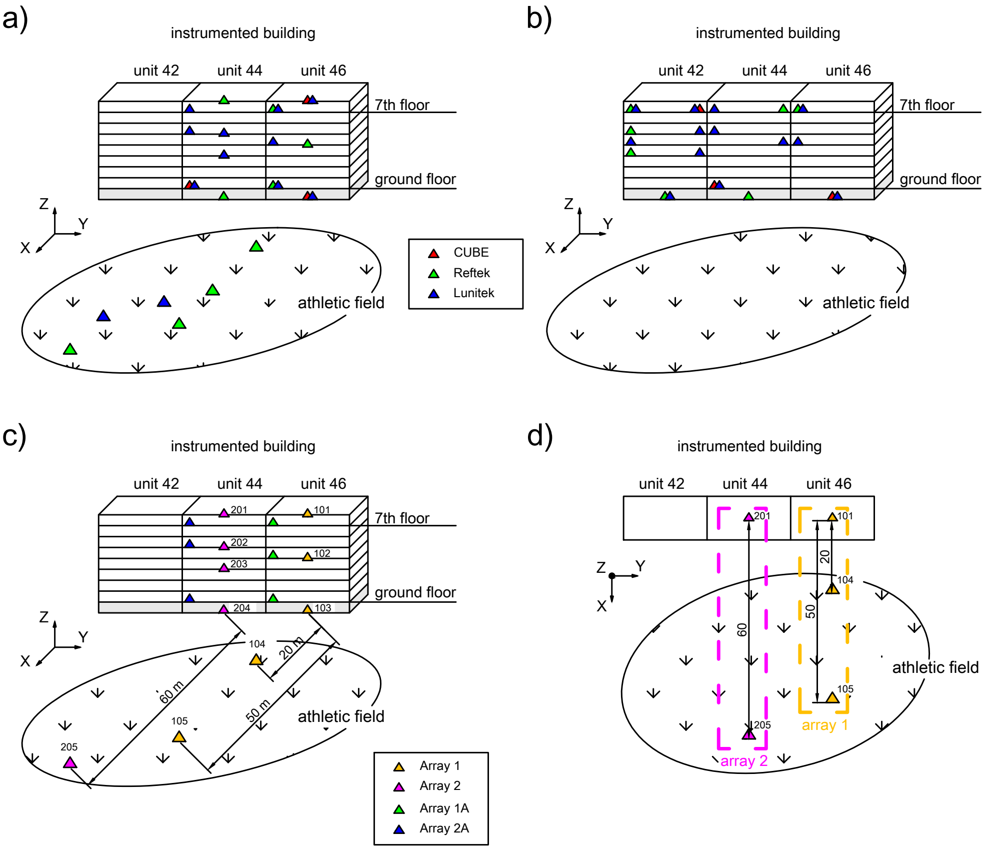

Figure 4.5: Schematic drawing of the positions of the three-component sensors in the building and on the athletic field. a) instrumental setup for the soil-structure interaction study, b) instrumental setup for the estimation of the dynamic behavior of the building. c) Location of the sensors from Array 1, Array 2, Array 1A, and Array 2A. d) Top view of the location of the sensors from Array 1 and Array 2. For a) and b) triangle colors correspond to different digitizer/sensor combinations: red - CUBE with LE-3Dlite 1s, green - Reftek with LE-3Dlite 1s, blue - Lunitek Sentinel Geo. In c) and d) yellow triangles represent sensors from Array 1, pink - sensors from Array 2, green - from Array 1A, and blue - from Array 2A. Names of the sensors from Array 1 and Array 2 are next to the corresponding triangles.

earthquake (EQ) occurred approximately 145 km South-West of the Matera test site (Figure 4.1 red star) at 4:31 am (UTC) on 25.10.2019. The occurrence of the earthquake during the acquisition provided useful data for testing the proposed approach since the methodology is based on the analysis of earthquake recordings. No structural damage to the analyzed building was reported due to the occurrence of the registered earthquake, given the magnitude and distance of the earthquake. Due to the limited duration of the battery of some of the Lunitek sensors, the earthquake was not recorded by all stations since it occurred early in the morning, before the battery recharging.

The earthquake recordings from Array 1 are shown with the corresponding Fourier amplitude spectra in Figure 4.6a and b. The length of the recordings is

120 s. 24 hours long seismic noise recordings were used for the FDD analysis and the spectral ratio (the analysis of the dynamic behavior of the structure). An example of two hours of seismic noise recordings of Array 1 and their Fourier amplitude spectra are presented in Figure 4.6c and d. The Fourier amplitude spectra of the noise recordings were calculated by averaging spectra of 20 s-long time windows (360 windows). In all the plots in Figure 4.6 the gray background indicates the recordings of sensors installed in the building and the green background the ones installed on the athletic field.

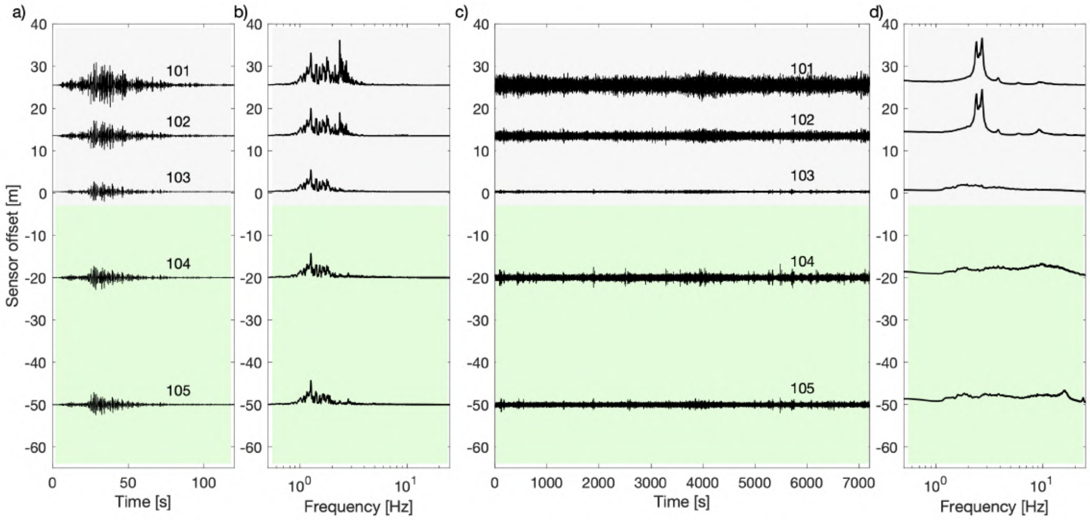

Figure 4.6: Example of the velocity recordings of the X component and their Fourier amplitude spectra used in this study. a) example of the Catanzaro earthquake recordings registered during the Matera experiment of sensors in Array 1; b) corresponding earthquake Fourier spectra; c) example of seismic noise recordings for the same array; d) corresponding moving window Fourier spectra. The gray background indicates sensors installed in the building. The green background indicates sensors installed on the athletic field. Sensor names are above the corresponding time histories. The frequency plots are in a semi-log scale with a logarithmic x-axis. The y-axis indicates the vertical (building) or horizontal (athletic field) offset of the sensors with respect to the basement sensor. Sensors offset below 0 indicates the horizontal distance of sensors installed in the field relative to the bottom sensor in the building.

In the presented example of the earthquake and seismic noise signals, the amplitude of the signals in the building is increasing with height, both in the time and frequency domains. The amplitude of the signals in the field is similar for data coming from both field sensors (green lines). The Fourier amplitude spectra of the earthquake recordings (Figure 4.6d) has multiple peaks corresponding to both the soil and building. The seismic noise spectra (Figure 4.6d) are smoother since they are the average of multiple moving windows Fourier spectra.

4.2 Piana di Toppo test site

The second experiment, carried out in April 2022, was designed to create the second data set for testing the proposed approach in a controlled, well-known environment using a simple structure. The aim was to reconstruct the Matera experiment and compare the results from both test sites. For this reason, a simple structure was built on the existing test site Piana di Toppo of the National Institute of Oceanography and Applied Geophysics (OGS), and extensive seismic measurements were performed. The Piana di Toppo test site, along with the built structure and performed measurements, is described in the following paragraphs.

4.2.1 Site description

Piana di Toppo test site is located in northeastern Italy in the Friuli Venezia Giulia region, around 70 km from Udine in the inter-mountain plain on the external thrust-belt of the eastern Southern Alps (Figure 4.7a). The site is a rectangular area with 80 m length and 50 m width (Figure 4.7b) located in a seismically active area with low urban seismic noise (Piana di Toppo, 2022). Next to the southern edge of the test site, there are train rails on which the tourist train goes between the cities of Salice and Gemona in the summertime. During the experiment, the train was not operating. Around 100 m north of the test site there is a provincial road (SP32). The test site is far away from any other infrastructure.

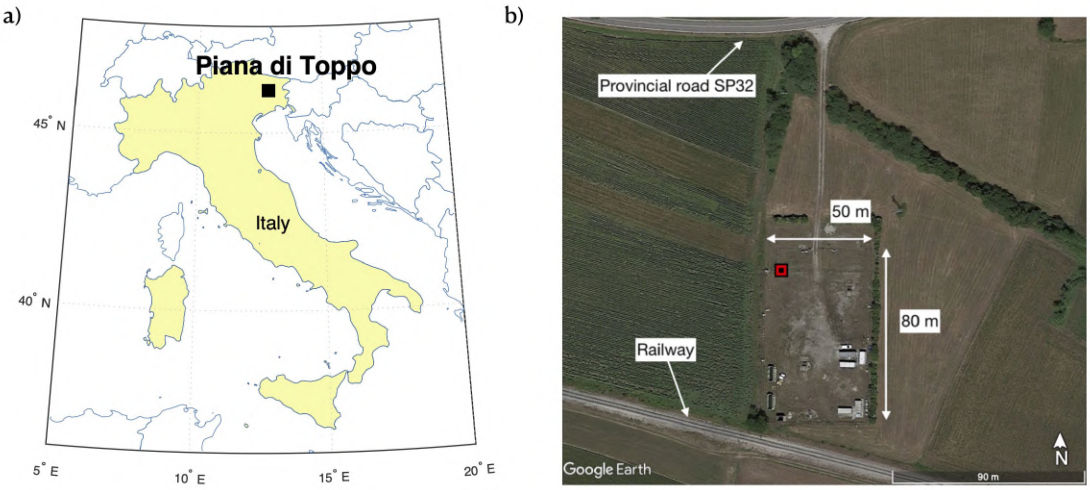

Figure 4.7: (a) Map of Italy with the location of the Piana di Toppo test site indicated (black square). (b) Satellite view of the Piana di Toppo test site. The location of the center of the built structure is marked with a red square.

The geology of the test site consists of Quaternary alluvial sediments (loose coarse gravels) overlying Miocene conglomerates (the Morello formation) (Poletto et al., 2011; Dreossi and Parolai, 2022). The S-wave velocity profile for the Piana di Toppo test site was calculated using the Simultaneous Algebraic Reconstruction Technique (SART) by Dreossi and Parolai (2022) and is presented in Table 4.4.

4.2.2 Design of the structure

The structure designed for the experiment was a square concrete shallow foundation with a quadratic hollow steel column (QHS profiles 250 mm x 250 mm x 10 mm)

Table 4.4: The average shear wave velocities of the soil layers at the Piana di Toppo test site (Dreossi and Parolai, 2022).

Layer nb	Thickness [m]	S-wave velocity [m/s]
1	11.1	551.4
2	33.2	741.6
3	-	1011.8

over-topped by a concrete slab (Figure 4.8a). It was constructed in the North-West part of the test site (Figure 4.7b). The total height of the structure was 2.5 m and the width was 2 m x 2 m. The aim of the design was to enable the approximation of a structure to a single degree of freedom system with a fixed-base fundamental frequency of 5.0 Hz, estimated using SAP2000 software (courtesy of Chiara Amendola). The column has been modeled as an elastic beam element with QHS steel section ($\gamma_S = 78$ kN/m3) characterized by Young's modulus equal to $2.10 * 10^8$ kN/m2. The foundation and top slabs were modeled as shell elements made of concrete material ($\gamma_C = 25$ kN/m3). In the model, the column was fully fixed to the slabs using linear link elements constraints. The constructed structure with part of the installed instruments is presented in Figure 4.8c.

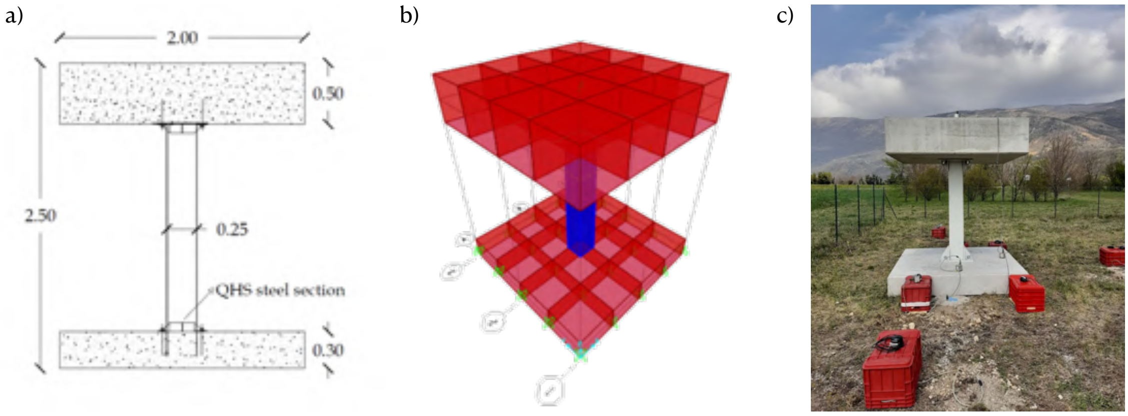

Figure 4.8: a) Schematic drawing of the designed structure (dimensions in m). b) 3D numerical model of the structure from SAP2000 (courtesy of Chiara Amendola). c) Constructed structure located in the North-West part of the Piana di Toppo test site.

4.2.3 Instrumentation and experimental setups

Instrumentation

During the experiment, 15 three-component Lennartz sensors connected to 12 Reftek digitizers (nine with three channels and three with six channels) (Figure 4.9a) were used for recording seismic data. The sampling frequency of the digitizers was set to 250 Hz. There were 12 LE-3D/1s (Figure 4.9b) and, additionally, three LE-3D/5s connected to the three digitizers with six channels (hereon the digitizer-sensor combinations will be referred to as "sensors"). GPS antennas were used for the synchronization of the instruments. The energy was supplied by external batteries connected to the digitizers. An example of the instruments installed at the test site is presented in Figure 4.9c.

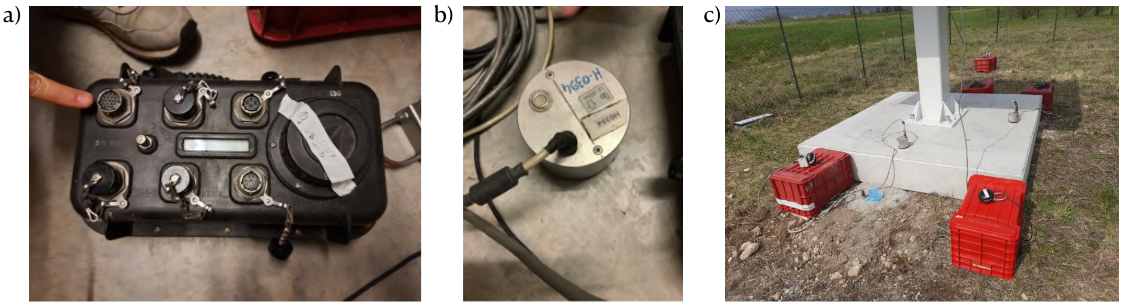

Figure 4.9: a) Reftek digitizer used for the study, b) 1s Lennartz sensor LE-3D/1s, c) installed instrumentation at the test site.

From now on the 1s Lennartz sensors (LE-3D/1s) are identified by the subscript "E" (corresponding to the digitizer channel used to connect those sensors), and 5s Lennartz sensors (LE-3D/5s) are identified by the subscript "H" next to the sensor/digitized ID.

Experimental setups

During the Piana di Toppo experiment there were three instrumental setups:

- Setup 1 (S1) - before installation of the structure (Figure 4.10),
- Setup 2 (S2) - after installation of the structure, with a dense sensor array on the top and bottom slabs (Figure 4.11),
- Setup 3 (S3) - sensors installed both on the top and bottom slabs of the structure, and on the field (Figure 4.12).

In the first setup - S1, all available sensors were installed in the ground in two perpendicular linear arrays aligned with the North-South (NS) and East-West (EW) axes of the future structure (Figure 4.10). Sensors were located at increasing distances from the structure loosely following the Fibonacci sequence. Such an array shape was chosen since it provides the best data analysis quality in L-shape arrays for an additional passive-seismic study (Seismic, 2022). For the installation of each of the sensors, a shallow hole was dug and the bottom was leveled with sand. Then, the sensors were installed and covered with soil. The placement of the sensors right below the surface of the ground was done to ensure good coupling with the ground and to decrease the negative impact of adverse weather conditions on the recordings. In this setup, 5s sensors were installed right next to the 1s sensors connected to the same digitizer to have a direct comparison of the recordings coming from two different sensor types. This setup was installed for approximately 20 hours.

For the installation on the structure, all the sensors were removed from their positions to avoid potential damage from the heavy construction machinery which was used for the installation. After the installation was finished, for the S2 setup (Figure 4.11), most of the sensors were installed on the top and bottom slab of the a)

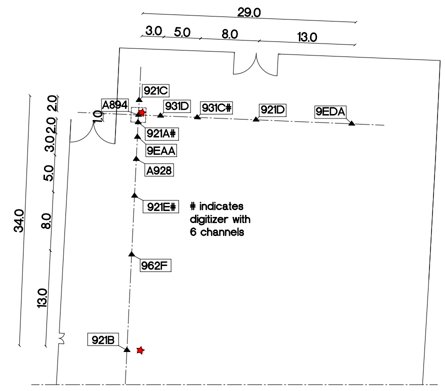

Figure 4.10: Setup S1 used during the Piana di Toppo experiment. Triangles represent sensors, red stars indicate active source locations, and the blue square is the location of the structure. # next to the sensor name indicates 5s Lennartz sensors.

b)

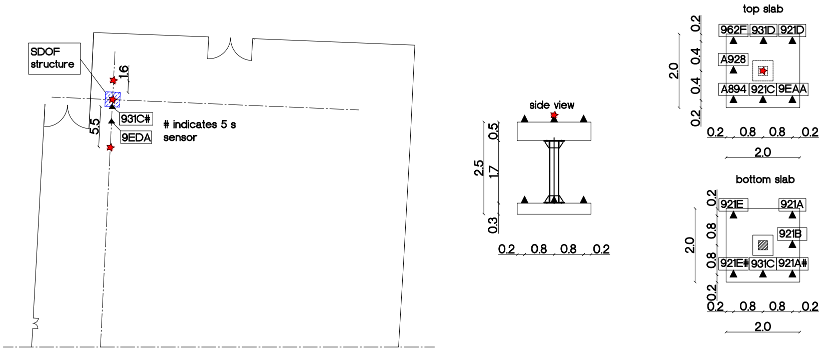

Figure 4.11: Setup S2 used during the Piana di Toppo experiment. Triangles represent sensors, red stars indicate active source locations, and the blue square is the location of the structure. # next to the sensor name indicates 5s Lennartz sensors.

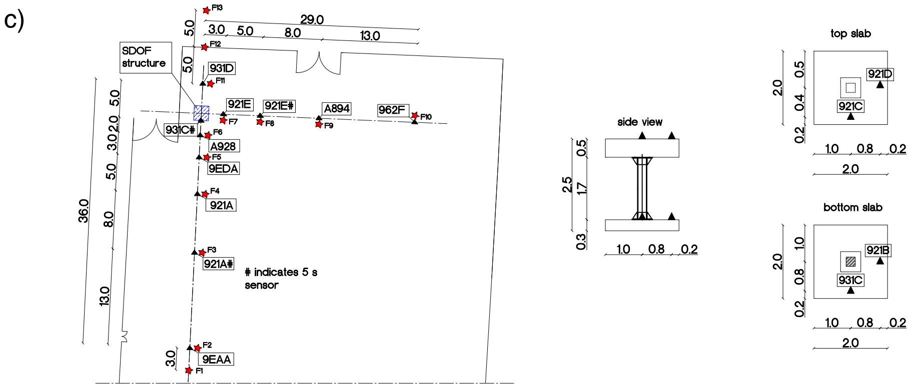

Figure 4.12: Setup S3 used during the Piana di Toppo experiment. Triangles represent sensors, red stars indicate active source locations, and the blue square is the location of the structure. # next to the sensor name indicates 5s Lennartz sensors. Numbers from F1 to F13 next to the red stars refer to the active source position. Dimensions are in meters [m].

built structure. In total, on the top slab of the structure, there were seven sensors installed in four corners and three sides, to enable the use of the active source in the middle of the top slab of the structure. Such placement of the active source was chosen due to the relatively small available area on the top slab for such a type of excitation (2 m x 2 m).On the bottom slab, there were six sensors in total: one in each corner of the foundation and two on the sides facing the ground arrays of S1 and S3 setups. Two remaining sensors were installed on the soil North of the structure: one right next to the bottom slab (the 5s 931C#), and the second 2 m away (9EDA). This setup was installed for approximately 19 hours.

In the last setup, S3 (Figure 4.12), all the sensors, but four, were installed in the ground. The four sensors on the structure were installed as follows: two on the top slab and two on the bottom slab. At the top slab, sensor 912C was left in its original position from S2, and sensor 921D was moved from the corner of the slab to the East edge to be aligned in the East-West ground array. The two sensors installed in the foundation slab were located on the South and East side of the slab. The sensors installed on the structure were positioned to be aligned with the ground arrays. The other sensors were placed in the L-shape array in similar positions as in the S1 setup. This setup was installed until the end of the experiment, for around 20 days.

The setup layouts were chosen to enable a comparison of the recordings collected before and after the installation of the structure in order to assess possible changes in the medium. Therefore in the S3 setup, the location of the ground instruments was the same before and after the installation of the structure. Due to the malfunction of the GPS antenna, the recordings of the A928 sensor could not be considered in the analysis.

4.2.4 Data description

Seismic noise

During the Piana di Toppo experiment for 23 consecutive days, seismic noise was recorded using the three described setups.

An example of the noise recordings of a six-hour-long time window from the S3 setup and the corresponding average Fourier amplitude spectra (20 s long moving window) is presented in Figure 4.13.

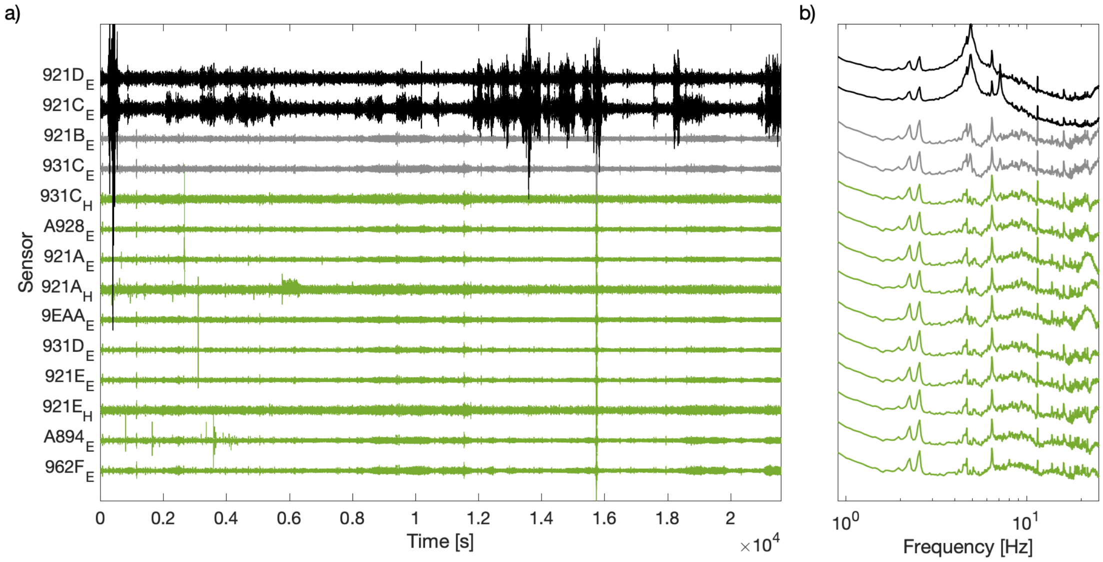

Figure 4.13: a) Example of the time history of the East component of the noise recordings from all the sensors from S3. Black traces indicate sensors installed on the top slab of the structure. Gray traces are sensors on the bottom slab. Green traces are sensors installed on the soil. b) Corresponding Fourier amplitude spectra averaged from 20s moving window. Data are from 18:00 to 23:59 on the 9th of April 2022.

Figure 4.13 shows that the signal recorded at the top of the structure is larger than that collected at the lower slab and on the ground. The increase in the amplitude of shaking at the top is visible in both time and frequency domains.

Active source

In addition to the noise recordings, active source measurements were performed using an Elvis VII-type seismic vibrator source. The vibrator generated a P-wave upsweep of 30 s with a theoretical frequency range from 10 Hz to 200 Hz. Three to four sweeps for each source position were made.

In the S1 setup, the vibrator was placed in two positions: 1) next to the 921B sensor in the NS array and 2) next to the sensor A894 installed in the center of the planned location of the structure (Figure 4.10). In the S2 setup, three active source positions were considered: one directly on the top of the structure in the middle of the slab, and two on the ground – one 5.5 m and another 1.6 m from the Southern and from the Northern edge of the foundation, respectively (Figure 4.11). For the S3 setup, 13 vibrator positions, all on the ground, were used (Figure 4.12).

An example of the recordings of one sweep source (F13) by the S3 setup and of the corresponding Fourier amplitude spectra smoothed with Konno-Ohmachi smoothing function (Konno and Ohmachi, 1998) for the North-South line of sensors from the S3 setup is shown in Figure 4.14.

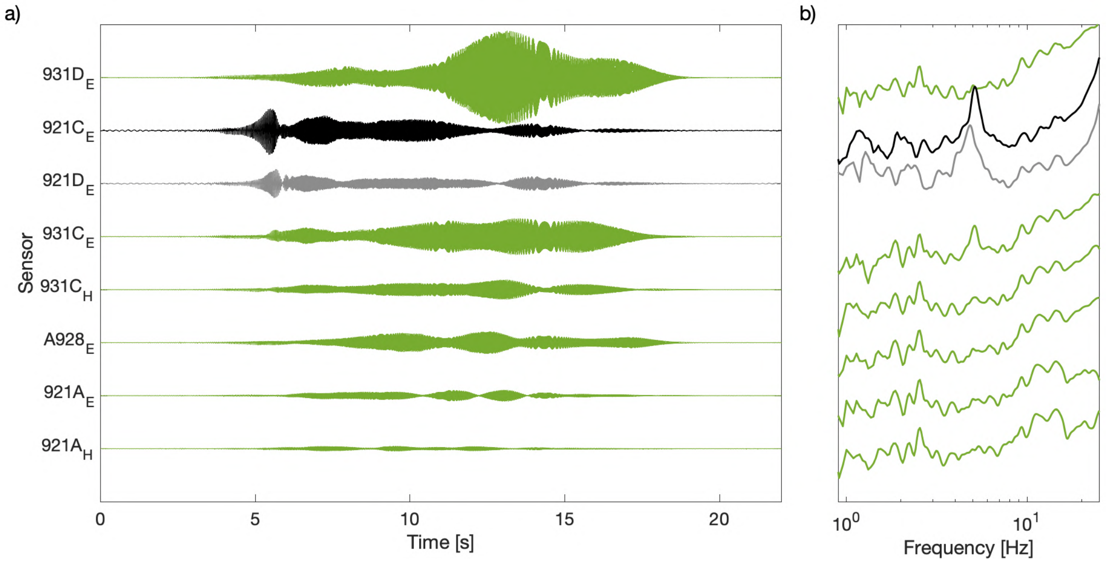

Figure 4.14: a) Example of the vertical component recordings of the active source in the NS array (S3 setup). The source was located 15 m North of the structure (F13 in Figure ??c). The black lines show the recordings of sensors installed on the top slab of the structure, gray lines represent the recordings of sensors located at the bottom slab. Green lines represent sensors installed on the soil. b) Corresponding Fourier amplitude spectra smoothed with Konno-Ohmachi smoothing function (Konno and Ohmachi, 1998).

Earthquakes

The S3 configuration was used for recording seismic signals for almost three weeks. Therefore it was possible to acquire also weak motions, including earthquake recordings. In total, 23 earthquakes generated signals were registered by the installed array. A list containing dates, location, depth, and magnitude of the events was created based on the regional (RTS `https://rts.crs.inogs.it/en/home.html`) and national (INGV `http://terremoti.ingv.it/en`) Italian earthquake catalog and is presented in the Appendix (Table A.1 and A.2).

However, even though the signal of the registered earthquakes was clear at the ground level, for most of the earthquakes, the recordings at the top of the structure had a poor signal-to-noise ratio (SNR). SNR was calculated by comparing the spectra of the event signal with the pre-event noise, and only recordings with a ratio above 3 in the frequency range between 1 and 20 Hz were chosen for the analysis.

In the end, only six earthquakes with sufficient SNR were selected for this study: one M1.0 local earthquake around 18 km North-West from the test site (earthquake B.2, Table A.2), and five earthquakes from the April 2022 Bosnia and Herzegovina sequence with magnitudes from M3.9 to M5.5 located around 550 km from the test site (earthquakes A.8, A.9, A.10, A.11, A.12, Table A.1). The high level of noise and poor SNR in the recordings from the sensors on the top of the structure was most likely caused by a combination of poor sensor-structure coupling, unfavorable weather conditions, and the low energy of the shaking. Figure 4.15 shows the epicenter location of the selected earthquakes.

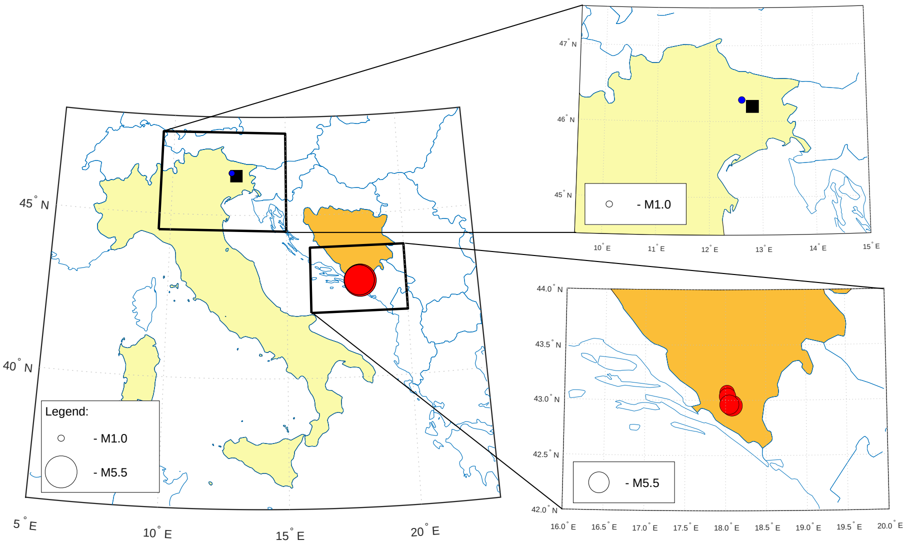

Figure 4.15: Location of the epicenters of the selected earthquakes registered by the array installed in the Piana di Toppo experiment. The blue circle shows the epicentral location of the M1.0 earthquake from the RTS earthquake catalog. Red circles show the epicentral locations of the Bosnia and Herzegovina sequence. The size of the earthquakes on the map on the left is scaled with the magnitude. Maps on the right are zoomed maps of the framed areas. The black square indicates the location of the Piana di Toppo test site. Italy is indicated with yellow color, and Bosnia and Herzegovina with orange.

Figure 4.16 shows the recordings and the corresponding spectra of the M5.5 earthquake that occurred on the 22nd of April at 21:07:49.1 (UTC) near Stolac in Bosnia and Herzegovina (approximately 550 km from the test site) collected by the North-South line of the array. Similar to the noise recordings, the amplitudes of the signals recorded by the sensor installed on the top slab of the structure are greater with respect to the recordings from the bottom slab and the soil.

Although this section contains the description of all the collected data during the Piana di Toppo experiment in this study I focus on the analysis of the earthquake and noise data.

4.3 Preparation of the data for the analysis

Prior to the analysis using the approach proposed in this thesis, the mean and the trend should be removed from the earthquake time-history data. Additionally, if the data is recorded by different types of instruments, as it is in the case of both the Matera and Piana di Toppo experiments, it is necessary to remove the instrumental

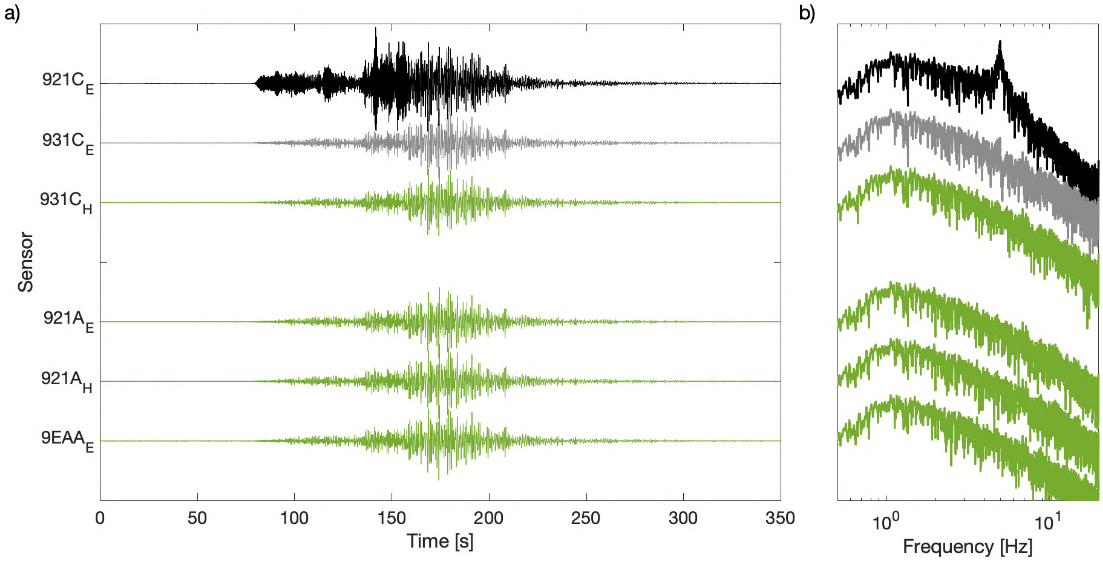

Figure 4.16: a) Example of the velocity amplitude values of the East component of the earthquake recordings registered by NS line from the S3 setup. The black trace indicates the sensor installed on the top slab of the structure, the gray trace, a sensor at the bottom slab, and the green trace sensors installed on the soil. b) Corresponding Fourier amplitude spectra.

response to jointly analyze the data. For this reason, the instrumental response is deconvolved from the time histories. In the analysis presented in this thesis, the data was tapered with a 5 % Hann window.

Chapter 5

Results Matera

5.1 Dynamic behavior of the building

5.1.1 Results

Spectral ratio analysis

To estimate the dynamic behavior of the building, both seismic noise and earthquake recordings were analyzed. For spectral ratio calculation data from Arrays 1, 1A, 2, and 2A (that recorded both the seismic noise and the earthquake) from the two building units instrumented during the first setup (Figure 4.5c,d) were used. Unit 42 was not considered for spectral ratio analysis, since there were no earthquake recordings available. The spectral ratios of the seismic noise are the average spectral ratios of one day of recordings using 20 s moving windows. Both noise and earthquake spectral ratios were smoothed with a Konno-Ohmachi smoothing function with a bandwidth coefficient equal to 80 and are presented in Figure 5.1.

The fundamental frequency of the building estimated from the noise recordings is 2.4 Hz in the X (transverse) direction, and 2.5 Hz in the Y (longitudinal) direction. The second peak in both components is very close at 2.7 Hz, however, in the spectral ratios of the X direction it disappears towards the center of the building (Arrays 2 and 2A). The third peak at 3.8 Hz is present in all arrays in the X direction. In the Y direction, the 3.8 Hz peak, similar to the 2.7 Hz peak in the X direction, disappears towards the middle of the building (Arrays 2 and 2A). The fourth peak at 6.4 Hz in the X direction is mostly visible in the spectral ratios from arrays installed near the edge of each unit (Arrays 1A and 2A), and it is much less amplified in the middle arrays (Arrays 1 and 2). In the Y component, the amplification of the peak at 6.4 Hz is present in all the noise spectral ratios from both horizontal components. There is no clear amplification of the vertical component in none of the arrays.

The shape of the spectral ratios calculated from the earthquake data is different compared to those calculated from the noise data. In Arrays 1 and 1A, the earthquake spectral ratios do not show a peak at 2.4 Hz in the X direction. The peak at this frequency is, however, present in the middle unit (Arrays 2 and 2A). The main peak in the X component of at 2.6 Hz in Array 1 and at 2.7 Hz in Array 2. Spectral ratios of all of the Y components in all of the arrays show clear peaks at 2.5 Hz and 2.7 Hz, similar to the noise spectral ratio results. Around 3.8 Hz, the earthquake spectral ratios are significantly amplified in the X component of arrays 2 and 2A and in the Y component of arrays 1 and 1A. For higher frequencies, the spectral ratios

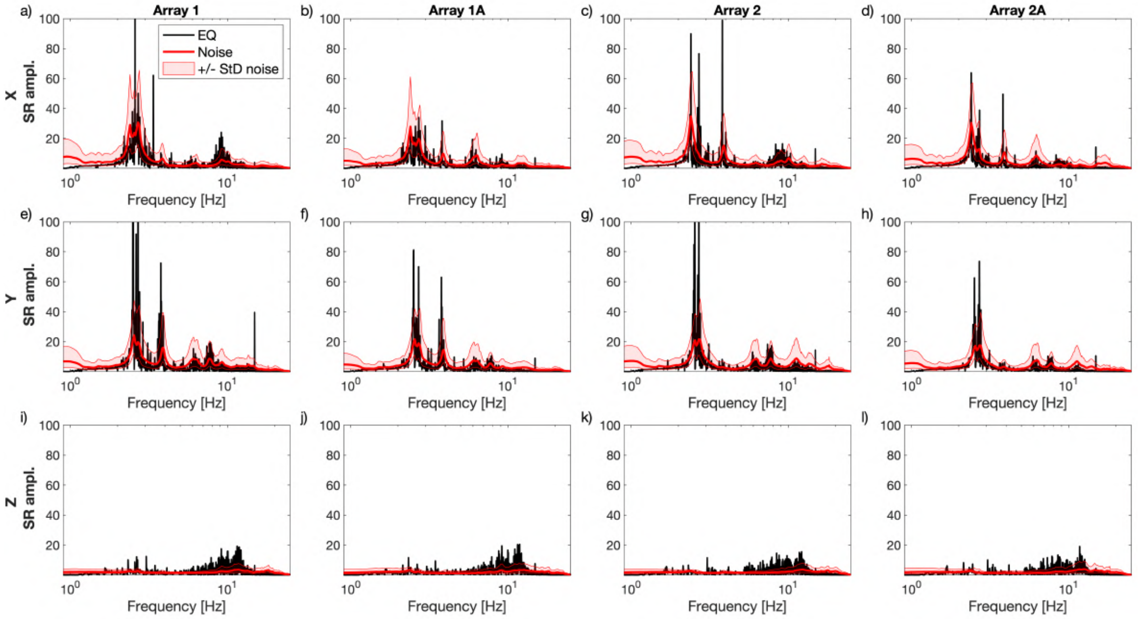

Figure 5.1: Comparison of noise and earthquake spectral ratios for each component for Arrays 1, 1A, 2, and 2A. Red lines indicate the noise spectral ratio. The red shade indicates the +/- standard deviation of the average noise spectral ratio. Black lines show the spectral ratio of the earthquake recordings.

have similar shapes to those calculated from the noise recordings with all the main peaks in the frequency range from 2 Hz to 10 Hz. The calculated spectral ratios for the vertical component do not show any significant peaks for either the noise or the earthquake recordings.

Another visible aspect is that the amplification of the earthquake spectral ratios in the middle arrays of each unit (Array 1 and Array 2) is much higher than that of the noise. By comparing earthquake data and the upper standard deviation of the noise data, the biggest amplification difference is observed for the Y component in Array 2, where the amplification of the earthquake spectral ratio at 2.7 Hz (out of the scale of Figure 5.1g) is over seven times higher than the noise spectral ratio at the same frequency peak. Smaller, but still significant amplification differences between the earthquake and noise spectral ratios are observed for the peaks at 2.5 Hz and 2.7 Hz in the Y component (earthquake almost four times bigger than noise for both), and at 2.6 Hz in the X component in Array 1 (earthquake 2.5 times bigger than noise peaks at 2.4 and 2.7 Hz). The amplification difference is not as significant for the X component in Array 2A, where both noise and earthquake data have similar levels of amplification of the main peaks of spectral ratios. In the Y components both Array 1A and Array 2A, peaks at 2.5 Hz and 2.7 Hz are around two times bigger for the earthquake compared to the noise spectral ratios. Different behavior is observed in the X component from Array 1A, where the noise spectral ratio is amplified equally or more than the earthquake data spectral ratio. In general, the amplification of the spectral ratio peaks is higher for the middle arrays (Array 1 and Array 2) than those installed near the edges of each unit (Array 1A and Array 2A).

Frequency Domain Decomposition

In addition to the spectral ratio analysis, it was possible to perform FDD analysis using noise recordings from all sensors installed in the building during the first and the second setup. This was especially beneficial for separating close peaks observed in both the noise and earthquake spectral ratios. The data from both instrumental setups were used for the FDD analysis. The FDD results in form of the singular values of the calculated PSD matrix are presented in Figure 5.2.

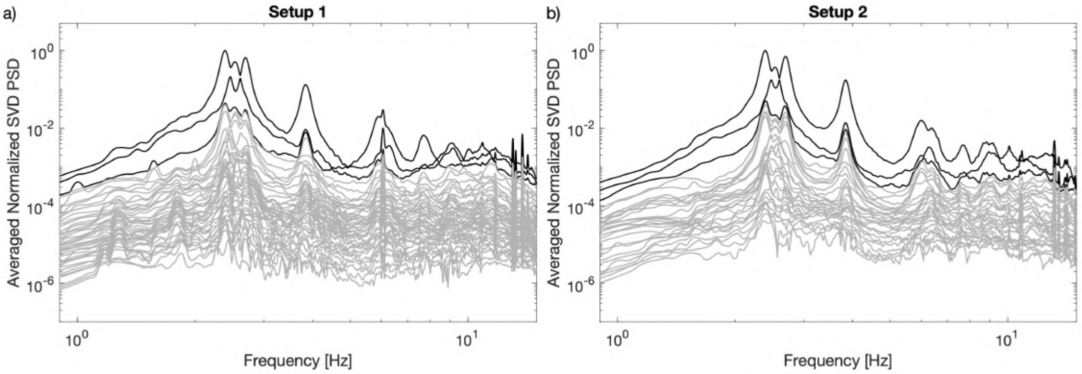

Figure 5.2: Singular values of the PSD matrix from the FDD analysis for data from a) the first instrumental setup and b) the second setup. For better visualization of the FDD peaks, the first three eigenvectors from each setup are plotted with black color and the rest with gray.

Clearly visible peaks at 2.4 Hz, 2.5 Hz, and 2.7 Hz in the FDD results confirm that all three frequencies define the dynamic behavior of the building. The fourth peak (present in results from both arrays) is at 3.8 Hz, which is in agreement with the results coming from SR analysis. Estimated mode shapes corresponding to the identified frequencies for 2.4 Hz, 2.5 Hz, and 2.7 Hz are presented in Figure 5.3.

The first mode at 2.4 Hz is the bending mode in the transverse X direction (Figure 5.3a). The modal shape at this frequency is the same for each unit. Modes at 2.5 Hz (Figure 5.3b) and 2.7 Hz (Figure 5.3c) do not provide clear mode shapes and are hard to visually interpret. The mode shapes for both frequencies seem to be different for each unit. At 3.8 Hz, the mode shapes presented in Figure 5.3d indicate a torsional mode. Each part of the building is moving separately with the vertical axis of rotation approximately in the middle of each unit.

5.1.2 Discussion

From the FDD analysis, the first mode of the structure has a frequency of 2.4 Hz and is related to the bending in the X direction. The other modes at 2.5 Hz and 2.7 Hz identified in both the spectral ratio and FDD analyzes did not provide very clear modal shapes. The mode shape at 3.8 Hz suggests that the building behaves as three separate units rather than one large structure, since three torsional axes are located approximately in the center of each unit. If the building were to rotate as one, only one axis of rotation would be at the center of unit 44 (the one in the middle). Such a complex shape (Figure 5.3) could be related to the coupling of the modes of different units, which are close to each other in the case of the building analyzed in the Matera experiment.

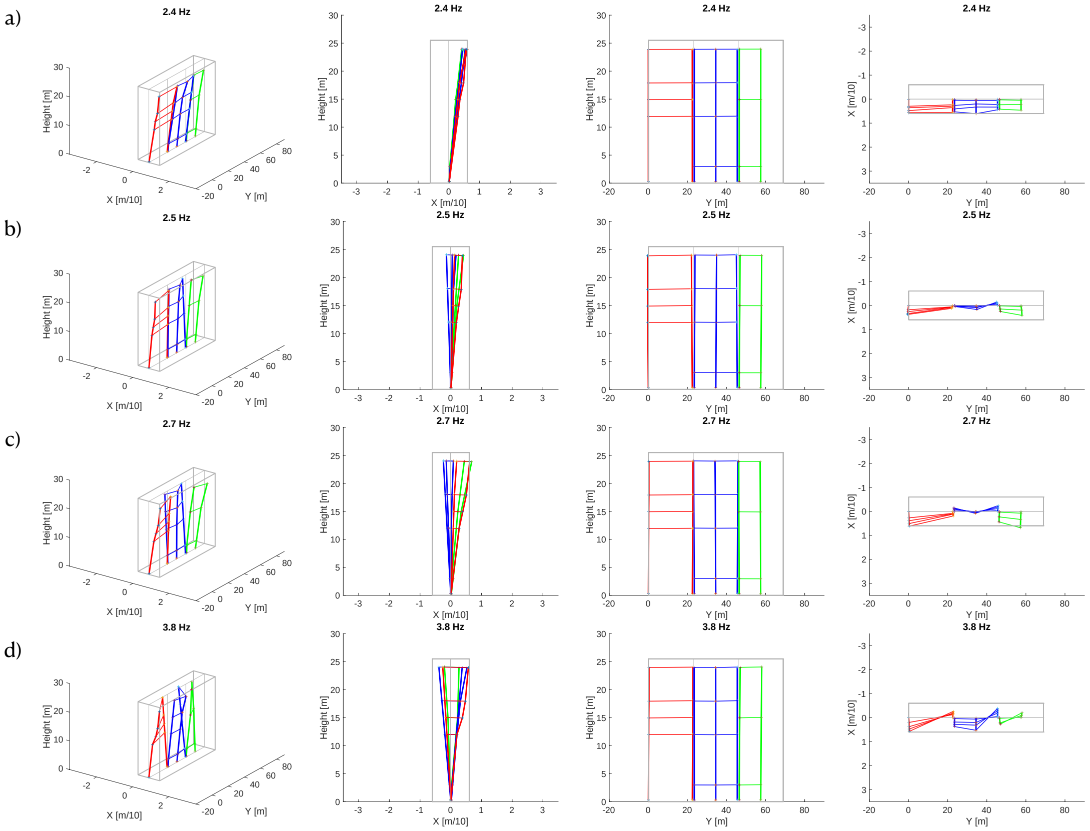

Figure 5.3: Estimated mode shapes of the four first modes of the building analyzed in the Matera experiment 2.4 Hz (a), 2.5 Hz (b), 2.7 Hz (c), and 3.8 Hz (d). The green lines represent unit 46, the blue lines unit 44, and the red lines unit 42. The gray lines indicate the outline of the undeformed building. The first column shows the 3D view, the second is the deformation in the X direction of the building, the third is the deformation in the Y direction, and the fourth shows the view from the top. Figures are not to scale.

Some other studies (e.g., Guéguen et al., 2016; Astorga et al., 2018; Pianese et al., 2018; Skłodowska et al., 2021) showed a co-seismic decrease of the resonant frequency during an earthquake. In the case of the Matera building, the comparison of the resonant frequencies from the noise spectral ratios with those obtained by the analysis of the earthquake data showed that the variation of the frequencies is insignificant. A possible explanation for this observation could be the small magnitude of the shaking caused by the recorded earthquake (peak acceleration in the North direction at the top of the building of 0.0012 m/s, and 5.23 x 10^{-4} m/s at the bottom).

The shapes of the spectral ratios differ between the earthquake and seismic noise inputs (Figure 5.1). As discussed by Ditommaso et al. (2012), this could be explained by the excitation of different modes by different inputs - earthquake or noise. The excitation of different modes is related to the different energy concentrations various inputs (Figure 5.4).

In the case of the Matera building, it is possible that the joints between the units are seismic joints (no engineering confirmation was available) and each unit primarily

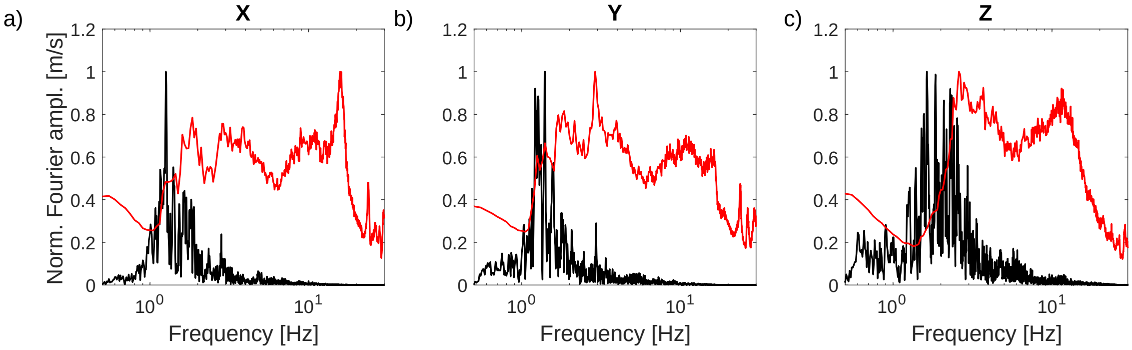

Figure 5.4: Normalized Fourier amplitude spectra of noise (red lines) and earthquake data (black lines) coming from sensor 105 in Array 1. a) The X component, b) the Y component, and c) the Z component.

behaves as a separate building. Since the stiffness is proportional to the square of the frequency (Clotaire et al., 2008), the very close frequency peaks observed in the data analyzed from the Matera building suggest that also the stiffness of the structure is similar in both directions. Considering the dimensions of the building, if it would behave as one structure, its stiffness would be greater in the Y direction (longer side of the building) compared to the X direction (much shorter side of the building), which is not the case. This observation supports the hypothesis that the presence of seismic joints causes the analyzed building to behave as three separate structures, even though the whole structure has a rectangular shape (the Y dimension is almost six times larger than the X dimension). However, to precisely identify the modes of the Matera building, a more precise modal analysis should be performed (e.g., a numerical model of the building, or an engineering evaluation of the connections between the units).

The analysis of the dynamic behavior of the building instrumented in the Matera experiment confirmed the complex vibrational characteristics of the building. For the needs of the proposed approach, however, it is not necessary to determine whether the building behaves as one structure or three. The results coming from both spectral ratio and FDD analyses clearly indicate the frequency range in which most of the vibrational energy is located and the resonant frequencies of the building. Therefore for further analysis data were bandpass filtered between 2 Hz and 10 Hz to analyze the frequency band where any possible interaction between the building and the soil is expected.

5.2 Deconvolution of the recordings from the building and the field

5.2.1 Results

Deconvolved wavefields of the simultaneous earthquake recordings from the instrumented building and the nearby athletic field using the sensor at the top of the building as the reference are presented for Array 1 (Figure 5.5) and Array 2 (Figure 5.6). Prior to the deconvolution, all data were bandpass filtered with a 4th-order Butterworth filter between 2 Hz and 10 Hz. The regularization parameter used in the deconvolution (equation 3.4), ε was set to 1 % of the average spectral power of u_2 (i.e., the reference signal).

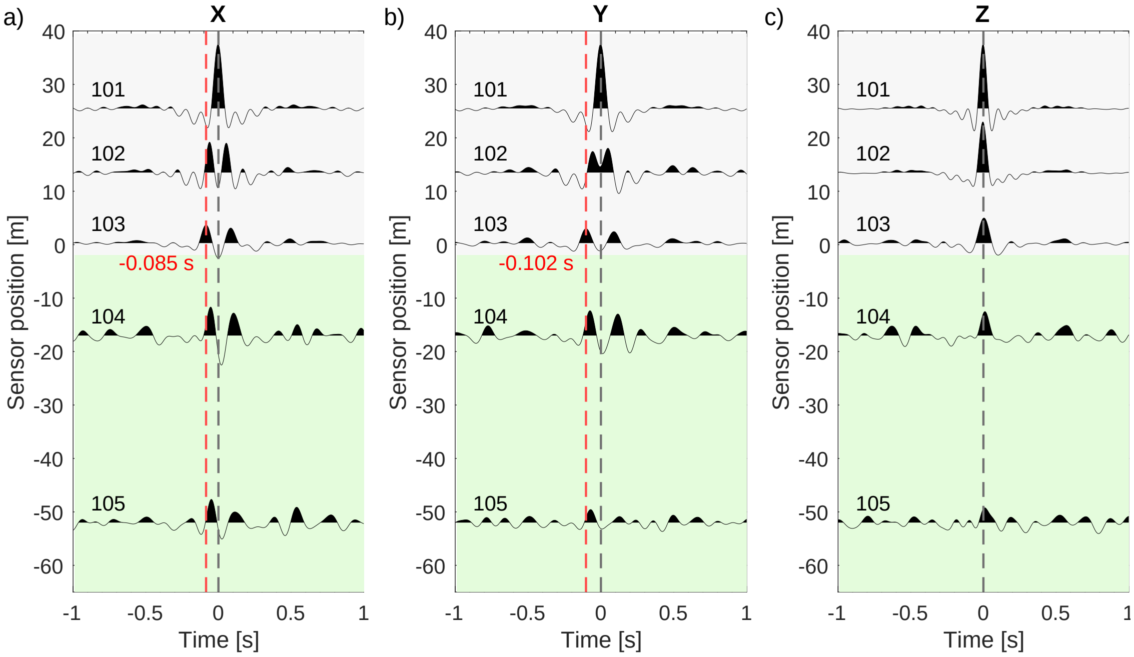

Figure 5.5: Deconvolved wavefields of the earthquake recordings bandpass filtered from 2 Hz to 10 Hz for Array 1 for a) X, b) Y and c) Z components. Results represent the deconvolved wavefield using the sensor at the top of the building (101) as a reference. Sensor offset equal to or greater than 0 indicates the height of sensors located in the building. Sensors offset below 0 indicates the horizontal distance of sensors installed in the field relative to the bottom sensor in the building. The time delay of the main peak in the acausal part (related to the up-going wave of the sensor at the bottom of the building) is indicated with red color in a) and b). In c) the wave propagation velocity is too high to observe peak separation. The gray background indicates sensors installed in the building. The green background indicates sensors installed on the athletic field.

In both arrays considered, the deconvolved wavefields of the recordings from sensors installed in the building, for both horizontal components (X and Y), show symmetrical peaks in the acausal and causal parts. Those peaks can be associated with the up- and down-going waves propagating within the structure (Snieder and Şafak, 2006). The wave propagation velocity in both directions was estimated based on the relation of the peaks delay and distance between sensors installed in each of the arrays (Table 5.1). v_X and v_Y are the wave propagation velocities in the X and the Y direction, respectively. The uncertainties of the velocity estiamtion are calculated as propagating error of the distance and travel time uncertainties (see Appendix A.2).

The deconvolved wavefields of the sensors installed on the athletic field are asymmetrical compared to the sensors from the building. In Array 1, sensors 104 and 105 have dominant peaks arriving simultaneously in the acausal part, regardless of the distance from the building. Additionally, the dashed vertical lines marked on the two horizontal components plots (Figure 5.5a, b) highlight the fact that the dominant peaks of the field sensors arrive closer to the time 0, compared to the sensor

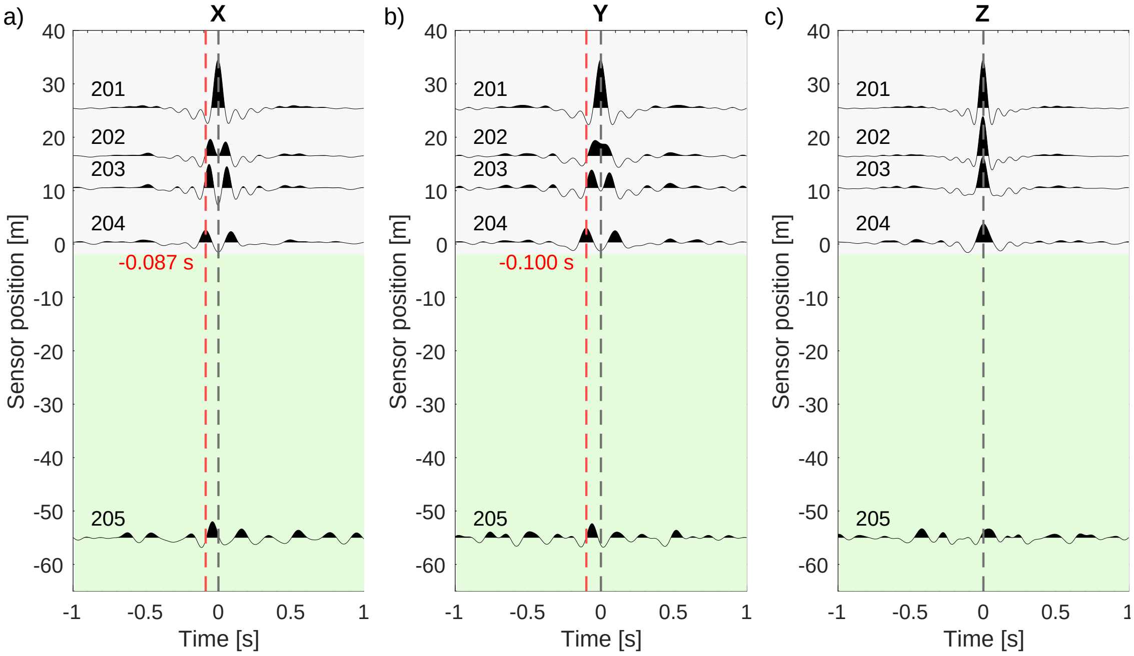

Figure 5.6: Deconvolved wavefields of the earthquake recordings bandpass filtered from 2 Hz to 10 Hz for Array 2 for a) X, b) Y and c) Z components. Results represent the deconvolved wavefield using the sensor at the top of the building (201) as a reference. Sensor offset equal to or greater than 0 indicates the height of sensors located in the building. Sensors offset below 0 indicates the horizontal distance of sensors installed in the field relative to the bottom sensor in the building. The time delay of the main peak in the acausal part (related to the up-going wave of the sensor at the bottom of the building) is indicated with red color in a) and b). In c) the wave propagation velocity is too high to observe peak separation. The gray background indicates sensors installed in the building. The green background indicates sensors installed on the athletic field.

Table 5.1: The wave propagation velocities in the building analyzed in the Matera experiment, estimated from the deconvolved wavefields. v_X and v_Y are the wave propagation velocities in the X and the Y direction, respectively.

Array	v_X	v_Y
1	300 m/s ± 89 m/s	250 m/s ± 62 m/s
2	293 m/s ± 85 m/s	290 m/s ± 65 m/s

installed at the bottom of the building (sensor 103).

In the deconvolved wavefield from Array 2, similar characteristics can be observed. As in Array 1, the deconvolved wavefield of the field recordings is asymmetric. The dominant peak in the acausal part of the deconvolved wavefield of the sensor installed in the field (205) is closer to time 0 than the sensor at the bottom of the building (204).

In both arrays, the separation of peaks in the vertical component (Z) is not visible in the deconvolved wavefield in the buildings.

5.2.2 Discussion

In the Matera test site, the ground level of the athletic field is higher than the level of the lowest sensor installed in the building. This geometry characteristic results in a loss of symmetry observed in the deconvolved wavefields of the sensors installed on the field. The elevation difference of around 7.5 m has a visible impact on the presented results. The same time delay of the peaks observed in the causal parts of the deconvolved wavefields of the sensors in the field can be explained by the nearly vertical incidence of the earthquake wavefront. Taking all this into consideration, it is likely that the wavefront arrived first at the bottom of the building and with a slight delay reached the sensors installed on the higher-altitude athletic field.

The lack of separation of the peaks in the deconvolution results of the Z component (Figures 5.5c and 5.6c) is most likely caused by the higher wave propagation velocity in this direction combined with low sampling rate of the instruments for such configuration. Since only the vertical component data is considered, the wave propagation velocity is close to the P-wave velocity (Parolai et al., 2009) leading to arrivals that are separated in time by less than the sampling interval (Bindi et al., 2015b) and in space by less than the vertical spacing of the sensors. Some peak separation that is visible in the wavefields of the field sensors is hard to properly identify in terms of velocity calculation, which could be caused by the insufficient resolution of the deconvolution results or by the presence of data analysis artifacts caused by noise.

The energy transmitted from the building to its surroundings is expected in the causal part of the deconvolved wavefields of the sensors installed on the athletic field. However, the causal part of the obtained deconvolved wavefields is complex. This could be caused by several factors such as the low energy of the registered earthquake, the presence of seismic noise originating from the surroundings of the building, or the geometry of the test site. The complexity of the causal part of the deconvolved wavefields coming from the sensors installed on the athletic field and the limited number of sensors installed on the field make it difficult to identify seismic phases related to the energy transmitted from the building to the ground. Therefore, in the following section an analytical model is introduced to overcome those limitations and identify the seismic phases corresponding to the transmitted energy from the vibrating building to its surroundings.

5.3 Seismic phase identification

5.3.1 Analytical model

The analytical model presented in this section defines a transfer function between the top of the building and a given sensor on the field. It was developed to identify and interpret seismic phases of the deconvolved wavefield related to the energy transmitted from the building to its surroundings. The geometry used for the model is presented in Figure 5.7. The proposed model, even if simplified, aims to explain the main features observed in the deconvolved wavefield. To simplify the model, attenuation is not considered, since the focus was on identifying the seismic phases related to the energy transmitted from the building to the ground, not on the amplitude changes.

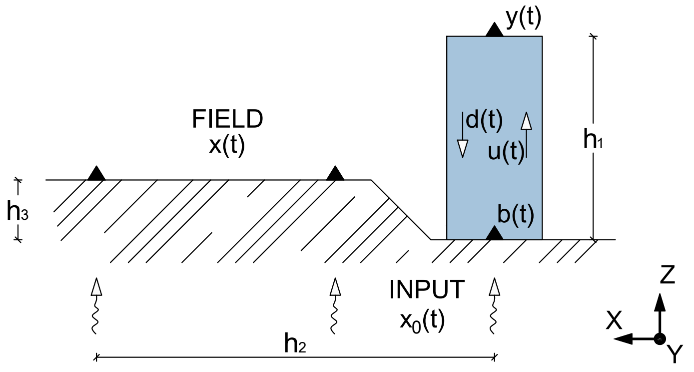

Figure 5.7: Schematic geometry of the Matera test site used for the analytical model. The building is indicated by the blue rectangle on the right. h_1 is the height of the building, h_2 is the horizontal distance of a sensor in the field from the sensor installed at the bottom of the building, h_3 is the vertical distance from the bottom of the building to the level of the athletic field. $x(t)$ defines the recordings of the sensors on the athletic field, and $y(t)$ and $b(t)$ are the recordings at the top and bottom of the building, respectively.$u(t)$ and $d(t)$ are the up- and down-going waves in the building. $x_0(t)$ is the input ground motion.

As described in section 3.3.1, I make the assumption that the input is a vertically propagating plane wave, $x_0(t)$. The building is described by the shear-beam model and it is modeled as a layer over a soil layer. As indicated in Figure 5.7, the waves propagating in the building can be decomposed into up-going, $u(t)$, and down-going $d(t)$ waves. In the time domain, they are defined as

$$u(t) = (1 + r)x_0(t - \tau_1) + (-r)d(t - \tau_1) \tag{5.1}$$

and

$$d(t) = u(t - \tau_1) \tag{5.2}$$

where τ_1 is the time delay corresponding to the wave propagation with velocity v_X or v_Y (depending on the considered component) in the building with the height equal to h_1. r is the reflection coefficient and $1 + r$ defines the transmission coefficient of the boundary soil-building (see Section 2.1).

Since the building is modeled as a layer over a soil layer, the free surface condition applies and the signal at the top is defined as

$$y(t) = 2u(t). \tag{5.3}$$

In the proposed model, the recording at the position of the field sensor is defined by the equation

$$x(t) = 2x_0(t - \tau_3) + \frac{(1 - r)}{2} y(t - \tau_1 - \tau_2 - \tau_3) \tag{5.4}$$

where τ_2 is the time delay of a wave propagating with the velocity V_2 through the distance from the bottom of the building to a field sensor approximated as $\sqrt{h_2^2 + h_3^2}$. τ_3 is related to the wave travel time in the soil considering the vertical elevation of the athletic field, with respect to the base of the building, h_3, and velocity V_3. In the frequency domain, Equation 5.4 is expressed as

$$X(f) = 2X_0 e^{-i2\pi f \tau_3} + (1 - r)Y(f)e^{-i2\pi f(\tau_1 + \tau_2 + \tau_3)} \tag{5.5}$$

By combining Equations 5.1, 5.2, and 5.3 a new equation is obtained where the recording at the top $y(t)$ is dependent only on the input $x_0(t)$

$$\frac{y(t)}{2} = (1+r)x_0(t-\tau_1) + \frac{-r}{2}y(t-2\tau_1). \tag{5.6}$$

After transformation of $y(t)$ to the Fourier domain, $Y(f)$ is expressed as

$$\frac{Y(f)}{2} = (1+r)X_0(f)e^{-i2\pi f\tau_1} + \frac{-r}{2}Y(f)e^{-i2\pi f2\tau_1}. \tag{5.7}$$

After transformation and simplification of Equation 5.7, the input $X_0(f)$ can be defined as

$$X_0(f) = Y(f)\frac{1}{2(1+r)}[e^{-i2\pi f(-\tau_1} + re^{-i2\pi f\tau_1}]. \tag{5.8}$$

By substituting X_0 in Equation 5.5 with Equation 5.8, $X(f)$ can be expressed as

$$X(f) = Y(f)\frac{1}{1+r}[e^{-i2\pi f(-\tau_1} + re^{-i2\pi f\tau_1}] + (1-r)Y(f)e^{-i2\pi f(\tau_1+\tau_2+\tau_3)} \tag{5.9}$$

By dividing Equation 5.9 by $Y(f)$, the analytical transfer function for a sensor in the field, $x(t)$, with a virtual source at the top of the building, $y(t)$, can be therefore described in the Fourier domain by

$$\frac{X(f)}{Y(f)} = P_1 + P_2 + P_3 \tag{5.10}$$

where

$$P_1 = \frac{1}{1+r}e^{-i2\pi f(-\tau_1+\tau_3)}, \tag{5.11}$$

$$P_2 = \frac{r}{1+r}e^{-i2\pi f(\tau_1+\tau_3)}, \tag{5.12}$$

and

$$P_3 = \frac{(1-r)}{2}e^{-i2\pi f(\tau_1+\tau_2+\tau_3)}. \tag{5.13}$$

P_1 and P_2 correspond to the wave propagation within the building (since the deconvolution is performed using a sensor at the top of the building as the reference) and P_3 describes the phase related to the energy transmitted from the building to its surroundings. $(1-r)/2$ in Equation 5.13 is the estimate of the amplitude of the transmitted energy.

The wave propagation velocity in the building calculated from the relation of the time delay of the phases of the deconvolved wavefield and the distance between sensors included significant uncertainties (up to 89 m/s, see Table 5.1). Therefore τ_1, corresponding to the wave propagation velocity in the building used in the analytical model, was estimated using a simple model similar to the one proposed by Snieder and Şafak (2006) (without considering attenuation). The model defines the transfer function of the building in the frequency domain, $B(f)$, using the signal at the top of the building as a reference:

$$B(f) = \frac{1}{2}e^{-i2\pi f(-\tau_1)} + \frac{1}{2}e^{-i2\pi f\tau_1} \tag{5.14}$$

5.3.2 Results - analytical model fit

In this study, to find the best fitting parameters describing models of the transfer functions defined by Equations 5.10 and 5.14, a grid search approach (e.g., Parolai et al., 2010) performed in the frequency domain was used. The parameters providing the best fitting model were chosen based on the minimum misfit function defined by $RMSLE$ (equation 3.5). For the models, densities $\rho_1 = 250$ kg/m3 for the building and $\rho_2 = 1800$ kg/m3 for the soil were used. In the developed model the density values impact only the impedance contrast included in the reflection coefficient r and not the time delay, which is the primary information searched for in this approach. Therefore the use of approximate densities, without in-detail parameter computation, is sufficient for this study. However, it is important to keep in mind that the density, ρ, is related to the seismic velocity and the values chosen for the model should be consistent with the velocity results.

The search for the best-fitting parameters for the models was divided into two parts:

1. estimation of the wave propagation velocity in the building based on the time delay τ_1 using Model 5.14 (Figures 5.8a,c and 5.9a,c),

2. estimation of the τ_2 and τ_3 defining velocities of the wave propagation in the soil (V_2 and V_3), using Model 5.10 and previously estimated τ_1 (Figures 5.8b,d and 5.9b,d).

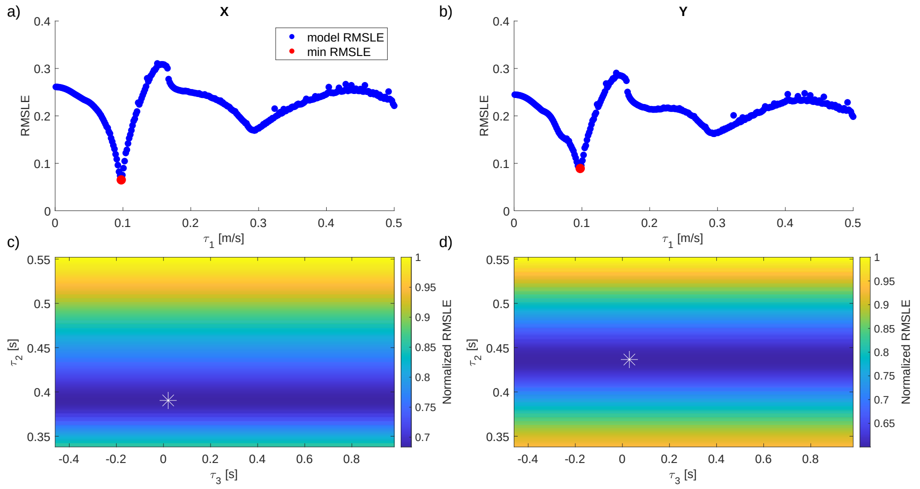

Figure 5.8: The grid search results for the X (a,c) and Y components (b,d) of sensor 105 from Array 1. a) and b) show grid search of τ_1 from fitting Model 5.14. τ_1 values providing minimum $RMSLE$ are indicated with red dots. c) and d) show grid search of τ_2 and τ_3 from fitting Model 5.10. White asterisks indicate τ_2 and τ_3 values combination providing minimum $RMSLE$.

The wave propagation velocities calculated using time delays providing the minimum $RMSLE$ of the models (Figures 5.8 and 5.9) are presented in Table 5.2.

The model is much less sensitive to the vertical propagation velocity of the input wave, V_3, than the horizontal propagation velocity, V_2 (i.e., similar $RMSLE$ values for different τ_3 values considered in the grid search – see Figures 5.8a,d and 5.9c,d). V_3 has therefore a low impact on the model and the convergence to the minimum

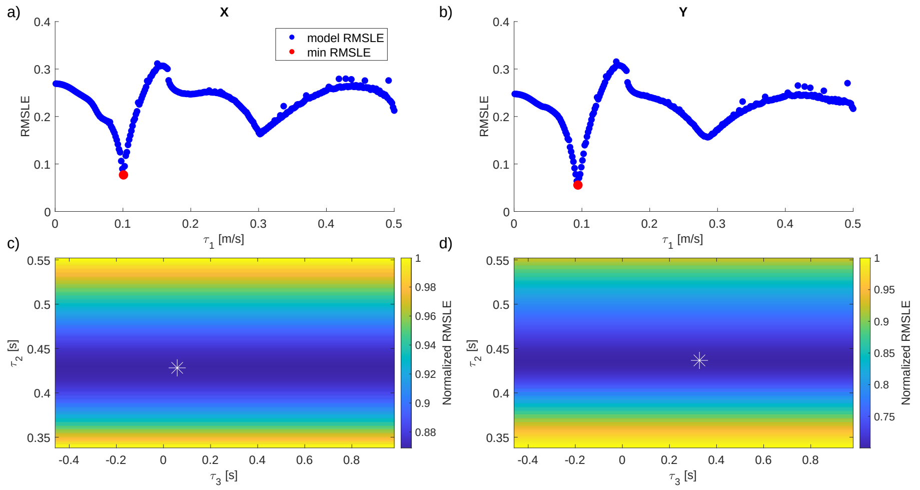

Figure 5.9: The grid search results for the X (a,c) and Y components (b,d) of sensor 205 from Array 2. a) and b) show grid search of τ_1 from fitting Model 5.14. τ_1 values providing minimum $RMSLE$ are indicated with red dots. c) and d) show grid search of τ_2 and τ_3 from fitting Model 5.10. White asterisks indicate τ_2 and τ_3 values combination providing minimum $RMSLE$.

Table 5.2: Wave propagation velocities in the building and the soil calculated using time delay values, providing the minimum $RMSLE$ of the analytical model used for Matera data analysis. The uncertainties are estimated based on propagating error calculation (see Appendix A.2).

	Component	V_b [m/s]	V_2 [m/s]	V_3 [m/s]
Array 1	X	262 ± 8	135 ± 3	364 ± 15
	Y	262 ± 8	120 ± 3	253 ± 8
Array 2	X	253 ± 8	130 ± 3	270 ± 9
	Y	271 ± 8	127 ± 3	335 ± 13

value is worse than for the V_2 search. This explains the greater difference between the V_3 values presented in Table 5.2 compared to V_b and V_2.

Comparison of the transfer functions calculated using the time delays (τ_1, τ_2 and τ_3) that provided minimum $RMSLE$, and the real data is shown in Figure 5.10. The best-fitting transfer functions in the time and frequency domains are indicated with purple lines. Additionally, in the time domain, the vertical red dashed lines highlight the peaks of the identified seismic phases related to the part of the wavefield transmitted from the building to the ground (equation 5.13).

The analytical models are simpler than the real data deconvolved wavefields, both in the frequency and time domains. In the frequency domain, models fit only some of the troughs of the real data results. In the X direction, for the sensors with the largest distance from the building (i.e. 105 and 205), the model fits well the first trough at 2.5 Hz. The model of sensor 104, which is the closest to the building, does not describe this trough at all. The second trough defined by the model is at around 7.5 Hz. However, in real data, it is observed only in the results from the Array 1 and not in the data from Array 2. In the Y component, similar to the X component results, the first trough at 2.5 Hz is captured by the model only for sensors 105 and 205. The second trough at 7.6 Hz is the only peak in the considered frequency range

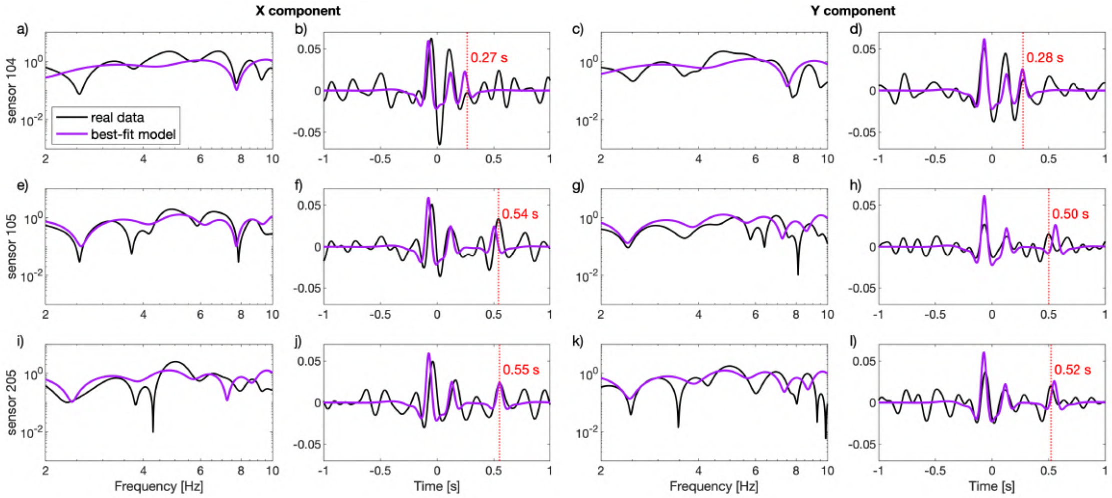

Figure 5.10: Comparison of the real data deconvolved wavefield (black lines) and analytical solution (purple lines) for sensors in the field: a)-d) 104, e)-h) 105 and i)-l) 205. The first and second columns present the model fit of the X component in frequency and time domains, respectively. The same for the third and fourth columns of the Y component. The black line is the real data transfer function, and the purple line is the analytical solution (equation 5.10). Red vertical lines indicate the identified seismic phases of the real data deconvolved wavefield related to the wavefield transmitted from the building to the athletic field. The time delays of the selected phase peaks are written on the plots.

shown by the model for sensor 104. The model for sensor 105 in the Y direction has a double trough at around 7.5 Hz, however, it does not accurately describe the troughs in the real data. The real data results are more complex than the model at higher frequencies.

After calculating the inverse Fourier transform, the models identified three peaks in the time domain. Despite a small shift in the X direction, the first two peaks related to the wave propagation within the building (one in the causal and one in the acausal part, described by P_1 and P_2 in Equations 5.11 and 5.12) are well identified. The third peak of the analytical model is described by P_3 (equation 5.13) and is related to the part of the wavefield transmitted from the building to its surroundings. The analytical solutions for sensor 205 (Figure 5.10j, l) more accurately fit the real data in both components, compared to those of sensor 105 (Figure 5.10f, h). The phase shift of the peaks between the real data and the best-fitting model can be observed in the solutions of sensor 105. The solution of sensor 104 (Figure 5.10b, d) is defined accurately in the time domain for both components, even though there is a small phase shift of the two dominant peaks in the X component of the deconvolved wavefield. The shift of the two dominant peaks in the analytical models with respect to the real data transfer function is observed for all the sensors in the X component, in contrast to the Y component, where the fit is good.

By comparing the real data results with the analytical models, the third peak of the model described by P_3 (Equation 5.13) identified the part of the deconvolved wavefield transmitted from the building to the athletic field. They have time delays of around 0.27 s (X component) and 0.28 s (Y) for sensor 104; 0.54 s for X, and

0.50 s for Y for sensor 105; and 0.55 s (X) and 0.52 s (Y) delay for sensor 205 (red dashed vertical lines in Figure 5.10).

5.3.3 Constrained deconvolution

To select the time interval for the positivity constraint used in the constrained deconvolution method, I selected the time intervals around the phase peaks identified by the best-fitting models in the previous step. The selected time intervals were chosen to contain both horizontal peaks of the deconvolved wavefield from the considered sensor. The selected time interval for sensor 105 in Array 1 was between 0.42 s and 0.60 s, and for sensor 205 Array 2 was between 0.39 s and 0.62 s. For sensor 104, the peaks describing phases related to the energy radiated from the building were too close to the dominant peak in the causal part of the deconvolved wavefield and therefore peak separation for the constrained deconvolution was not possible and was not considered in this study.

The deconvolved wavefield and the constrained deconvolved wavefields of sensors 105 and 205 are shown in Figures 5.11a and 5.12a, respectively. The time intervals (gray areas) define the positivity constraint used for the phase selection of the deconvolved wavefield based on the identification of the peaks in the previous step. The blue dashed lines indicate the constrained wavefield of the deconvolved signal (black lines). The Fourier spectra of the deconvolved (black line) and the constrained deconvolved wavefield (dashed blue line) are presented in Figures 5.11b-d and 5.12b-d. When comparing both spectra, for both horizontal components the troughs of the transfer functions around the resonant frequencies of the structure (2 -3 Hz) are below the amplitudes of the constrained spectra. The constrained spectra, which in the time domain contain only one peak for each component (Figures 5.11a and 5.12a), are much smoother than the spectra of the deconvolved wavefield of the real data.

The smoothed spectra of the recordings at the top of the building (purple lines), on the athletic field (orange lines), and the spectra of the reconstructed signal related to the wavefield transmitted from the building to the ground (green lines) are compared in Figures 5.11e-g for Array 1 and 5.12e-g for Array 2. The spectra of the reconstructed signal (green lines) are obtained by convolution of the constrained spectra (dashed blue lines in Figures 5.11b-d and 5.12b-d) with the spectra of the top sensor recordings (purple lines in Figures 5.11e-g and 5.12e-g). The orange lines presenting the Fourier amplitude spectra of the recordings of the analyzed field sensors are shown for comparison.

5.3.4 Energy of the radiated wavefield

To evaluate the influence of the presence of the building on the ground motion at the nearby athletic field, the energy of the wavefield radiated from the analyzed building into its surroundings was estimated. The energy was calculated as the integral of the power spectral density (PSD) within the frequency band 2 Hz - 10 Hz (as used for the analysis). By rewriting Equation 5.5, I obtained an equation defining the input motion, X_0, at the surface of the athletic field:

$$2X_0(f)e^{-i2\pi f\tau_3} = X(f) - \frac{1-r}{2}Y(f)e^{-i2\pi f(\tau_1+\tau_2+\tau_3)} \tag{5.15}$$

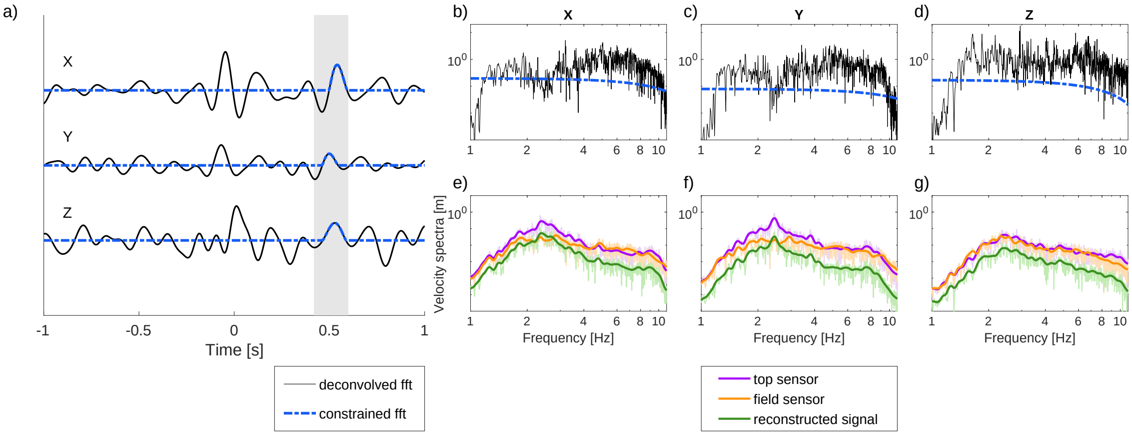

Figure 5.11: Example of the constrained deconvolution for sensor 105 from Array 1. a) deconvolution time history of all three components, indicated with a black solid line. The time interval for the constrained phase selection is marked by a gray shade. The blue dashed lines indicate the constrained deconvolution in time. b) - d) Fourier spectra of the deconvolved wavefields shown by the corresponding colors. e) - g) comparison of the Fourier spectra of the signal recorded by the sensor at the top of the building (purple line), the signal registered by the sensor in the field (orange line), and the reconstructed motion (green line). The more intense colors represent the smoothed spectra of the corresponding light-colored spectra.

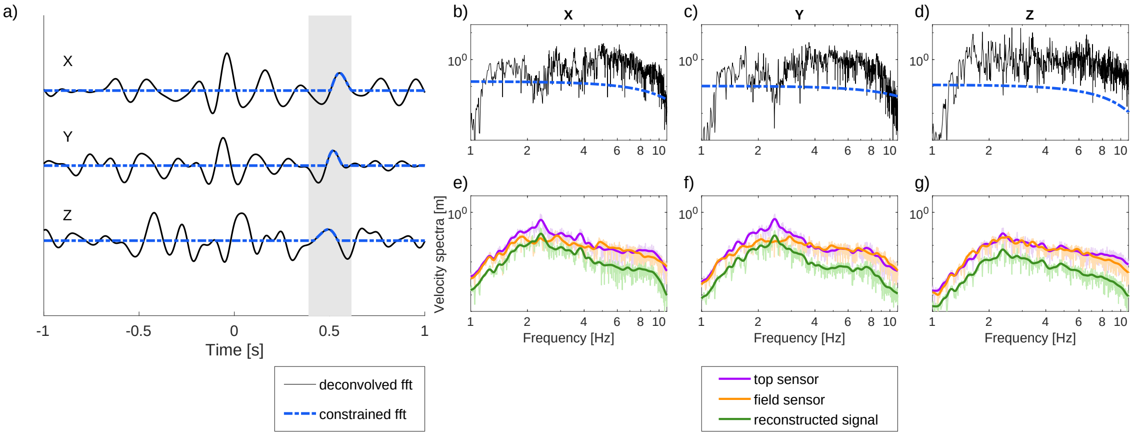

Figure 5.12: Same as Figure 5.11 but for the sensor 205 from Array 2.

The input motion at the surface (left side of the Equation 5.15) accounts for the free surface boundary condition (multiplication by 2) and time delay, τ_3, considering the vertical elevation of the athletic field, with respect to the base of the building, h_3.

Equation 5.15 states that to obtain the ground motion that would be recorded without the influence of the energy radiated from the vibrating building, the transmitted part of the signal should be subtracted from the signal recorded by the field sensor. A comparison of the reconstructed input (without the influence of the building), the recorded signal, and the reconstructed signal related to the energy transmitted from a vibrating building are shown in Figure 5.13 (for sensor 105) and Figure 5.14 (for sensor 205).

The reconstructed signals, obtained by inverse Fourier transforms of the reconstructed spectra (green lines in Figure 5.11e-g and 5.12e-g) differ from those recorded

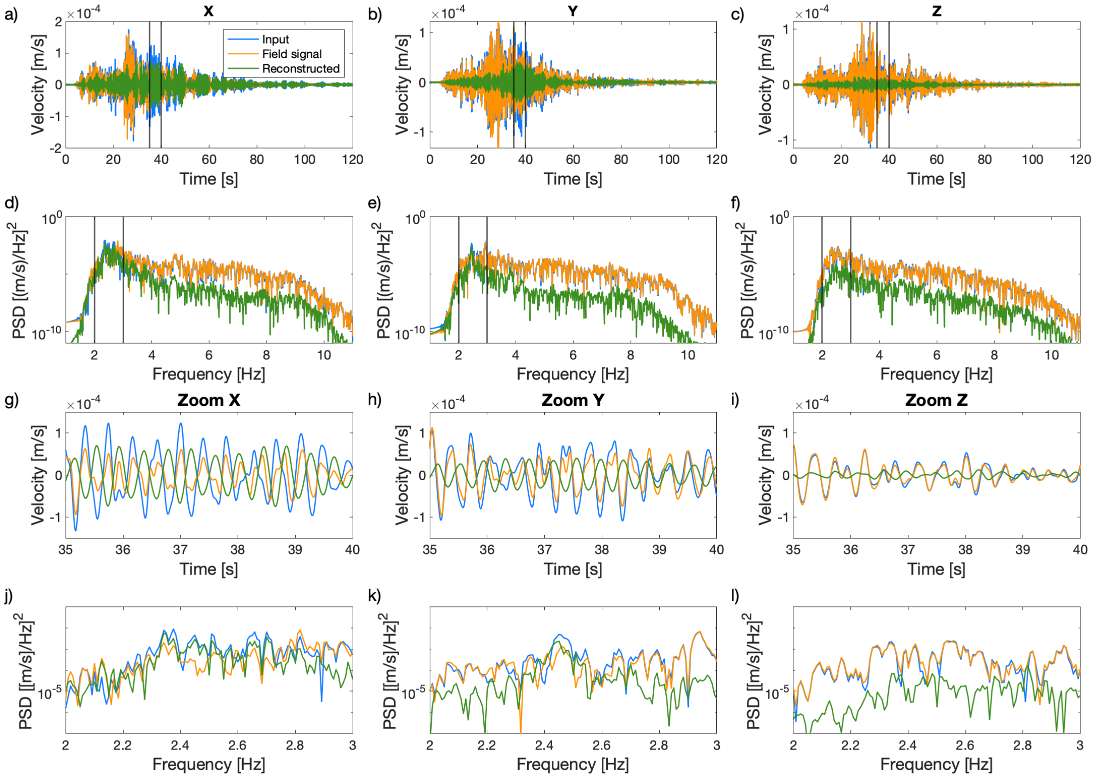

Figure 5.13: Comparison of the reconstructed input signal (blue lines), the signal recorded by sensor 105 from Array 1 (orange lines), and the reconstructed signal related to the energy transmitted from the building to the ground (green lines). Plots a-c show the time history of the signals. Plots d-f show their Fourier amplitude spectra. Plots g-i show the zoom on the 5 s time interval with the most energetic part of the reconstructed wavefield marked with black vertical lines in plots a-c. Plots j-l show the zoom on the frequency interval indicated by black vertical lines in plots d-f.

by both field sensors. The difference is visible both in the shape and the amplitudes (Figures 5.13a-c,g-i, and 5.14a-c,g-i). The biggest difference is visible for the Z component, where the reconstructed motion has a much smaller amplitude compared to the original signal. Additionally, on the plots presenting the zoom between 35 s and 40 s (the time interval with the highest amplitude of the reconstructed signal) of the time histories (Figures 5.13g-i and 5.14g-i) a 180 °phase shift is visible for the two horizontal components. Therefore, the presence of the vibrating building produced wavefields that were out of phase with the reconstructed input signals in the two horizontal components (Figure 5.13 and 5.14g-i).

In the considered frequency band, 2 Hz - 10 Hz, the calculated energy of the signals from Array 1 (sensor 105) implies that the reconstructed signal related to the wavefield radiated from the building to the ground is around 59 % of the energy of the signal registered by the sensor 105 for the X component. The Y component of the signal is less affected by the transmitted wavefield in the building - it is around 17 % of the recorded signal. The lowest impact on the recording in the field is in the vertical component and is around 3 %.

In Array 2, the energy of the reconstructed signal transmitted from the building to the ground is approximately 30 % of the recorded signal in the X direction. In

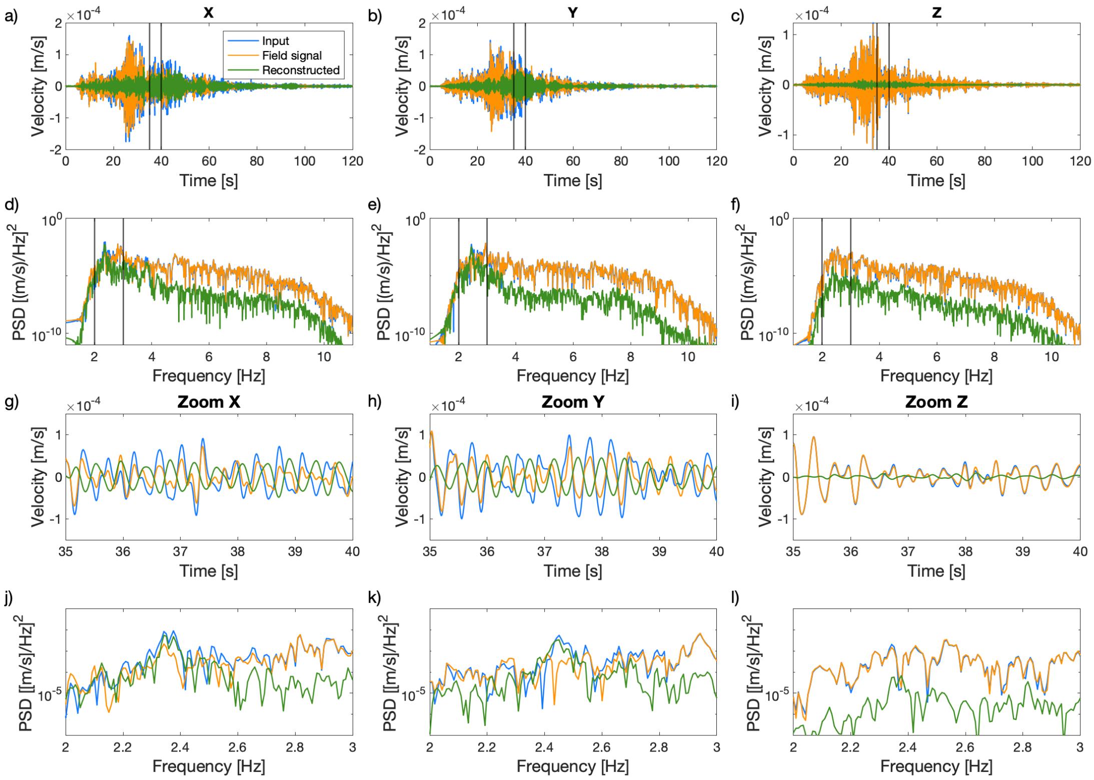

Figure 5.14: Comparison of the reconstructed input signal (blue lines), the signal recorded by sensor 205 from Array 2 (orange lines), and the reconstructed signal related to the energy transmitted from the building to the ground (green lines). Plots a-c show the time history of the signals. Plots d-f show their Fourier amplitude spectra. Plots g-i show the zoom on the 5 s time interval with the most energetic part of the reconstructed wavefield marked with black vertical lines in plots a-c. Plots j-l show the zoom on the frequency interval indicated by black vertical lines in plots d-f.

the Y direction, similar to the results from Array 1, it is less, around 24 %. The lowest percentage of the calculated recorded signal energy is for the Z component, around 1 %.

When comparing the energy of the signal recorded by the sensors installed in the field and the reconstructed input without the impact of the existing building, the results show that in Array 1 the input is around 153 % of the original signal in the X component, 122 % in the Y component and 99 % in the vertical component. In Array 2, the energy is smaller for the X component - 135 %, and similar for the other components: 121 % for the Y component and 99 % for the vertical.

5.3.5 Discussion

The velocities of the wave propagation in the structure are estimated assuming pure shear behavior and, therefore, no velocity dispersion (Guéguen et al., 2019). This means that the velocity in the building, V_b, is the same over the analyzed frequency interval. In the building instrumented during the Matera experiment, the wave propagation velocities in both horizontal directions calculated from the analytical model are similar. Considering that the wave propagation velocity in the building is directly related to the stiffness (Clotaire et al., 2008), the discrepancies between the plane dimensions of the building (69 m vs 12 m) suggests that the building should be much stiffer in the Y direction (69 m) than in the X direction (12 m). The similar values in both X and Y directions obtained from the model suggest that the analyzed structure behaves as three separate buildings (23 m x 12 m) than as one big (69 m x 12 m). A similar conclusion was obtained from the estimation of the dynamic behavior of the building in the first step of the approach. In case the structure would behave as a single, large building, the difference in dimensions would be highlighted by the velocity and frequency results.

The results from the grid search provided information about the wave propagation velocities both in the building and in the soil (Table 5.2). Based on the obtained τ_2, the estimated velocities of the wave propagation in the soil, V_2, were below the S-wave velocity for the upper soil layer in Matera (Table 4.2), even considering their significant uncertainties. They are, however, close to the S-wave velocity estimated for the top sand layer in the test site during the experiment, V_S = 150-200 m/s (Lorenzo Petronio, personal communication). However V_3, which corresponds to the estimated τ_3 of the input wave propagation over the vertical uplift of the athletic field, is within the upper limit of the sand S-wave velocity estimated by Gallipoli and Lupo (2012).

The spectra of the deconvolved wavefield of the sensors installed on the athletic field (Figure 5.7) show several features (e.g., many troughs) that are not reproduced by the simple analytical model. The troughs present in the real data spectra may be related to the influence of sources other than the input and the radiated energy on the deconvolved wavefield (e.g., wave reflections caused by the geometry of the test site). The model developed based on the simplified geometry of the Matera test site, however, identified the three main phases of the deconvolved wavefield well. Two of these are associated with the up- and down-going wavefield in the building (P_1 and P_2), and the third is related to the energy transmitted from the building to its surroundings (P_3).

The fit of the analytical transfer function in the frequency domain is better for the X component. Also, the third peak of the model related to the transmitted energy, P_3, fits the peaks of the deconvolved wavefield better in the X component than the Y. This could be explained by the orientation of the analyzed arrays, which are aligned in the X direction with respect to the building. Additionally, the differences between the analytical and the real data transfer functions for both horizontal components are most likely caused by simplified model assumptions (such as no coupling between the building and the soil), and the simplified model geometry of a complex experimental setup.

The apparent better fit of the analytical transfer in the time domain is caused by the assumptions of the model. In the time domain, there are only three peaks of the model that are fitted, and therefore the good fit is obtained only for those three phases, and all the other phases of the deconvolved wavefield are neglected. However, in the frequency domain, the search of the parameters describing the best fitting analytical transfer function is done over the frequency band describing the whole time domain.

The clear peaks of the Fourier amplitude spectra of the reconstructed signals imply that the dominant frequencies of the horizontal components are strongly affected by the resonant frequency of the building (5.11e-g and 5.12e-g). These results are in agreement with results reported by Petrovic and Parolai (2016) and Petrovic et al. (2018) in their joint analysis of the data recorded by sensors installed in buildings and nearby boreholes, where similar behavior was observed.

The difference in the reconstructed signal for the two horizontal components might be caused by the location of the field sensors with regard to the main axes of the building, and therefore the influence of modes on the transmitted wavefield. This could explain the higher amplitudes of the X component of the reconstructed signal compared to the Y component. Additionally, the low amplitudes of the transmitted signal's vertical component could be connected with the negligible rocking of the building during recorded motion. The smaller transfer of energy from the building in the vertical component compared to the horizontal components could be also due to the difference in the impedance for shear waves (from the horizontal components analysis) and the P-wave (obtained by the vertical component analysis).

There were only two sensors that recorded the earthquake at a sufficient distance from the vibrating building to provide data for the reconstruction of the radiated wavefield. Considering the estimated wave propagation velocity (corresponding to V_2) is around 130 m/s and the most energetic frequencies of the building vibration are between 2.4 Hz and 2.7 Hz, the estimated wavelength is around 48 m - 54 m. This wavelength corresponds to the approximate distance of the sensors from the building. Thus, a sensor installed at a distance of half a wavelength from the building should provide the reconstructed wavefield in phase with the input, and therefore amplified due to the positive interference of the ground motion with the wavefield radiated from the building.

A comparison of the energy of the wavefield radiated from the building and the energy of the reconstructed input signal (without the influence of the existing building) in the limited frequency band showed that the impact of the building on the ground motion is significant for the horizontal components.

In the case of the Matera experiment, the wavefield radiated from the building is out of phase with respect to the reconstructed input signals (Figure 5.13g-i and 5.14g-i). Consequently, ground motion recorded by sensors 105 and 205 (installed at distances 50 m and 60 m from the building respectively) is influenced by the negative interference of the radiated wavefield, and therefore their energies are smaller than those of the input signal. The reconstructed radiated wavefield is a significant part of the signal recorded in the surroundings of the building and its energy is up to 59 % of the field signal in the direction of the wave propagation from the building (X).

5.4 Polarization analysis

5.4.1 Results of the polarization ellipse parameters estimation

Based on the approach for polarization analysis proposed by Pinnegar (2006), the polarization ellipse parameters for all three deconvolved wavefields of the sensors installed on the athletic field were estimated. The S-transform, showing the deconvolved wavefields energy distribution in time and frequency, of all three components of each sensor used for the ellipse parameters calculation can be found in the Appendix A.3 (Figures A.1, A.2 and A.3).

An example of all of the estimated polarization ellipse parameters of the deconvolved wavefield of the recordings coming from sensor 105 in Array 1 is presented in Figure 5.15 with the corresponding deconvolved wavefield of all three components. The time interval identified as the part of the wavefield radiated from the building to the ground (Section 5.3.1) is highlighted in gray. The same interval is marked with black lines on the S-spectra plots (panels c-f). Figure 5.15 shows the S-spectrum of the semi-major and semi-minor axes, the difference between them, and the total power. The polarization ellipse parameters for the two remaining sensors, sensors 104 and 205, are presented in Appendix A.3. The polarization ellipses composing the analyzed signal are described by eight parameters (Section 2.2), however, their ellipticity and linearity are described by the ellipse axes and their difference.

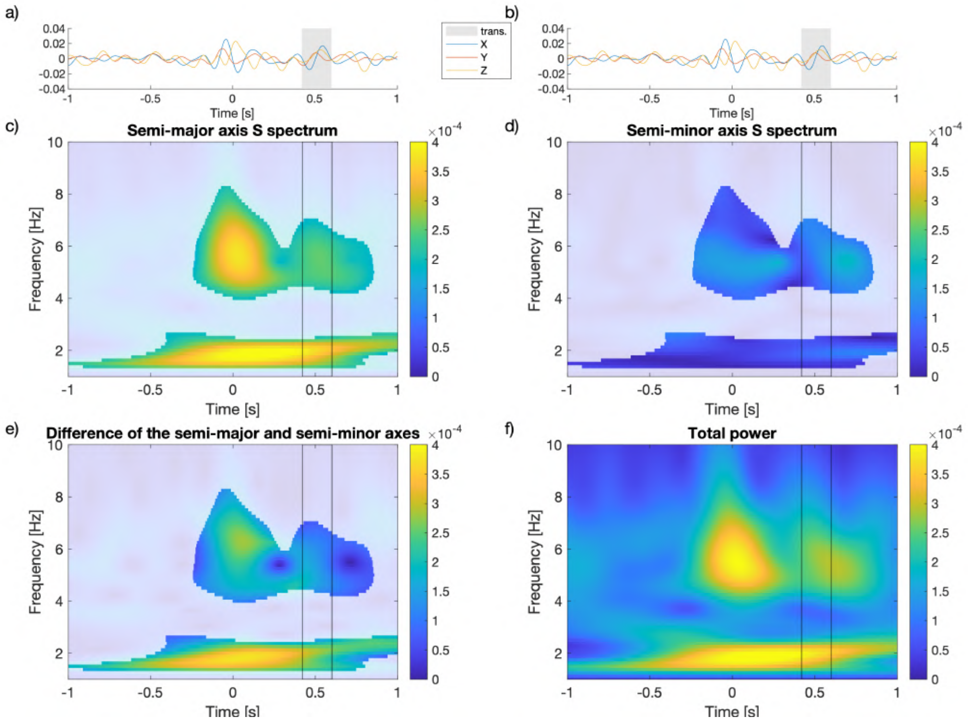

Figure 5.15: The ellipse parameters for sensor 105 from Array 1. a-b) the three components of the deconvolved wavefield used for the analysis. The gray rectangle indicates the considered time interval, corresponding to the seismic phases related to the energy transmitted from the building to its surroundings. c) Semi-major axis S-spectrum. d) Semi-minor axis S-spectrum. e) S-spectrum of the difference between semi-major and semi-minor axes. f) Total power S-spectrum. In time-frequency plots, black thin lines indicate the time interval corresponding to the gray patch from a) and b). The more pronounced colors indicate values where the total power of the S-spectrum (f) is greater than 50 % of the maximum power.

To focus the analysis on the most energetic parts of the signal, only values of each S-spectrum matrix larger than 50 % of the total power S-spectrum (Figure 5.15f) were considered. The corresponding values are indicated by more intense colors in S-spectra in Figure 5.15c-e. The results of all three analyzed sensors showed that the parts of the time-frequency domain within selected time intervals with the highest energy are distributed in the two frequency bands, 1 Hz - 3 Hz and 4 Hz - 8 Hz. The distribution of the three parameters that define the circular and linear polarization ellipse parts (semi-major, semi-minor, and their difference) from the constrained S-spectrum is presented in Figure 5.16, for the two distinct frequency bands.

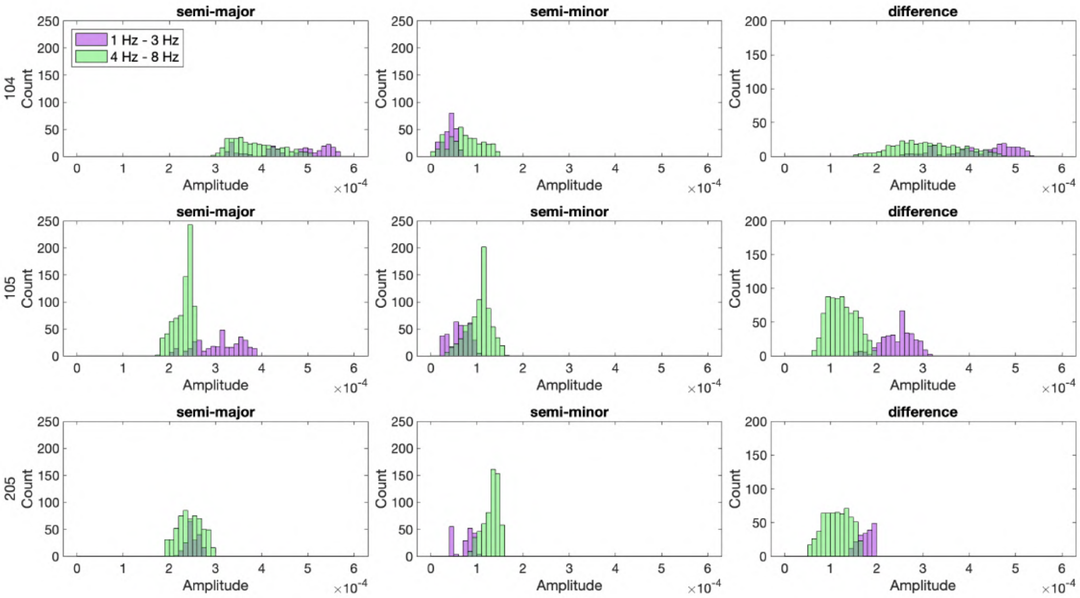

Figure 5.16: Distribution of the semi-major and semi-minor axes and their difference, for the considered time interval related to the identified deconvolution peaks. Data is separated into two frequency bands: purple corresponds to 1 Hz - 3 Hz and green to 4 Hz - 8 Hz.

Distributions of the selected polarization ellipse parameters show that the wavefield of sensor 104, which is the closest to the analyzed building, has higher amplitudes of the semi-major axis than the two other sensors farther from the structure in both considered frequency intervals (1 Hz - 3 Hz and 4 Hz - 8 Hz). The distribution of the semi-minor axis amplitudes, however, is relatively similar for all three sensors. Based on the dissimilarity of the two mentioned parameters, the distribution of the difference between both axes is expected - higher difference values are observed for sensor 104 than for the two sensors farther in the field.

The difference between sensor 104 and the two others is also visible in the shape of the parameter distributions. The ellipse parameters of motion recorded by sensor 104 are distributed over a wider range of values than the results of sensors 105 and 205 in both frequency bands. However, considering the values of the analyzed parameters, the dominant polarization in both frequency bands and for both sensors in Array 1 is linear (defined by the difference between the semi-major and semi-minor axes), and the circular part (semi-minor axis) is not very significant. Sensor 205 from Array 2 shows similar behavior to sensor 105 from Array 1. A small difference can be observed in the results from the interval of 1 Hz - 3 Hz, where the amplitude distribution of the semi-major axis is less wide, and the amplitude values are smaller than those of sensor 105.

5.4.2 Results of the particle motion polarization analysis

The recorded and reconstructed ground motion and corresponding particle trajectories are presented in Figures 5.17 and 5.18 for sensors 105 and 205, respectively. In both figures, the gray traces represent the ground motion recorded by the sensors, and the black lines represent the reconstructed signal related to the energy transmitted from the vibrating building to the ground (Figure 5.17a and Figure 5.18a). Gray patches indicate three time intervals, P1, P2, and P3, chosen to analyze the particle motion of the reconstructed signal. P1 starts at 20 s, P2 at 35 s, and P3 at 55 s, and each time interval has 5 seconds length. The intervals were chosen to cover the part of the signal a) where most of the recorded signal energy is located (P1), b) where most of the reconstructed signal energy is located (P2), and c) the coda (P3). The color scales at the bottom of the time histories of the signals, from blue to red, correspond to the time increment used for the particle motion visualization. Both the reconstructed signal and the recorded ground motion of the selected time intervals were then decomposed into three planes X-Z (Figure 5.17b-d and Figure 5.18b-d), Y- Z (Figure 5.17e-g and Figure 5.18e-g), and horizontal X-Y (Figure 5.17h-j and Figure 5.18h-j).

For the two horizontal components, the difference in amplitudes is the most significant in P1, where the recorded signal is the strongest. The amplitude differences are highlighted in the decomposed trajectories. Low amplitudes of the Z component result in nearly linear polarization of the motion in the X-Z and Y-Z planes in all presented time intervals. Clear elliptical motion is observed only in the horizontal plane (X-Y). In comparison, the particle trajectory of the recorded signal does not show clear polarization. The results for both sensors (Figures 5.17 and 5.18) are quite similar with a small difference in P1, where elliptical motion in the horizontal plane is more pronounced in the results from sensor 205 (Figure 5.18h).

5.4.3 Discussion

Performing the polarization analysis in two separate parts provides complete information about the polarization of the wavefield transmitted from the building to its surroundings. The polarization ellipse parameters of the deconvolved wavefield give information about the polarization of the wavefield in the surroundings of the analyzed building due to the unit impulse applied at the top of the structure. Therefore they define the polarization of the response of the building-soil system. In the second part, the focus is on the analysis of the polarization of the particle motion of the reconstructed wavefield that corresponds to the transmitted energy only.

In the case of the Matera test site, both parts provided complementary results. The first part of the analysis suggested that the polarization ellipses in the analyzed frequency bands are dominated by linear components, described by the difference between the two axes of the ellipse (Figure 5.16).

In X-Z and Y-Z planes, the particle motion is linearly polarized and the only clear elliptical motion is observed in the horizontal plane (X-Y). According to Richart et al. (1970), the energy transmitted from a circular footing undergoing vertical oscillations is propagated into the ground by the footing as a combination of P, S, and Rayleigh waves. Considering that the particle motion of the Rayleigh waves is a combination of two components - radial and vertical (Richart et al., 1970; Stein and Wysession, 2003), in the case of the Matera test site, the reconstructed motion

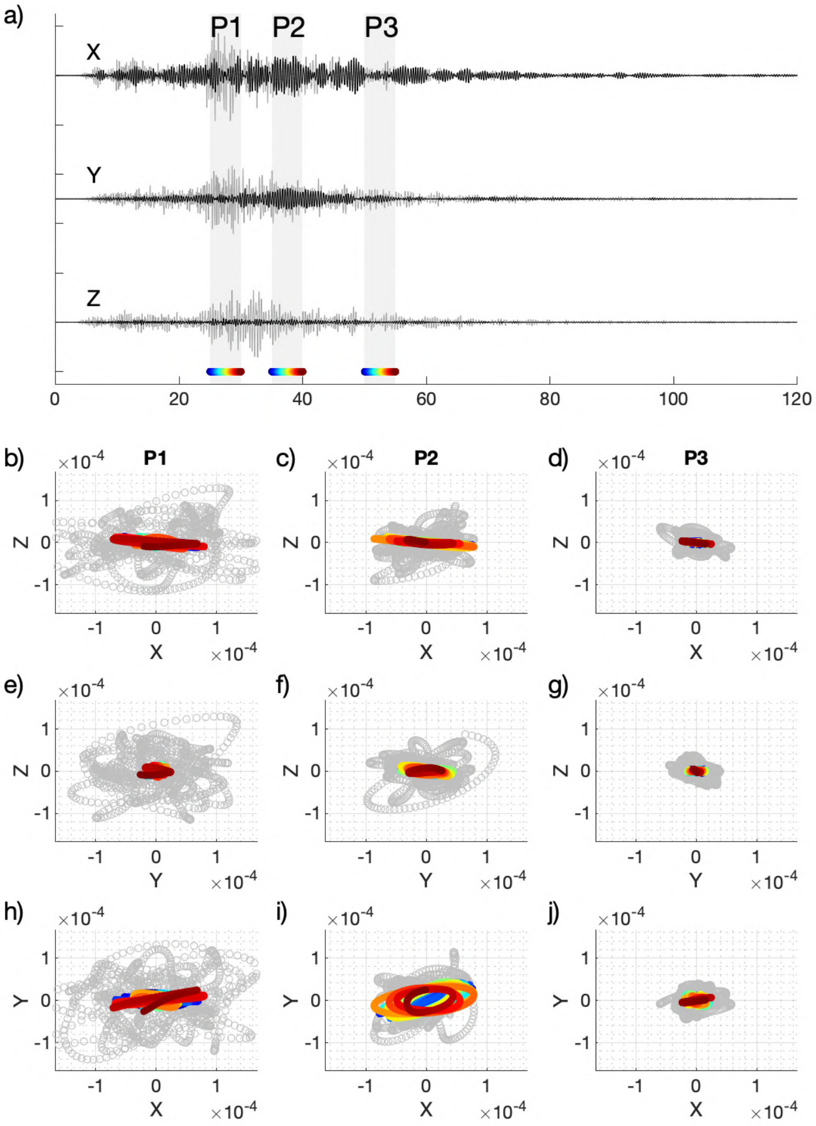

Figure 5.17: Particle motion trajectory analysis for sensor 105 from Array 1. a) Time histories of the recorded signal (gray) and the reconstructed signal radiated from the building to the athletic field (black). Gray shades indicate the intervals (P1, P2, and P3) for the trajectory analysis. b) - j) particle motion in three planes - radial X-Z (b-d), transverse Y-Z (e-g), and horizontal X-Y (h-j). The color scale of the trajectory plots corresponds to the increment of time (from blue to red) indicated at the bottom of the time history plots for each selected time interval. The gray scatter from b) to j) represents the trajectory of the recorded signal (gray traces in a)) for the corresponding time intervals.

is not dominated by a classically polarized Rayleigh wave.

The estimated wave propagation velocities of the deconvolved wavefield features (peaks) related to the energy radiated from the building (Table 5.2) are smaller than v_S of the soil layers of the Matera test site (Table 4.2). Therefore, the strong influence of compressional P-waves, which are faster than S-waves, in the radiated wavefield can be excluded.

One explanation for the observed radiated wavefield polarization results could be

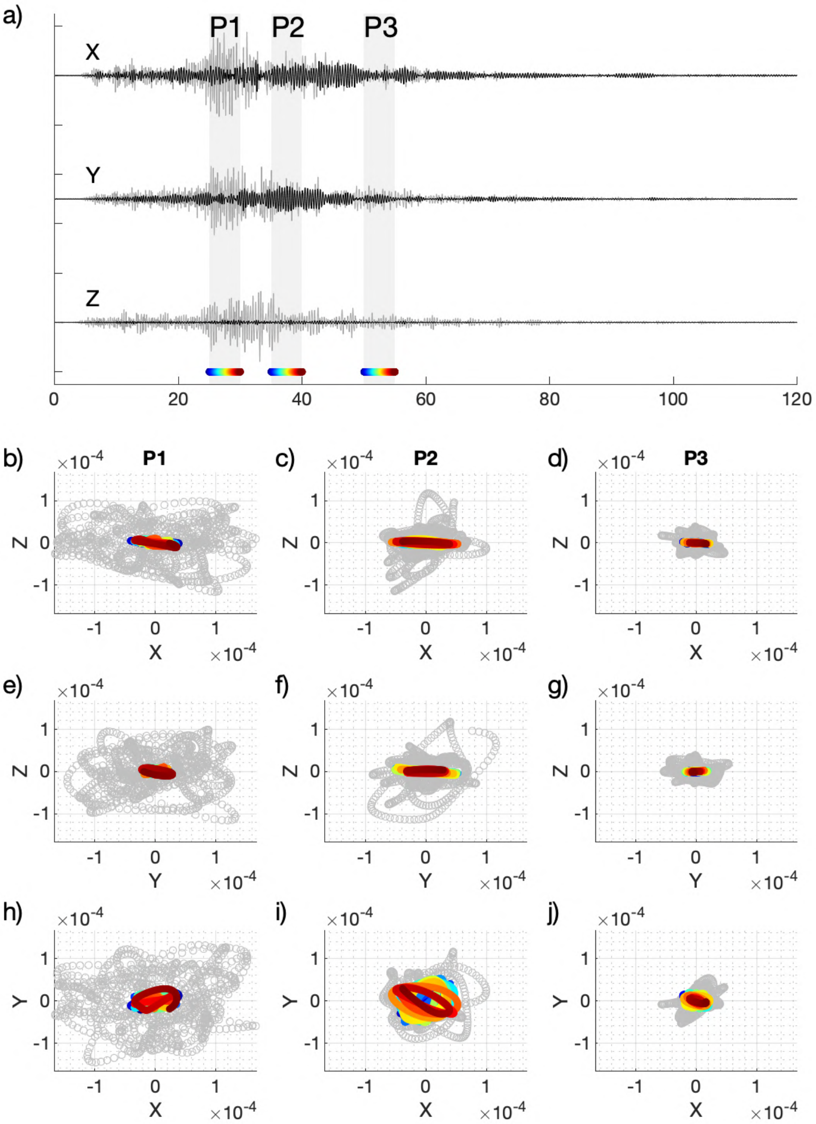

Figure 5.18: Particle motion trajectory analysis for sensor 205 from Array 2. a) Time histories of the recorded signal (gray) and the reconstructed signal radiated from the building to the athletic field (black). Gray shades indicate the intervals (P1, P2, and P3) for the trajectory analysis. b) - j) particle motion in three planes - radial X-Z (b-d), transverse Y-Z (e-g), and horizontal X-Y (h-j). The color scale of the trajectory plots corresponds to the increment of time (from blue to red) indicated at the bottom of the time history plots for each selected time interval. The gray scatter from b) to j) represents the trajectory of the recorded signal (gray traces in a)) for the corresponding time intervals.

that the anisotropy of the test site creates non-classically polarized surface waves. Yanovskaya and Savina (2004) defined quasi-Rayleigh waves by three planes, where radial and transverse have a phase shift, and the particle motion of the horizontal plane is elliptical. Another explanation for the observed polarization could be a combination of quasi-Rayleigh, and quasi-Love waves, which do not have strictly transverse motion according to Tanimoto (2004). Another possible explanation for the observed elliptical particle motion in the horizontal plane could be non-synchronous oscillations of the building in the X and Y direction. However, to fully understand the observed behavior, further study on both the anisotropy of the test site and the behavior of the building should be performed.

The analysis of the trajectory of the particle motion of the reconstructed ground motion related to the energy transmitted from the building to the ground showed that the polarization is stable in time during the event (i.e., it does not depend on the chosen time window, see Appendix A.4). The observed changes in the amplitude with time are related to the decrease of energy with time.

Chapter 6

Results Piana di Toppo

The results obtained by the analyzes presented in this Chapter are similar for both sensor arrays aligned with the main axes of the structure analyzed in this Chapter. Therefore, since the NS array was composed of more sensors installed on the ground (six vs four in the EW array), in the following sections of the thesis I present only the results from the NS array.

6.1 Dynamic behavior of the structure

6.1.1 Spectral ratio results

Similar to the analysis performed using data from the Matera test site, the dynamic behavior of the structure in the Piana di Toppo experiment was estimated using both seismic noise and earthquake recordings. Since all the studied earthquakes were recorded by sensors installed in the S3 setup, noise recordings from the S3 setup were used for the spectral ratio analysis. A comparison of the average spectral ratios of 20 s long moving windows of seismic noise recordings from the 21st of April 2022 between 06:00 pm and 10:00 pm and the spectral ratios of all analyzed earthquakes are presented in Figure 6.1 for the three components. The accuracy of the measurements of the spectral peaks is ± 0.05 Hz.

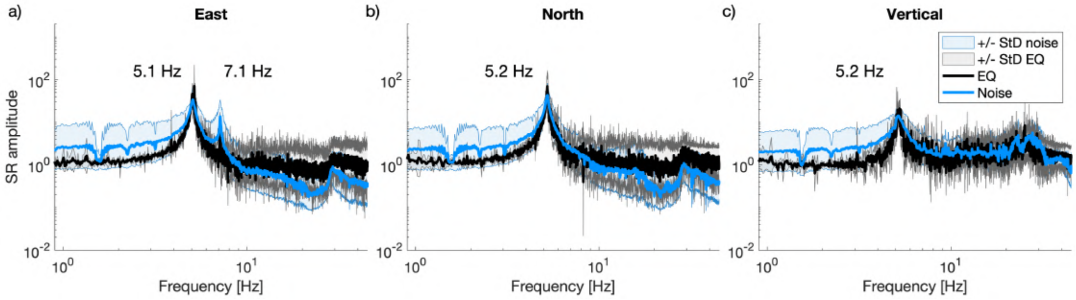

Figure 6.1: Comparison of average spectral ratios between sensors $921C_E$ (top) and $931C_E$ (bottom) for 20 s long moving windows from four hour-long noise (blue) recordings and all selected earthquake data (black) for each component.

The fundamental frequency of the structure estimated from the seismic noise recordings is around 5.1 Hz for the East component, and 5.2 Hz for the North component. In the vertical component, the spectral ratio peak is also present at 5.2

Hz, the same frequency as the North component. The second peak, at 7.1 Hz, is visible only in the East component.

The average earthquake spectral ratios show peaks at the same frequencies as the seismic noise. In the East direction, the peak at 5.1 Hz is amplified two times compared to the peak from the noise recordings. This is, however, not the case for the second peak at 7.1 Hz, where the noise spectral ratio is amplified by almost three times compared to the earthquake recordings. As for the East component, in the North component the earthquake peak is at the same frequency as noise (5.2 Hz) and is almost two times more amplified compared to the noise results. The vertical component spectral ratio of the earthquake data has a peak at 5.2 Hz and it has a slightly higher amplitude than the noise peak at the same frequency.

6.1.2 Frequency Domain Decomposition results

Since the S2 setup aimed to precisely characterize the dynamic behavior of the structure, in addition to the spectral ratio estimations, seismic noise data recorded on the 7th of April 2022 between 10:30 pm and midnight (1,5 h) was used for the FDD analysis. The normalized singular values of the PSD matrix are presented in Figure 6.2. The three first eigenvectors are highlighted with thick black lines for better visualization of the main peaks.

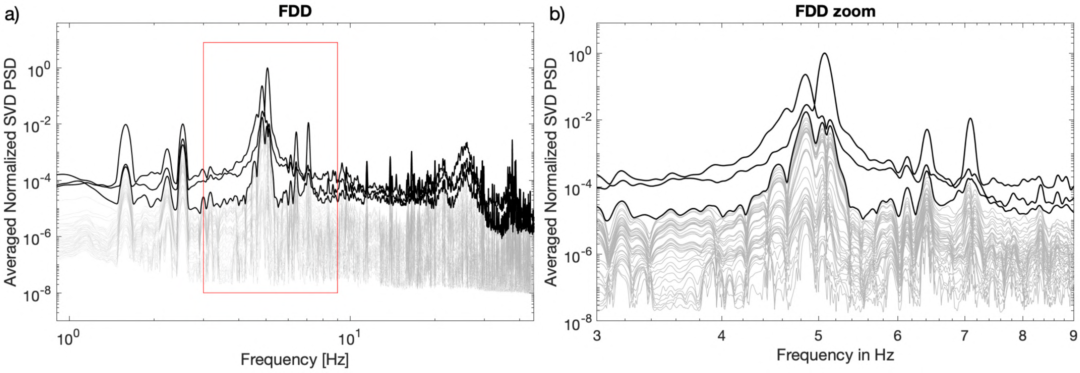

Figure 6.2: The singular values of the PSD matrix from the seismic noise FDD analysis of the Piana di Toppo structure. The first three eigenvectors from each setup are plotted in black, the rest in gray.

The singular values of the PSD matrix show multiple peaks over a wide range of frequencies. The first three peaks identified by the FDD analysis are at 1.6 Hz, 2.2 Hz, and 2.5 Hz. By comparing with the spectral ratio results, they are at the same frequencies as the troughs visible in the noise spectral ratio (Figure 6.1).

Since the spectral ratios of both noise and earthquake data show peaks between 3 Hz and 10 Hz, the focus on the analysis of the singular values of the PSD matrix is in this frequency range (Figure 6.2b). There are four peaks at 4.8 Hz, 5.1 Hz, 6.4 Hz, and 7.1 Hz. Similar to the peaks below 3 Hz, the peak at 6.4 Hz is also not present in any of the spectral ratio results. The estimated mode shapes for the three frequencies identified by both spectral ratio and FDD analyses (4.8 Hz, 5.1 Hz, and 7.1 Hz) are presented in Figure 6.3. The first two modes, at 4.8 Hz (Figure 6.3a, d) and at 5.1 Hz (Figure 6.3b, e), are the close bending modes in orthogonal directions (East and North, respectively). The third mode at 7.1 Hz (Figure 6.3c, f) is a torsional mode.

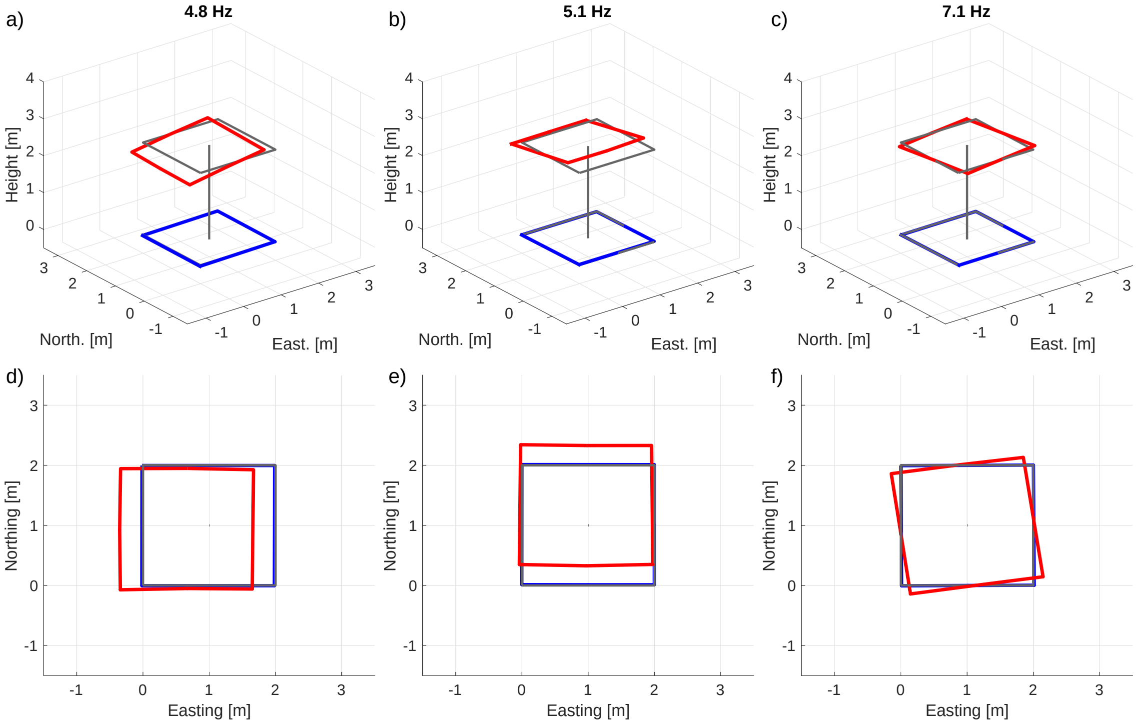

Figure 6.3: Estimated mode shapes for the three modes identified by FDD analyses at 4.8 Hz - bending in the East direction, 5.1 Hz - bending in the North direction, 7.1 Hz - torsion. Red lines indicate the position of the top slab of the structure. Blue lines indicate the position of the bottom slab. a)-c) show perspective view. d)-f) show the view from the top.

6.1.3 Discussion

The estimated resonant frequencies from the noise and earthquake spectral ratios are very close for both horizontal components because the structure is symmetric. The small frequency differences between the components could be caused by the uneven distribution of the construction material (concrete) in the slabs, which could change the center of gravity of the structure and thus cause changes in the stiffness in both directions.

More complex FFD results around 5 Hz (i.e. double peak, Figure 6.2) compared to the spectral ratio results is caused by the fact that the spectral ratio analysis is done separately for each component, whereas in FDD analysis all components are considered together. Since the dominant frequencies for each horizontal components are close, this is visible in the FDD results as a double peak around 5 Hz.

The troughs at 1.6 Hz, 2.2 Hz, and 2.5 Hz observed in the spectral ratios (Figure 6.1) correspond to the peaks in the FDD results (Figure 6.2). To understand why the troughs in the spectral ratio are at the same frequencies as the peaks in the FDD analysis, a cross-comparison was made with the averaged moving window FFT of the noise recordings from all sensors in all experimental setups (Figure 6.4). The FFT comparison showed that peaks below 3 Hz are also present in the Fourier amplitude spectra of the S1 setup. Peaks at 2.2 Hz and 2.5 Hz are present in all Fourier amplitude spectra of all three components from all three setups. The peak at 1.6 Hz is only visible in the FFTs of the horizontal components of the S1 and S2 setups. The presence of the peaks prior to the installation of the structure indicates that they are unrelated to the structure and originate from another source, which is not defined in this study.

The peak at 6.4 Hz is also present in the Fourier amplitude spectra from the S1 setup and is not visible in any of the spectral ratio results (similar to the peaks below 3 Hz), therefore is not structure-related. The other three peaks in the frequency range of 3 Hz to 10 Hz (4.8 Hz, 5.1 Hz, and 7.1 Hz) correspond to the modes of the structure (Figure 6.3).

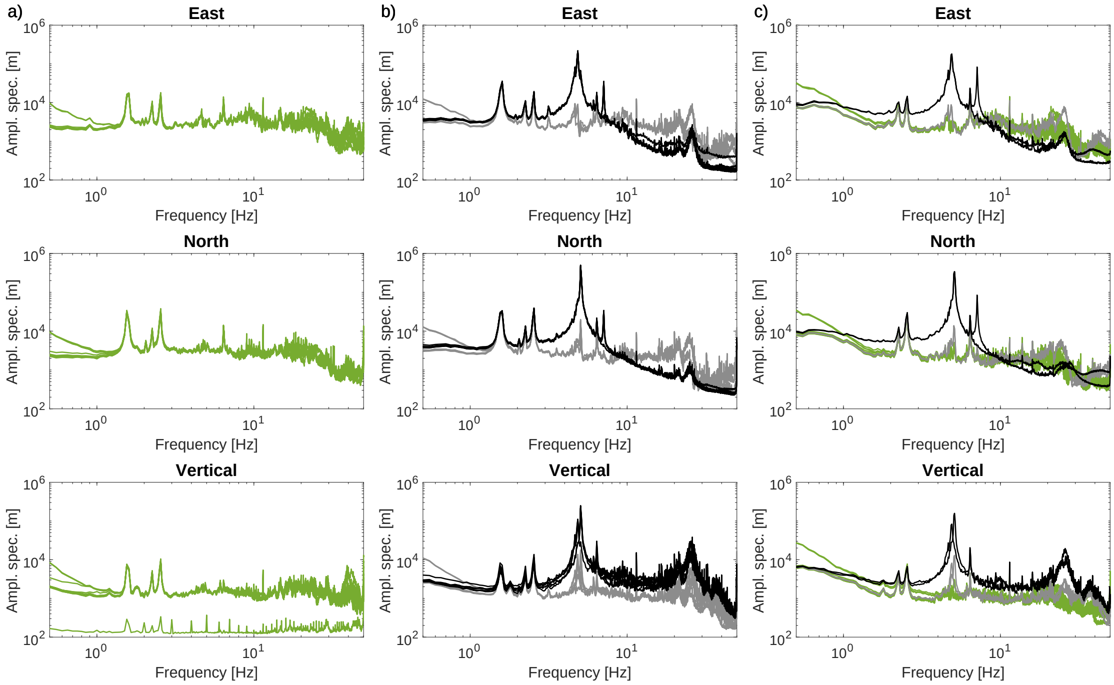

Figure 6.4: Fourier amplitude spectra of all sensors installed in a) the S1 setup, b) the S2 setup, and c) the S3 setup. Green lines correspond to the sensors installed on the ground, gray lines to those installed on the bottom slab of the structure, and black lines to those installed on the top of the structure.

The analysis of the dynamic behavior of the structure in the Piana di Toppo experiment using the spectral ratio method showed that most of the vibrational energy of the structure is located between 3 Hz and 10 Hz. The results coming from spectral ratio, FDD, and FFT analyses provided very similar results and identified three modes of the structure: the two bending modes and one torsional.

Since the top sensor used for the spectral ratio calculation (921_{E}) was located in the middle of the southern edge of the top and bottom slab, the torsional mode at 7.1 Hz is only present in the East component (Figure 6.1a). A different sensor position, such as in the corner of the slab (Figure 6.5) would show the torsional mode in both horizontal components after spectral ratio analysis (in the case of rotation with respect to the vertical axis of the structure).

The difference in the amplitude of the peaks observed in spectral ratios coming from seismic noise and earthquake data might be caused by the excitation of different

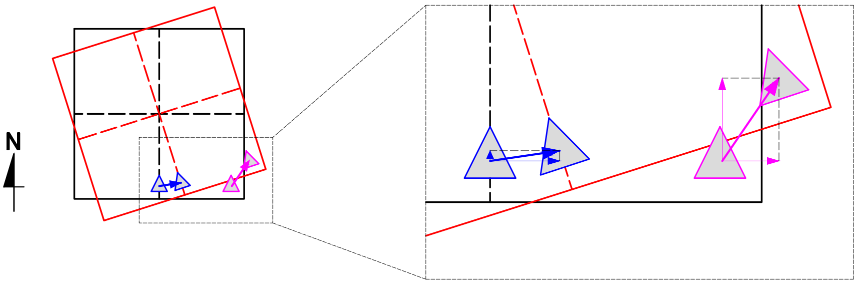

Figure 6.5: Displacement at the top of the structure due to the torsional mode at 7.1 Hz. Black lines show the undeformed shape of the top slab. With the red lines is presented the displacement of the top slab due to torsion. The blue triangles indicate the positions of sensor 921_{E} in the southern part of the top slab. The pink triangle indicates the informative position of the sensor if installed in the corner of the slab (not installed during the S3 setup). Arrows indicate the displacement of the sensor. On the right, zoom in on the corner indicated by the dashed rectangle. Small arrows indicate the decomposition of the displacement vectors in the North-South direction (vertical) and East-West direction (horizontal).

modes by different frequency content of the inputs. The results indicate that, unlike the seismic noise, the recorded earthquakes did not strongly activate the torsional mode at 7.1 Hz. The earthquake input did, however, activate the bending mode of the analyzed structure more strongly.

Since the structure was numerically modeled in SAP2000 (courtesy of Chiara Amendola), it was possible to compare the frequencies and modal shapes estimated from the real data results and from the numerical model. The four modes, two at 5.0 Hz, at 5.9 Hz, and at 23.0 Hz, estimated from the model are presented in Figure 6.6.

The real data modes are comparable to the numerical model from SAP2000, however, there are some slight differences in the estimated resonant frequencies. Since the structure is symmetric, the first two bending modes of the model are at the same frequency of 5.0 Hz. In reality, the resonant frequencies for East and North directions differ from each other and from the estimates made by the numerical model (Figure 6.3).

A similar observation can be made for the third torsional mode, which in the model is at 5.9 Hz, whereas in the results from spectral ratios and FDD analysis is at 7.1 Hz. The differences between the model and the real data are most likely because the structure, in reality, is stiffer in the North direction than the calculated fixed-base numerical model.

The second bending mode estimated by the model at 23.0 Hz is not observed in the spectral ratio results of the horizontal components. A small amplification effect, however, is present in the spectral ratio of the vertical component and in the FFD results around 26.0 Hz.

The different instrumental setups during the experiment, the recording being long enough to record a sequence of earthquakes, and the availability of the numerical model, made it possible to study in detail the dynamic behavior of the built structure. Even though there are some differences observed between the numerical

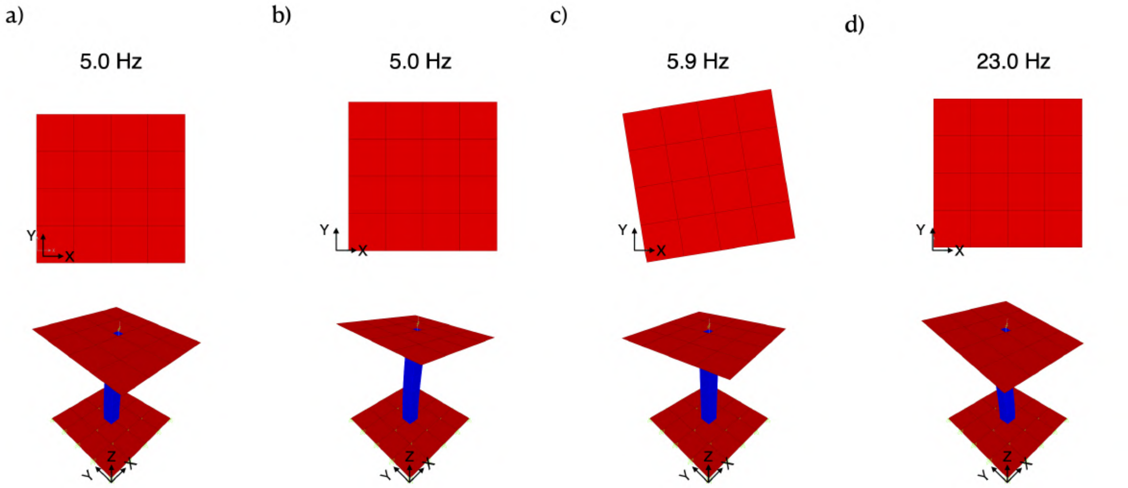

Figure 6.6: Mode shapes SAP2000 estimated for the first bending mode at 5.0 Hz (a,b), the torsional mode at 5.9 Hz (c), and the second bending mode at 23.0 Hz. The top row shows the displacement of the top slab in the X-Y plane for each frequency. The bottom row shows the 3D view of the deformation of the structure corresponding to the defined mode. Courtesy of Chiara Amendola.

model and spectral ratios and FDD analyses of the real data, they provided complimentary information on the frequency band needed for further analysis. The results coming from all the presented analyses indicate that most of the vibrational energy of the structure is located in the frequency band between 3 Hz and 10 Hz. Therefore to focus the study on the frequency range where possible interaction between the structure and the soil might occur, data were filtered between those frequencies.

6.2 Deconvolution of the recordings installed on the structure and the soil

6.2.1 Results

The earthquake data was filtered with a 4-th order Butterworth filter between 3 Hz and 10 Hz and deconvolved using sensor 921D$_{\mathrm{E}}$ at the top of the structure as a reference. The deconvolved wavefields from the NS array are presented in Figure 6.7 for the small earthquake recorded around 18 km from the test site, and in Figure 6.8 for all the five earthquakes from the Bosnia sequence. Since sensors 931D$_{\mathrm{E}}$, 921D$_{\mathrm{E}}$ and A928$_{\mathrm{E}}$ did not record earthquakes from the Bosnia sequence, they are not shown in Figure 6.8. The gray dashed vertical line indicates time 0 and the red dashed line indicates the time of the acausal peak of the sensor at the bottom of the structure with respect to time 0. Sensor 931C$_{\mathrm{H}}$ was not directly installed on the structure, but on the ground around 5 cm from the edge of the foundation, however, due to the closeness of the sensor 931C$_{\mathrm{E}}$, it also has a gray background.

The recordings of the close and small earthquake had higher energy in the higher frequencies (above 1 Hz), whereas the considered events of the Bosnia sequence amplified the lower frequencies (around 1 Hz). Since the energy content of the

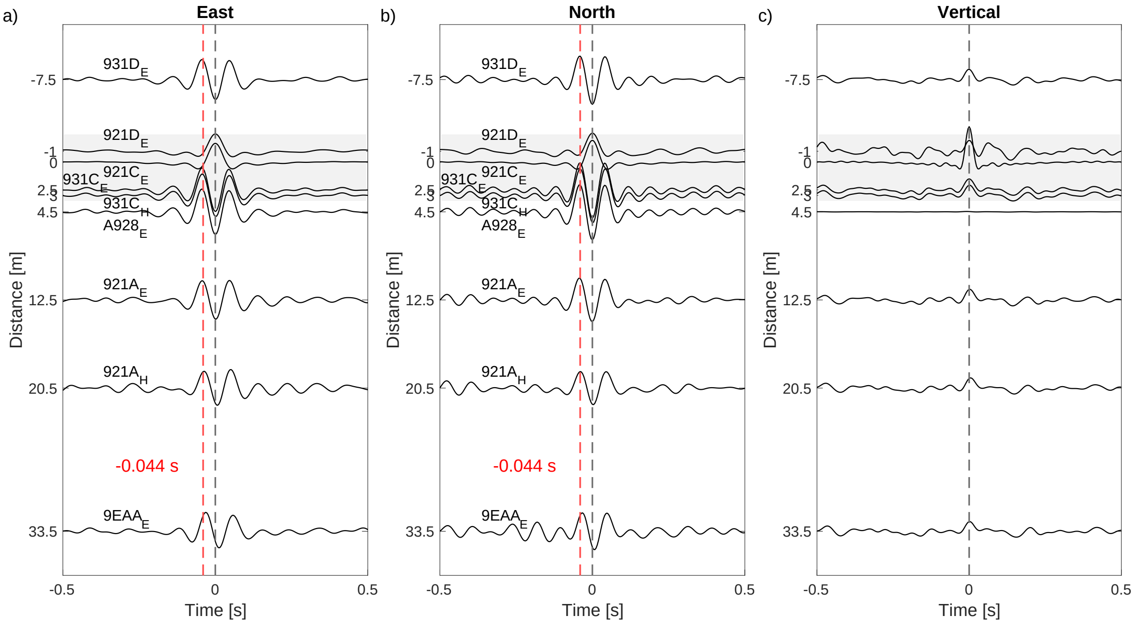

Figure 6.7: Deconvolved wavefield of the small earthquake recordings from the North-South array filtered between 3 Hz and 10 Hz for a) X, b) Y, and c) Z components. The deconvolved wavefield was obtained using a sensor at the top of the structure (921D$_\mathrm{E}$) as a reference. The y-axis indicates the distance from the position of the reference sensor accounting for both vertical and horizontal offset. The negative distance indicates the position North of the reference sensor. The time delays of the acausal peaks of the sensor installed at the bottom of the structure are indicated with red dashed vertical lines with corresponding values in a) and b). In c) the wave propagation velocity is too high to observe peak separation. The gray background indicates sensors 921D$_\mathrm{E}$, 931C$_\mathrm{E}$, and 921C$_\mathrm{E}$ installed on the structure.

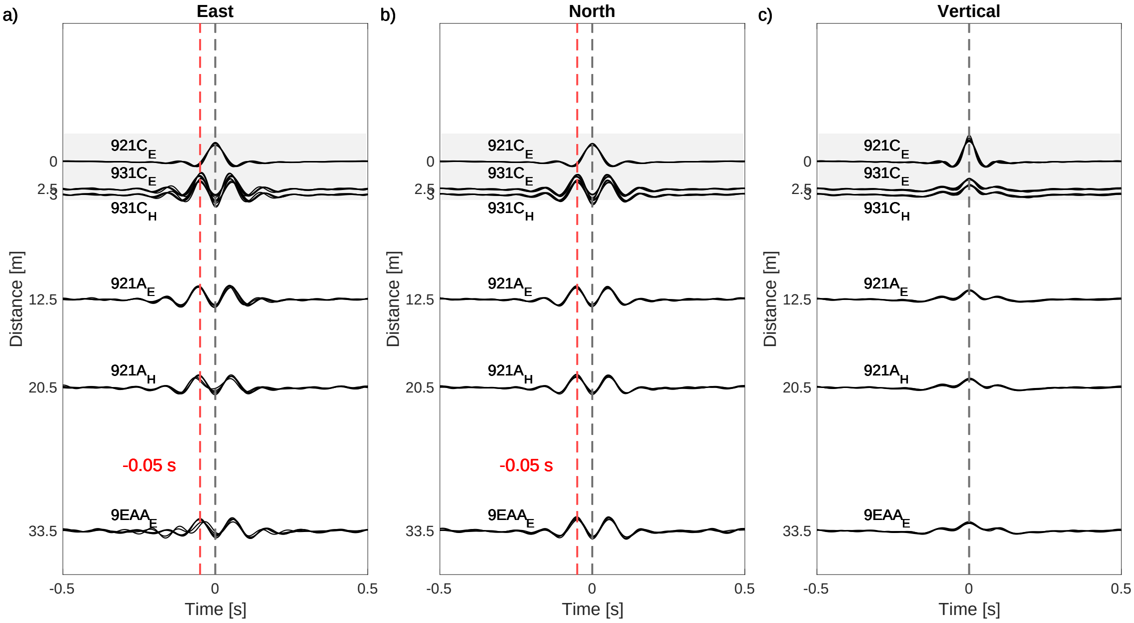

Figure 6.8: Same as Figure 6.7 but for all considered earthquakes from the Bosnia sequence.

input was different for two groups (the small earthquake and the Bosnia sequence), I analyze them separately.

The difference in energy content is also visible in the deconvolution results, where in the small earthquake deconvolution (Figure 6.7), the higher frequencies are amplified compared to the Bosnia sequence (Figure 6.8). However, both groups have similar shapes in terms of the main acausal and causal peaks of the sensors installed on the ground and foundation of the structure. The main peaks in acausal and causal parts of the deconvolved wavefields of the two horizontal components are symmetric.

The deconvolved wavefields of the earthquake that occurred 18 km away from the test site (Figure 6.7) show that the time delay corresponding to the main acausal peak is almost the same within the uncertainty of measurements for all the sensors installed on the ground and for the sensor installed at the bottom slab. The delay is around 0.044 s (± 0.002 s) for both horizontal components. With a structure represented by an equivalent block (considering the appropriate percentage of the construction material and empty spaces), the time delay of the phases of the deconvolved wavefields can be related to the wave propagation velocity in the medium. Based on the relation of the travel time and distance, the wave propagation velocity in the equivalent medium during the first earthquake was around 57 m/s (± 3 m/s).

The deconvolved wavefields of the five earthquakes from the Bosnia sequence are very similar, with some minor variations in the East component of sensor $9\mathrm{EAA}_\mathrm{E}$ (Figure 6.8). The time delay of the acausal peak of the sensors installed on the ground and the bottom slab of the structure is almost the same for all of the Bosnia earthquakes and is around 0.050 s (± 0.003 s). In the equivalent medium representing the structure the wave propagation velocity is therefore around 50 m/s (± 3 m/s).

The separation of the peaks in the deconvolved wavefields of the vertical component is not visible for all of the analyzed earthquakes. In contrast to the results from the earthquakes from the Bosnia sequence (Figure 6.8c), the deconvolved wavefield of the small earthquake (Figure 6.7c) is much noisier in the vertical component and the main peak at time 0 is not as clear as for the other earthquakes.

6.2.2 Discussion

The occurrence at the same time of the main peak in the acausal part of the deconvolved wavefields of the horizontal components, for all the sensors installed on the ground, confirms that the input can be approximated as a vertically propagating plane wave. Such behavior is caused by the earthquake energy reaching all the mentioned sensors at the same time. Additionally, due to the very small elevation difference between the ground sensors and the sensors installed at the bottom slab of the structure (approximately 0.4 m), the time delay of the acausal peak is the same for all of them.

The slower wave propagation velocity, indicated by the observed time delay difference of the main acausal peak (Figures 6.7 and 6.8) could be explained by the larger loading from the Bosnia sequence earthquakes. A similar phenomenon has been observed previously also for small loadings in real buildings (e.g. Astorga et al., 2018; Skłodowska et al., 2021; Jaimes et al., 2022). Even though the observed difference in the time domain is small, it has an impact on the velocity results. However, considering the dimensions of the structure and the sampling resolution of the results, the estimate of the wave propagation velocity in the case of the Piana di Toppo experiment should be considered only informative.

Due to the stronger influence of higher frequencies on the deconvolved wavefields of the close earthquake, the obtained wavefields are more complex (i.e., there are more peaks) than those obtained from the five earthquakes from the Bosnia sequence. This difference in energy of different frequencies is also visible in the Fourier amplitude spectra of small earthquakes and in the mainshock of the Bosnia sequence (seen in the comparison of the spectra of their deconvolved wavefields presented in Figure 6.9). This observation could be caused by a combination of higher attenuation of the short-period waves than long-period ones with distance, and the different energy content released by earthquakes of different magnitudes (Stein and Wysession, 2003; Aki and Richards, 1981).

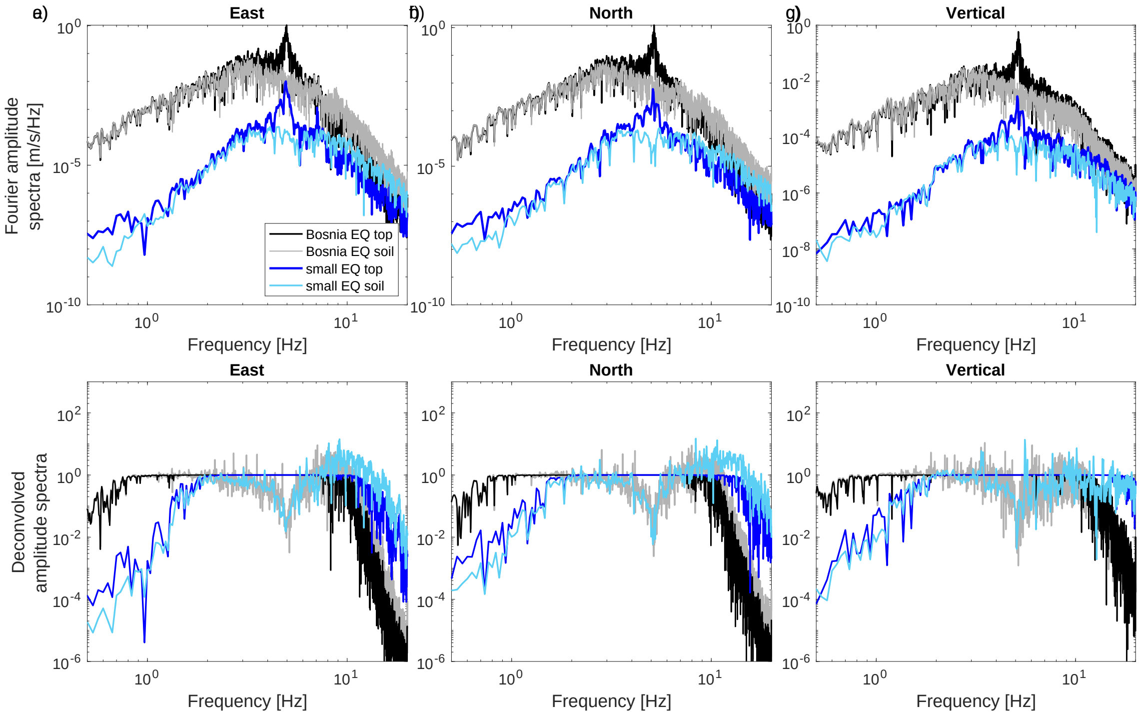

Figure 6.9: Comparison of the Fourier amplitude spectra (a-c) and the deconvolved amplitude spectra (d-f) of the A.8 earthquake from the Bosnia sequence and the small earthquake (B.1). The recording at the top of the structure for the Bosnia earthquake is indicated with black line, and for the bottom of the structure with a gray line. For the small earthquake, the top recording is indicated with a dark blue line and the bottom one with a light blue line.

6.3 Seismic phase identification

6.3.1 Analytical model

Similarly to the Matera case, to identify the peaks of the deconvolved wavefield related to the energy transmitted from the structure to its surroundings, the analytical model is introduced in the following section. The analytical model developed for the Piana di Toppo case study describes the transfer function between the sensors in the field and the sensor installed on the top slab of the structure. The simplified geometry used for the model is presented in Figure 6.10.

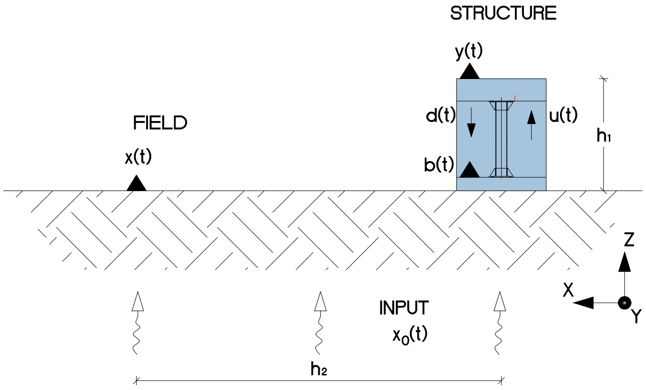

Figure 6.10: Schematic geometry of the Piana di Toppo test site used for the analytical model. The structure is indicated by the blue rectangle on the right. h_1 is the height of the structure, and h_2 is the horizontal distance of a sensor in the field from the sensor installed at the bottom of the building. $x(t)$ defines the recordings of the sensors installed on the ground, and $y(t)$ and $b(t)$ are the recordings at the top and bottom of the structure, respectively. $u(t)$ and $d(t)$ are the up- and down-going waves in the building. $x_0(t)$ is the input ground motion.

Since the results from the deconvolution show that the input, $x_0(t)$, can be approximated by the vertically propagating plane wave (simultaneous arrival of the peaks in the acausal part of the deconvolved wavefields, Figures 6.7 and 6.8), such assumption is made for the model development. Therefore, analogously to the model developed for the Matera test case, the up- , $u(t)$, and down-going waves in the structure, $d(t)$, can be defined as

$$u(t) = b(t - \tau_1) + (-r)d(t - \tau_1)) \tag{6.1}$$

and

$$d(t) = u(t - \tau_1) \tag{6.2}$$

where τ_1 is the wave propagation travel time in the structure with velocity V_1 and r is the reflection coefficient (Equation 2.3). $b(t)$ is the recording at the bottom of the structure defined as

$$b(t) = x_0(t)(1 + r). \tag{6.3}$$

$(1+r)$ is the transmission coefficient of the soil-structure boundary (see Section 2.1).

The free surface condition at the top of the structure considers the structure modeled as a layer over a soil layer, and therefore, the signal at the top is defined as

$$y(t) = 2u(t). \tag{6.4}$$

The recordings at the position of the sensors installed on the ground are defined by

$$x(t) = 2x_0(t) + (1 - r)d(t - \tau_2) \tag{6.5}$$

where τ_2 is the travel time corresponding to the wave propagating from the structure to its surroundings with velocity V_2.

Analogous to the development of the analytical model used for the Matera data analysis (see Section 5.3.1), Fourier transforms and simplification of Equations 6.1, 6.2, 6.3, 6.4 and 6.5 were performed. Finally, the model of the transfer function of the building-soil system using the recording at the top of the structure as a reference used for the Piana di Toppo seismic phase identification is defined as

$$\frac{X(f)}{Y(f)} = R_1 + R_2 + R_3 \tag{6.6}$$

where

$$R_1 = \frac{1}{1+r} e^{-i2\pi f(-\tau_1)}, \tag{6.7}$$

$$R_2 = \frac{r}{1+r} e^{-i2\pi f(\tau_1)}, \tag{6.8}$$

and

$$R_3 = \frac{(1-r)}{2} e^{-i2\pi f(\tau_1+\tau_2)}. \tag{6.9}$$

where $X(f)$ and $Y(f)$ are the Fourier transforms of the signal $x(t)$ recorded on the ground, and the signal $y(t)$ recorded on the top of the structure, respectively. The density of the layer representing the structure was estimated equal to $\rho_{structure} =$ 350 kg/m3, taking into consideration the densities of the materials that compose the structure (top and bottom slabs and steel column) and their respective contributions to the exterior volume (2.0 m x 2.0 m x 2.5 m). The density of the soil was estimated to be equal to $\rho_{soil} = 1800$ kg/m3 (Table 2.11 p. 32, Lanzo and Silvestri, 2016).

6.3.2 Results - analytical model fit

First, to estimate the wave propagation velocity in the medium representing the structure, I use the model proposed by Snieder and Şafak (2006), defined by Equation 5.14. The time delays τ_1 used for the calculations are indicated in Figures 6.7 and 6.8 with red text. The wave propagation velocities in the structure (Table 6.1) were obtained by performing a two-step grid search in the frequency domain:

1. estimation of the wave propagation velocity in the medium representing the structure based on the time delay τ_1 using Model 5.14 (Figures 6.11a,c and 6.12a,c),

2. estimation of the τ_2 defining velocity of the wave propagation in the soil (V_2, using Model 6.6 and previously estimated τ_1 (Figures 6.11b,d and 6.12b,d).

The grid search was performed for each one of the earthquakes separately. Figures 6.11 and 6.12 show the example grid search results of the parameters describing the best-fitting model for the small earthquake (B.1) and on the Bosnia sequence earthquakes (A.8). The grid search results for the rest of the Bosnia earthquakes are in the Appendix A.5.

The time delay parameters τ_1 and τ_2 defining best-fitting models were chosen based on the minimum $RMSLE$ (Equation 3.5). The corresponding velocities calculated from the relation of the calculated time delays and the distance of the sensor are presented in Table 6.1.

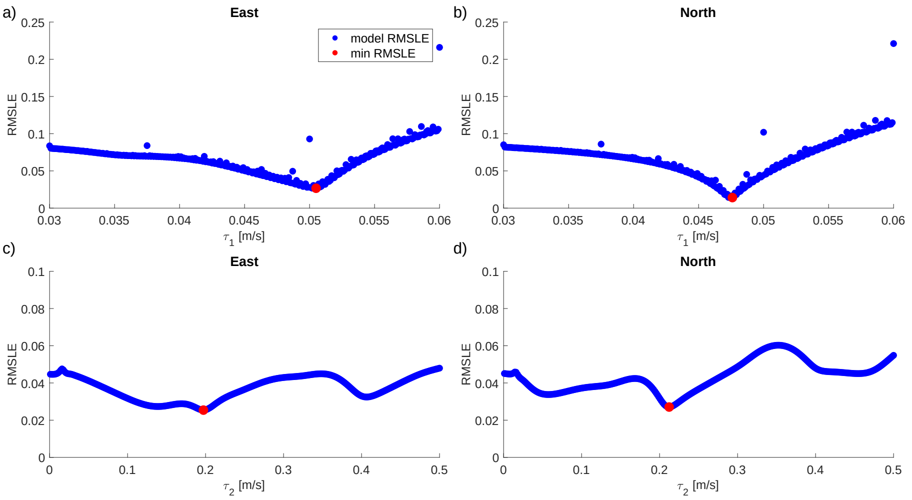

Figure 6.11: The grid search results for the East (a,c) and North components (b,d) of sensor 9EAA$_E$ for the small earthquake (B.1). a) and b) show grid search of τ_1 from fitting Model 5.14. c) and d) show grid search of τ_2 from fitting Model 6.6. The τ_1 and τ_2 values providing minimum $RMSLE$ are indicated with red dots.

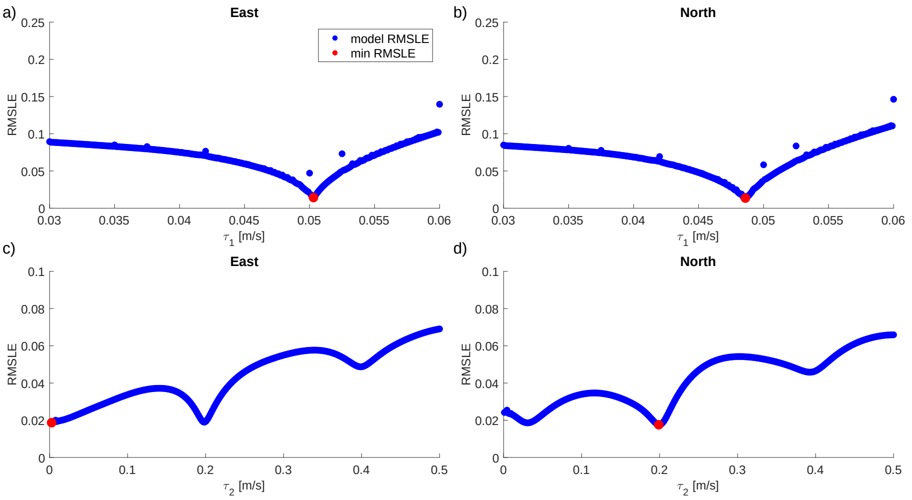

Figure 6.12: The grid search results for the East (a,c) and North components (b,d) of sensor 9EAA$_E$ for one of the Bosnia sequence earthquakes (A.8). a) and b) show grid search of τ_1 from fitting Model 5.14. c) and d) show grid search of τ_2 from fitting Model 6.6. The τ_1 and τ_2 values providing minimum $RMSLE$ are indicated with red dots.

Table 6.1: Wave propagation velocities in the structure and the soil calculated using time delay values providing minimum $RMSLE$ of the analytical model used for the Piana di Toppo data analysis. The information about the chosen earthquakes can be found in Tables A.1 and A.2. Velocities are given in [m/s].

	Component	EQ B.2	EQ A.8	EQ A.9	EQ A.10	EQ A.11	EQ A.12
Structure	East	50 ± 4	50 ± 4	51 ± 4	50 ±4	51 ±4	51 ±4
	North	53 ± 4	51 ± 4	52 ± 4	52 ±4	52 ± 4	52 ± 4
Soil	East	170 ± 1	12578 ± 7829	680 ± 23	932 ± 43	550 ± 15	978 ± 53
	North	158 ± 2	168 ± 1	1144 ± 65	891 ± 39	730 ± 26	757 ± 33

The velocities of the wave propagation in the structure are similar for both horizontal components (51 m/s ± 4 m/s for the East and 52 m/s ± 4 m/s for the North direction). The wave propagation in the structure estimated by the model is the same for both directions, within the range of the uncertainties. The velocity results of the wave propagation in the soil are inconsistent and vary significantly, from 158 m/s ± 2 m/s for the North component of the small earthquake, to unrealistic velocities for some of the Bosnia sequence earthquakes (e.g., 12578 m/s ± 7829 m/s for the East component of the A.8 earthquake). In most of the model fit attempts, the third peak (corresponding to the energy transmitted from the structure to its surroundings) gave a wave propagation velocity that was too high to clearly separate the peaks in the time domain of the deconvolved wavefield.

6.3.3 Discussion

The wave propagation velocities through the structure, calculated from the best-fitting models, are in agreement with the velocities obtained from the time lags of the deconvolved wavefields (within the estimated error range, see Section 6.2). For the first earthquake the velocity difference between the two methods is largest in the East component, however, the velocities are still comparable, and results from both methods are complementary.

The grid search of the time delay corresponding to the wave propagation in the soil did not provide consistent results for the considered events in the two horizontal components. With high wave propagation velocities estimated from the Bosnia sequence earthquake data, separation of the peaks from the first causal peak of the deconvolved wavefield (corresponding to Equation 6.8) was not possible. Additionally, comparing the results with the soil profile of the Piana di Toppo test site, the calculated wave propagation velocities are much higher than the v_S of the top soil layers, which was approximately 551 m/s (Table 4.4). Those results suggest that the model used for the Piana di Toppo results does not properly describe the test site.

To check if the transmitted wavefield can be observed in the deconvolved wavefield results, the same array of the recordings was deconvolved using a sensor installed on the bottom slab, $931\mathrm{C_E}$, as the reference. The results of this analysis are presented in Figure 6.13 for the small earthquake and in Figure 6.14 for all recorded earthquakes for the Bosnia sequence.

The results of the deconvolution using the bottom sensor as the reference show that the input is indeed the vertically propagating wave because the main peaks of the sensors installed on the field and the bottom of the structure all arrive near time 0. The sensors at the top of the structure ($921\mathrm{C_E}$ and $921\mathrm{D_E}$) show an increase in oscillation amplitude in the causal part of the deconvolved wavefield for both horizontal components (Figures 6.13a,b and 6.14a,b).

The oscillation of the structure due to the earthquake input is visible in the causal part of the deconvolved wavefields of the two horizontal components (Figures 6.7a,b and 6.8a,b). The peak of the oscillation is delayed with respect to time 0 by the time necessary for wave propagation through the structure. The vertical component is noisier for the one small earthquake (Figure 6.13c), but for the Bosnia sequence, the deconvolved wavefields are consistent for all five earthquakes (Figure 6.14c).

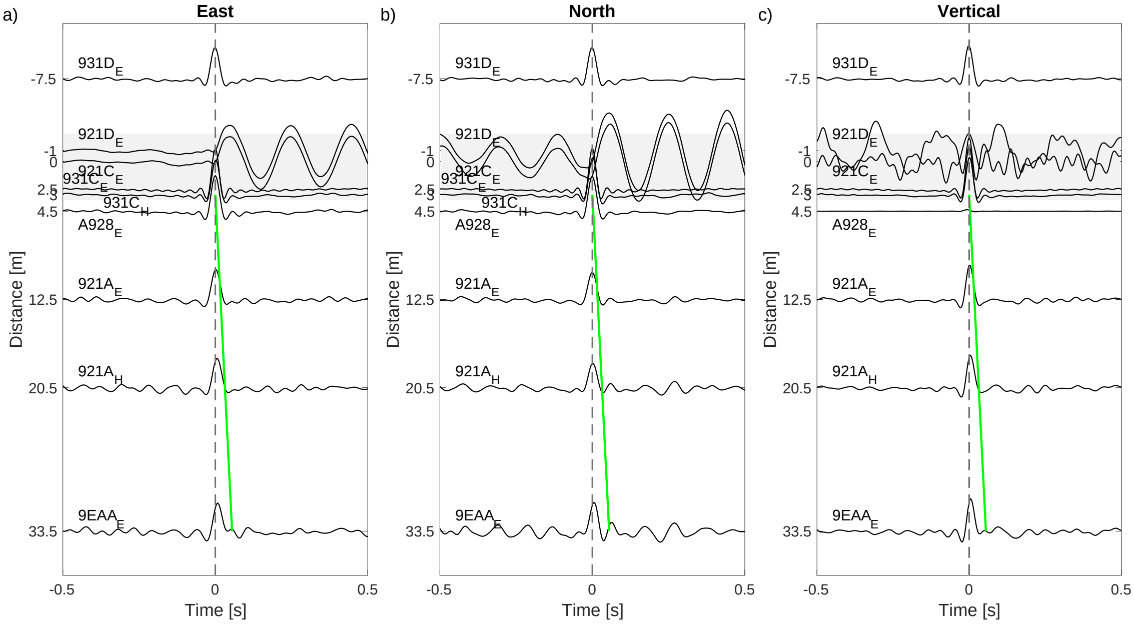

Figure 6.13: Deconvolution of the small earthquake recordings from the North-South array filtered between 3 Hz and 10 Hz for a) X, b) Y, and c) Z components. Results represent the deconvolved wavefield using the sensor at the bottom slab of the structure ($931C_E$) as a reference. The y-axis represents a distance from the position of the sensor at the top of the structure ($921D_E$) considering both vertical and horizontal offset. The distance below 0 indicates the position North of the top sensor. The gray background indicates sensors installed on the structure. Green lines indicate the slope corresponding to the wave propagation with the shear wave velocity of the upper soil layer, $v_s = 550$ m/s.

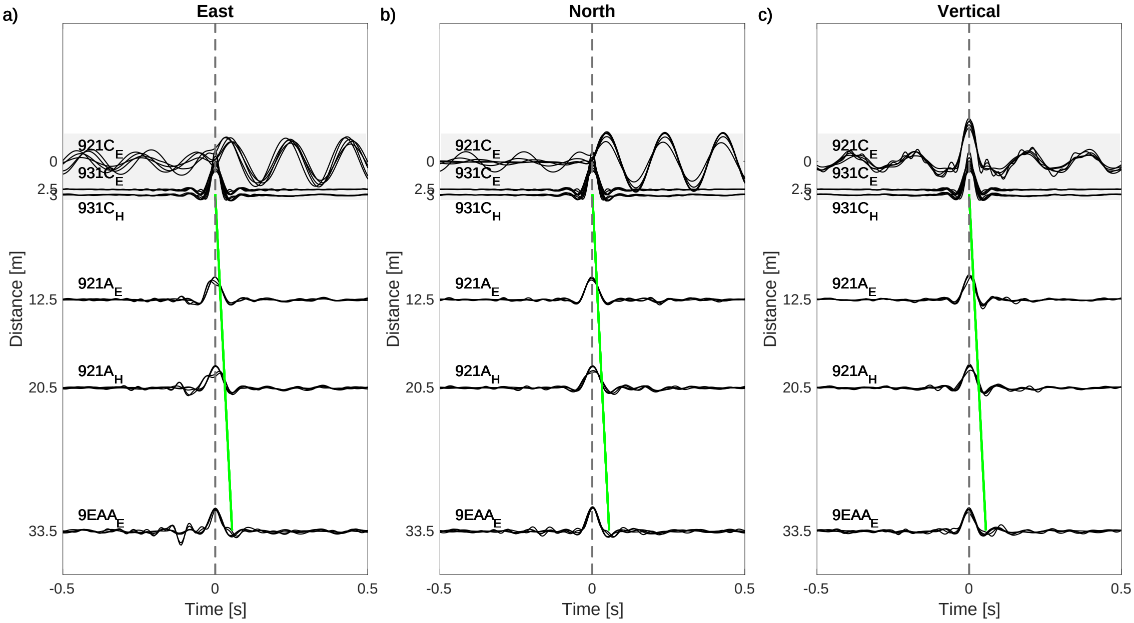

Figure 6.14: Same as Figure 6.7 but for all earthquakes from the Bosnia sequence.

Another important fact, highlighted by the deconvolution using the sensor installed at the bottom of the structure as a reference, is that there is almost no apparent disturbance of the wavefield (i.e., clear peaks) in the deconvolved wavefield that relates to the energy transmitted to the sensors installed on the ground. The slope corresponding to the wave propagation with the velocity of the shear wave velocity in the upper soil layer, $v_S = 551$ m/s (see Table 4.4), was shown in Figures 6.13 and 6.14 to help identification of the seismic phases with similar velocity. However, the only peak which could be identified in such a way is visible in the North component of the deconvolved wavefield from the small earthquake (sensor $9\mathrm{EAA}_\mathrm{E}$ in Figure 6.13 b). However, since no peak is visible in the East component, or in the results from the five Bosnia sequence earthquakes, it cannot be considered a reliable result that would indicate that energy is transmitted from the structure to its surroundings. In all the presented deconvolved wavefields in Figures 6.13 and 6.14, the oscillation visible at the top of the structure is damped by the structure, and no vibrational energy is released back to the surrounding ground.

To check if the energy of the vibrating oscillator can be observed in the recordings at the bottom of the structure, additionally, the spectrograms of the recordings at the top and the bottom of the structure were calculated. Example spectrograms of the small earthquake and the A.9 earthquake from the Bosnia sequence are shown in Figures 6.15 and 6.16, respectively.

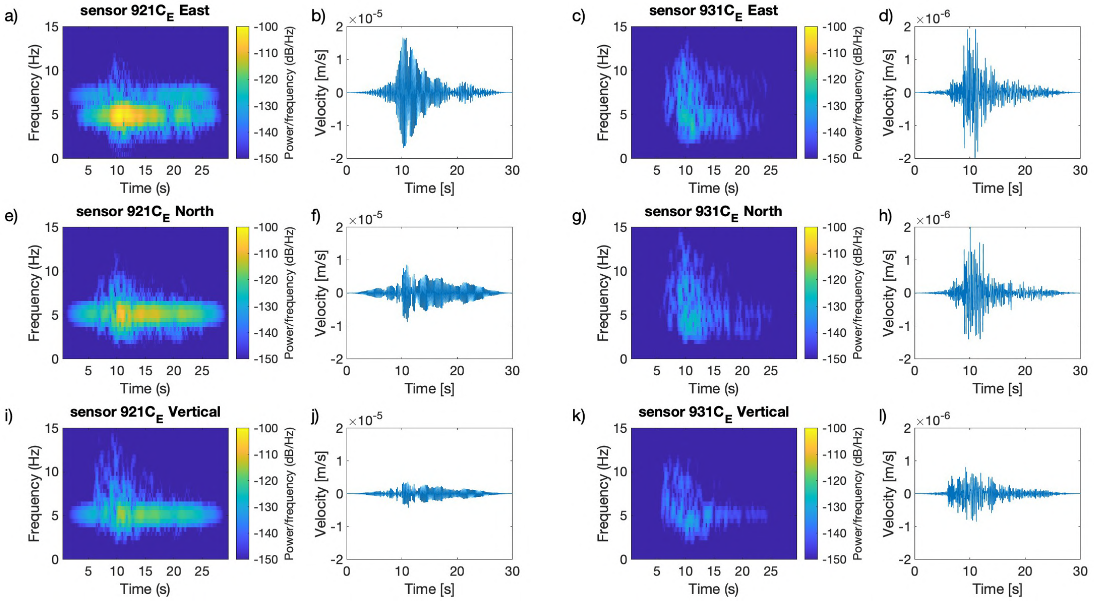

Figure 6.15: Comparison of the spectrograms of the earthquake data recorded at the top of the structure (a, e, and i) and the foundation (c, g, k) for the small earthquake (B.1 Table A.2). On the right side of each spectrogram is the corresponding time history of the data. The y-axis scale in subplots d), h), and l) is 10 times smaller than in b), f) and j).

In the spectrogram from sensor $921\mathrm{C}_\mathrm{E}$ (top slab), the clear trace of energy around the resonant frequency of the structure is visible for both presented earthquakes, for all three analyzed components. The spectrograms of the recordings from the sensor installed at the bottom slab of the structure show much lower energy. In the spectrogram of the small earthquake recordings (Figure 6.15), there is only a small amount of energy around the resonant frequency of the structure. A trace around 5 Hz is visible in the spectrogram of the North and Vertical components. For the

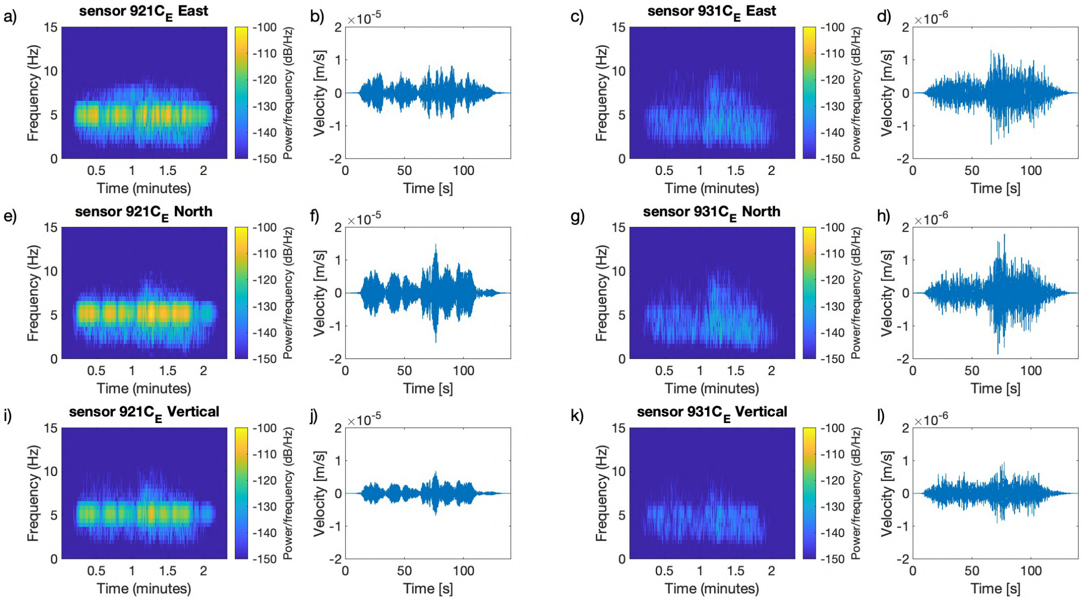

Figure 6.16: Comparison of the spectrograms of the earthquake data recorded at the top of the structure (a, e, and i) and the foundation (c, g, k) for one earthquake (A.9 Table A.1) from the Bosnia sequence. On the right side of each spectrogram is the corresponding time history of the data. The y-axis scale in subplots d), h), and l) is 10 times smaller than in b), f) and j).

East component, the energy is more spread out, and a trace at 5 Hz cannot be identified. In the spectrograms calculated from an example of the Bosnia sequence earthquake (Figure 6.16), the results show that the amount of energy transmitted from the oscillating slab to the foundation of the structure is small. Therefore, the spectrograms of the sensors installed at the top and the bottom of the structure revealed that there was not much energy transmitted from the oscillator to the foundation of the structure.

For a structure with a surface foundation, such as the one constructed in Piana di Toppo, it is possible to compute the radiation damping proposed by Gazetas (1991). Radiation damping describes the dissipation of energy by waves propagating away from the foundation (Gazetas, 1980). For each mode, an equivalent damping ratio can be defined. For the translational modes, the damping ratio is as expressed as

$$\xi_j = \frac{C_j}{2\sqrt{\bar{K}_j m}} \quad (j = z, x, y). \tag{6.10}$$

The damping ratio for rotational modes can be expressed as

$$\xi_l = \frac{C_l}{2\sqrt{\bar{K}_l I_p}} \quad (l = \theta x, \theta y;\ p = x, z). \tag{6.11}$$

Where $\bar{K}$ is the dynamic stiffness, C is the radiation damping coefficient. m is the mass of the structure and I_p is the mass moment of inertia about the p axis. More details about the radiation damping calculation can be found in (Gazetas, 1991).

The impedance functions were calculated using the shear wave velocity of the upper soil layer of the Piana di Toppo test site equal to 551 m/s (see Table 4.4). The radiation damping ratios for all identified modes are presented in Table 6.2.

High values of radiation damping ratios indicate that the waves radiated from an oscillating structure are emitted in phase and "reach" long distances away from the foundation. Consequently, low radiation damping ratios indicate out-of-phase waves which cannot "reach" long distances and in effect, they dissipate little energy from the oscillating foundation (Gazetas, 1991).

Table 6.2: Radiation damping ratio of the three modes of the Piana di Toppo structure calculated based on Gazetas (1991).

Frequency:	4.8 Hz	5.1 Hz	7.1 Hz
ξ_z	2.59 %	2.72 %	3.90 %
ξ_x	1.99 %	2.09 %	2.99 %
ξ_y	1.69 %	1.78 %	2.53 %
$\xi_{\theta x}$	0.01 %	0.02 %	0.04 %
$\xi_{\theta y}$	0.02 %	0.02 %	0.05 %

The calculated radiation damping ratios show that with the geometry of the structure built on the Piana di Toppo test site, and the characteristics of the soil, the radiation of the energy from the structure is minor. Such small radiation damping ratios are the effect of the combination of the stiff soil with high shear wave velocity, V_s, and the stiffness of the structure. Therefore, the results of the radiation damping ratios presented in Table 6.2 support the deconvolution results where the phase related to the energy radiated from the structure to the ground is not distinguishable.

6.4 Summary

The analyses of the Piana di Toppo experiment showed that the built structure, designed to resemble a single-degree-of-freedom system, did not transmit shaking energy back to the ground. The lack of energy transmission prevented the successful application of the approach proposed in this thesis. The reason why the approach could not be successfully applied to the Piana di Toppo test site could be a combination of the low energy of the earthquakes used for the analysis, poor coupling of the sensors with the structure, and the chosen design and characteristics of the materials of the structure. Additionally, radiation of the energy from the vibrating structure to its surroundings could be affected by the fact that the foundation slab was prefabricated, and there was no full contact with the ground. The results show that such a soil-structure interaction experimental design might not be appropriate for replicating the building-soil interaction which was observed in the Matera test site.

Chapter 7

Conclusions and final remarks

7.1 Synthesis of the thesis

In this thesis, I analyzed soil-structure interaction in terms of wave propagation. I proposed a new approach for earthquake data analysis that combines, in an innovative way, two methods already widely used in seismology and engineering seismology studies: deconvolution and polarization analysis. The proposed approach is composed of four main steps: 1) estimation of the dynamic behavior of the building, 2) deconvolution of the earthquake recordings coming from the building and its surroundings, 3) identification of the seismic phases, reconstruction of the signal transmitted from the building to its surroundings, and energy estimation, and 4) polarization analysis.

The main objective of the PhD project was to identify the wavefield radiated from the building and estimate the amount of energy associated with it using the proposed approach for soil-structure interaction assessment. To test the approach, I analyzed data from two SSI experimental campaigns, one conducted in Matera in October 2019 and the other in Piana di Toppo in April 2022.

Using the proposed approach, I estimated the deconvolved wavefield and I showed that, with the support of the developed analytical transfer function, it is possible to identify the wavefield released from the building to the ground. In the time domain, the analytical model used for the identification of the peaks in the Matera test case had three peaks: two associated with the up- and down-going wavefield in the building, and a third related to the wavefield transmitted from the building to its surroundings.

The polarization analysis of both the deconvolved wavefield and the reconstructed signal related to the energy transmitted from the Matera building to its surroundings provided complimentary results that indicate that the polarization in the analyzed frequency band was mostly linear. These results indicated that the transmitted wavefield was not characterized by classically polarized surface waves. The observed polarization of the particle motion could be explained by e.g., quasi-Rayleigh waves, characterized by three planes, where radial and transverse components have a phase shift and the particle motion in the horizontal plane is elliptic (Yanovskaya and Savina, 2004), or a combination of the quasi-Rayleigh and quasi-Love waves, which do not have strictly transverse motion (Tanimoto, 2004).

The preliminary results from the Piana di Toppo experiment showed that the built structure, which was designed to resemble a single-degree-of-freedom system, did not transmit shaking energy back to the ground. This prevented the successful estimation of the radiated wavefield from the structure and estimation of the radiated energy. The possible explanation for these observations could be a combination of the low energy of the earthquakes used for the analysis, poor coupling of the sensors with the structure, and the chosen design of the structure. The results suggest that an experiment design might not be appropriate for analyzing the soil-structure interaction phenomenon in the Piana di Toppo test site.

7.2 Outlook

Based on the results obtained with the proposed approach for soil-structure interaction assessment in terms of wave propagation, I attempt to answer several open scientific questions in the field of engineering seismology, as stated in the Introduction.

Is it possible to estimate the impact of the building on the surroundings? How does a vibrating building interact with its surroundings? Is the footprint of the shaking, in terms of wave propagation, significant?

In this work, I presented a new approach that enables the reconstruction of the wavefield related to the energy radiated from a vibrating structure to its surroundings on the surface. By analyzing earthquake recordings of three three-component sensors installed at the top and bottom of a building and on the surface at a sufficient distance from the building, it is possible to reconstruct the wavefield of interest. This can be obtained by applying the constrained deconvolution method (Bindi et al., 2010) on the deconvolved wavefield, using the sensor at the top of the building as the reference one (similar to Petrovic and Parolai, 2016). After identification of the phase of the deconvolved wavefield related to the energy transmitted from the building, the positivity constraint is applied, and the Fourier spectra of the constrained phase are convolved with the spectra of the recordings at the top of the building. The outcome is a representation of the seismic wavefield that relates only to the energy radiated from the shaking building at the surrounding ground surface.

The analysis presented in this study showed that the most significant impact of the vibrating building on the ground motion was near the resonant frequencies of the building itself. In the case at hand, the presence of the building instrumented during the experiment carried out in Matera decreased the ground motion caused by an earthquake (assuming that there is no building) in the studied frequency band. In the case of the Matera test site, the energy of the wavefield transmitted from the building to the ground was up to 59 % of the energy of the earthquake signal registered on the athletic field. Such results suggest that the footprint of the shaking of a building might be significant in its surroundings, in terms of wave propagation.

The method developed in this thesis is complementary to previous SSI studies. With the help of an analytical model, it is possible to estimate the amplitude of the transmitted energy, which in the case of the Matera test site was equal to $(1-r)/2$. Additionally, by removing the influence of the building from the wavefield recorded on the ground surface it is possible to study ground shaking as if there was no building. This part of the approach enables a detailed study of the interaction of the vibrating building with its surroundings. By combining the proposed approach with the joint deconvolution approach proposed by Petrovic and Parolai (2016) for analysis of earthquake recordings coming from an instrumented building and nearby borehole, it is possible to reconstruct the seismic wavefield radiated from a building to its surroundings both in the horizontal (this thesis) and vertical (Petrovic and Parolai, 2016) dimensions.

Could the characterization of the wavefield transmitted from a vibrating building into its surroundings be useful for improving the seismic design of structures in the future? Can polarization analysis of the radiated wavefield improve the understanding of SSI/SCI effects?

The proposed approach enables the identification of the wave types that compose the wavefield and the energy of the signal radiated from a building. Knowledge of the polarization and the energy of the transmitted waves provide information on the buildings that act as secondary sources of vibration during an earthquake. By analyzing the particle motion and polarization ellipse parameters of the radiated wavefield it is possible to obtain qualitative information on the wave types that compose the signal transmitted from the building to its surroundings on the surface.

One of the future goals in the design of structures could be that their spatial distribution helps to mitigate the impact of an earthquake by damping the amplitude of the shaking. Knowledge of the energy and particle motion of the wavefield generated by a building provides information about the potential additional load that could affect the surrounding area and could be considered in the future design of nearby buildings.

Moreover, with the information about the wave propagation velocity and the dominant frequency content of the radiated motion, it is possible to calculate the dominant wavelength of the released wavefield. The wavelength information could be used to estimate the location of the maxima, minima, and zeros of the signal coming from the building (Figure 7.1a). By evaluating the radiated wavefield using earthquake recordings coming from two already existing nearby buildings, it may be possible to evaluate the effects of their vibrations on the wavefield generated between them. Thus, the estimated modifications to the wavefield between the vibrating buildings could be used to understand where amplification of the signal radiated from nearby structures might be expected (Figure 7.1b). Simply put, if a new building with known dynamic properties was about to be constructed, estimating the wavefield radiated from this building could help in assessing the position of the building that could cause amplification or de-amplification of the signal in between (Figure 7.1b,c). Knowing the characteristics of the radiated wavefields from an already constructed building could help in estimating the location of a new building to avoid positive interference patterns (Figure 7.1b).

Additionally, knowledge of the dominant wavelength of the radiated wavefield, combined with the polarization analysis, could provide information about locations of positive and negative wavefield interference for a given earthquake motion (Figure 7.2). If the polarization of the surface ground motion produced by an earthquake (Figure 7.2a) interacts with the wavefield transmitted from a vibrating building (Figure 7.2b) it may modify the ground motion in the surroundings of the building (Figure 7.2c). A radiated wavefield polarized in the horizontal plane could interact with the horizontal motion of the ground resulting in an overall amplification or de-amplification of the wavefield in the surroundings of the building (Figure 7.2c).

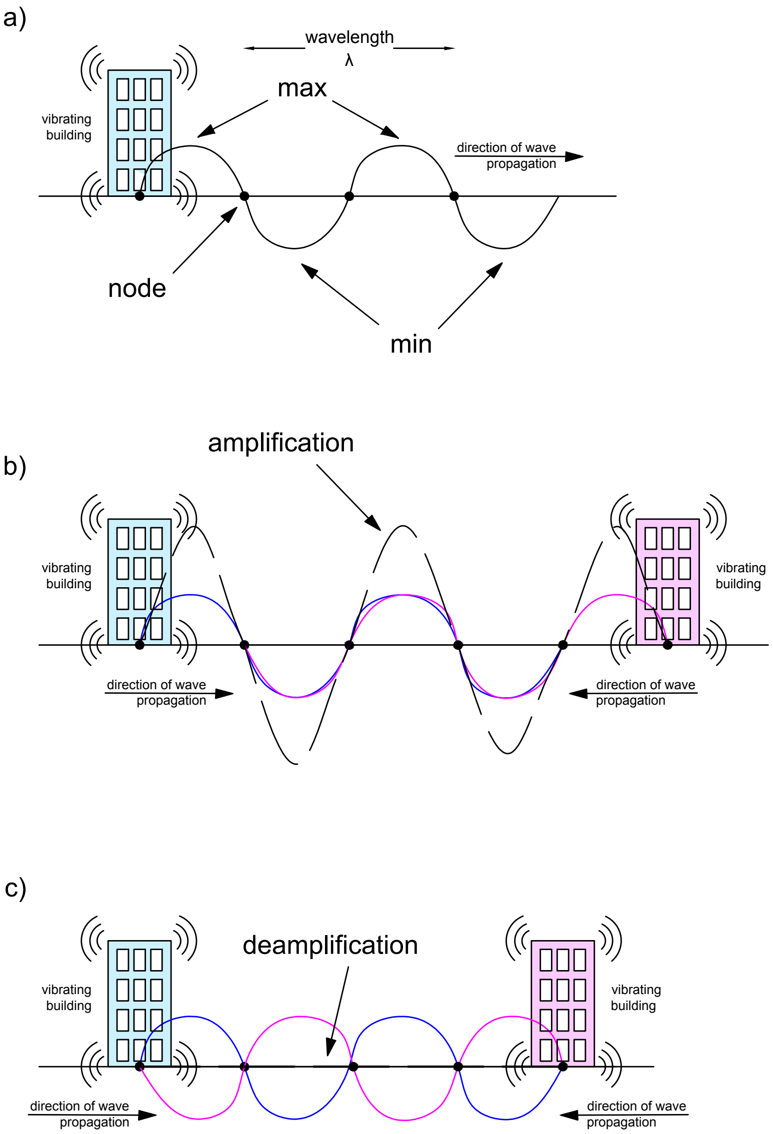

Figure 7.1: Schematic drawing of the changes to the radiated wavefield caused by buildings. a) Wavefield radiated from a vibrating building with indicated maxima, minima, and zeros of the wave. b) The case of amplification of the wavefield in between two buildings radiating in-phase wavefields. The amplified signal is indicated with the dashed line. c) The case of de-amplification of the wavefield in between two buildings radiating out-of-phase wavefields.

The characterization of the radiated wavefield (e.g., knowledge of the dominant wavelength, location of the zeros, maxima, and minima, and polarization) could help to identify locations where a future building should not be constructed or the areas where the properties of the buildings should be adjusted (stiffening or softening slightly the structure). Additionally, regions likely to be subjected to increased shaking, could be defined as "no development area" through a district plan. By analyzing soil-structure interaction using the approach proposed in this thesis, it could be possible to avoid the positive interference of the input motion with the radiated wavefield. With the knowledge of the radiated wavefield, the new buildings could be designed in a way to generate energy that would cancel our with the energy radiated from another building.

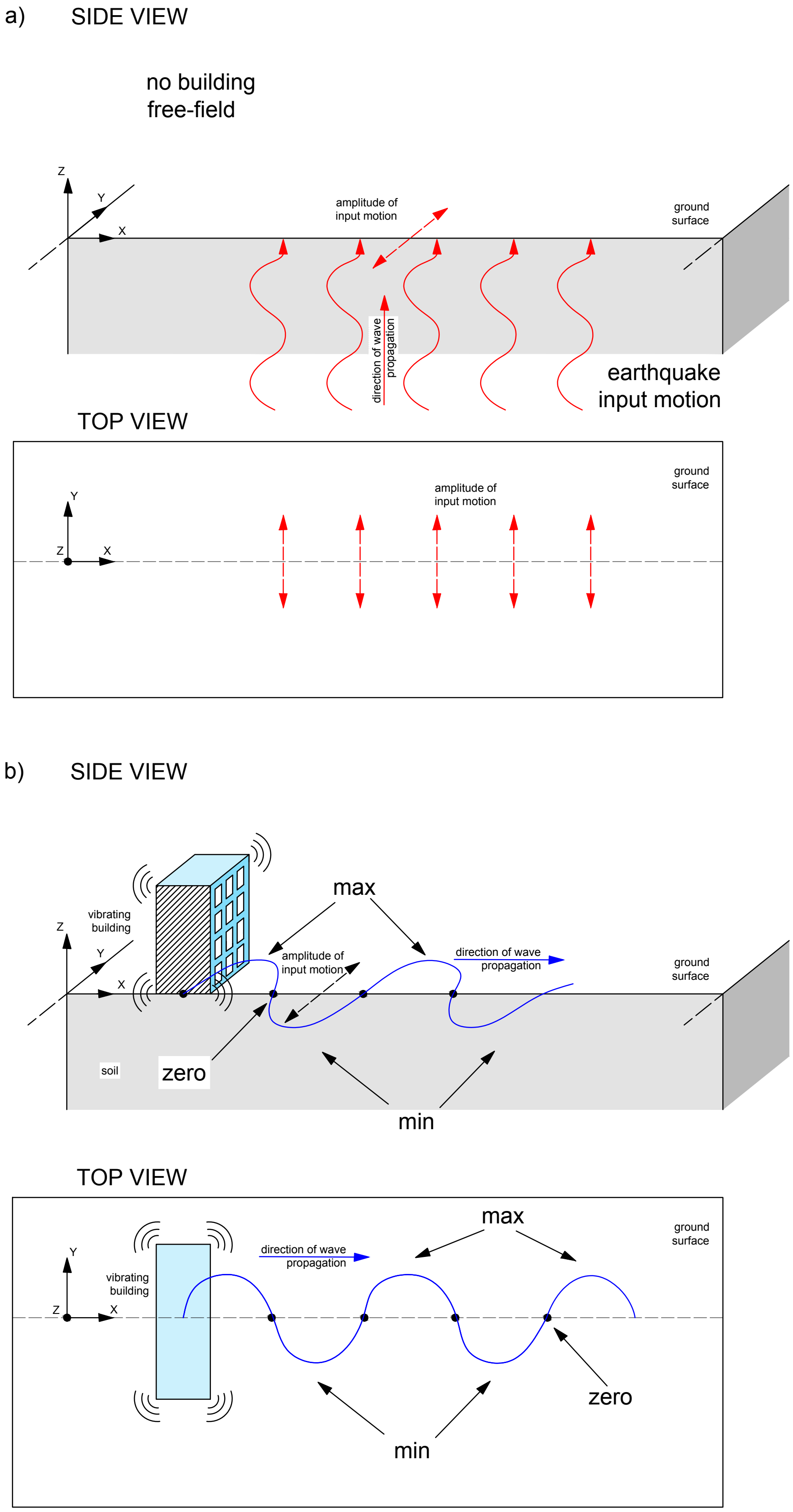

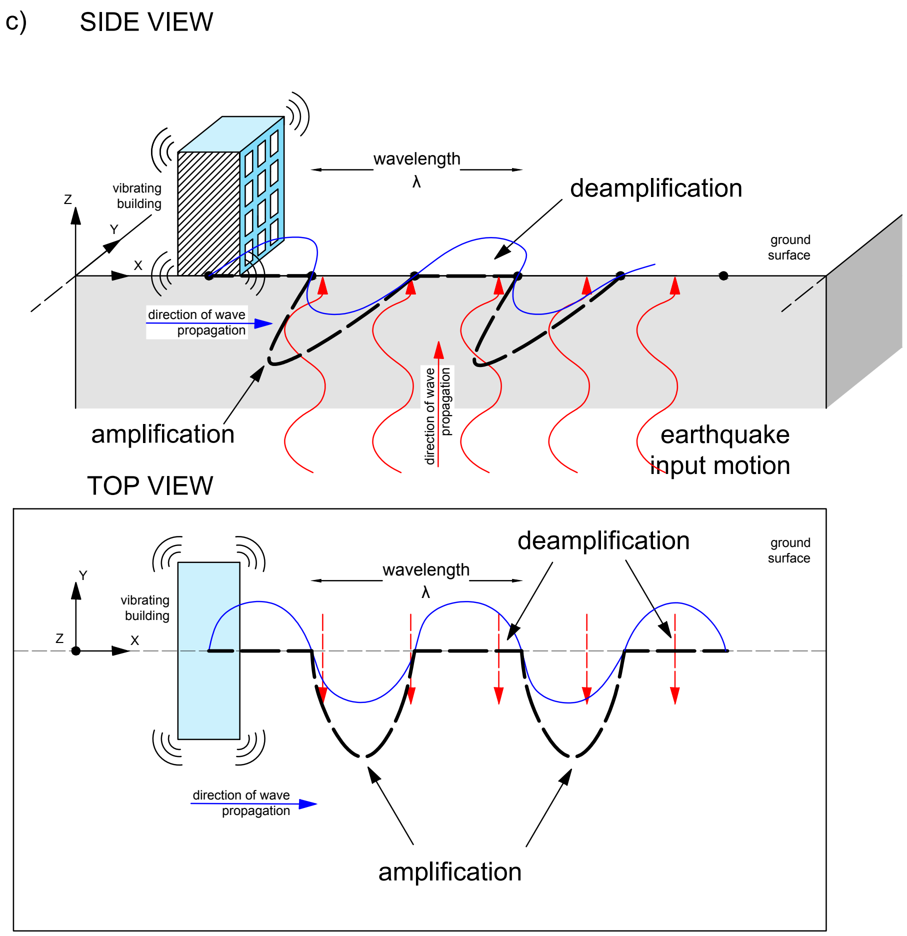

Figure 7.2: Schematic drawing of the changes to the radiated wavefield caused by buildings. a) Amplitude of the earthquake input motion (red solid curved arrows) at the surface in the free-field (red dashed arrows). b) Amplitude of motion of the wavefield radiated from a vibrating building to its surroundings at the ground surface with indicated maxima, minima, and zeros of the propagating wave. c) Surface interaction between the wavefield radiated from a building and the ground motion caused by an earthquake at a certain time t. The blue lines indicate the wavefield radiated by a vibrating building. The black dashed line indicates the modified wavefield with possible areas of amplification and de-amplification of the signal caused by constructive and destructive interference. In all plots, X-Y defines the surface plane. The top view shows the ground motion at a certain time t at the surface. Apart from input ground motion indicated with red curved arrows in a) and c), solid blue, red and black dashed lines refer to the surface motion.

7.3 Limitations and implications

Due to the limited duration of the experimental campaigns and the unforeseeable occurrence of earthquakes, the presented study is based on a limited dataset. The real building analysis using the data coming from the Matera experiment is based on the recordings of one earthquake with only a moderate level of shaking. In addition, the Matera test site might represent only one of the building-soil conditions. The results, therefore, should be considered valid only for similar events at this specific site. More case studies should be analyzed to draw more general conclusions about soil-structure interactions. Additionally, the lack of different magnitudes of shaking and the lack of strong motion recordings made it impossible to study the influence of non-linearity on the polarization of the wavefield radiated from the building to its surroundings.

In the case of the Matera data analysis, another limitation was the lack of a numerical model representing the building and the soil of the test site to compare and verify the results. Moreover, since the analysis was performed on a limited frequency band, it may not accurately represent reality, containing a wider frequency spectrum.

7.4 Overall conclusions and recommendations for further work

For the Matera test site, the radiated wavefield was estimated to consist of unconventionally polarized surface waves. Since the second experiment did not provide suitable data for a second analysis using the proposed approach, the study is based on recordings from only one earthquake and more data must be analyzed to confirm these observations. However, the experiment conducted in the Piana di Toppo test site showed that an experiment designed in such a way may not be suitable for the study of SSI in the case of a large impedance contrast.

To overcome the limitations of this study, I propose additional analyses to obtain complementary results in future work:

- a numerical model of an analyzed structure and the surrounding ground should be combined with the data analysis to additionally verify and interpret obtained results;

- the proposed approach should be applied to a larger dataset with different levels of shaking to obtain statistical information on the characteristics of the radiated wavefield. In addition, the use of strong ground motion recordings would allow validation and eventual modification of the approach for the analysis of possible non-linear effects on the polarization and energy of the wavefield radiated from a structure to the ground;

- additional experiments should be performed in more SSI-prone areas than the Matera and Piana di Toppo experiments with lower impedance contrast, i.e., with the more flexible ground, with lower V_s, and using a stiffer structure. In this way, the heavier and stiffer medium (the structure) would have a greater impact on the lighter and more flexible one (the ground);

- attenuation effects should be considered in the analytical model in order to have a more accurate model and to be able to consider the amplitude of the deconvolved wavefield;
- the proposed approach should be additionally tested in a controlled laboratory environment (e.g., using the data coming from a shaking table or centrifugal laboratory tests);
- testing the approach using data from an environment with dense urban setting.

To validate the results obtained using the proposed approach, further analyzes should be carried out in the future with different datasets. In addition, the proposed methodology should be extended to the analysis of seismic noise recordings (e.g., development of an analytical model describing transfer function with the seismic noise input for the seismic phase identification in the deconvolved wavefield - different input wavefield and propagation), which would provide a method for analyzing SSI with a larger amount of more easily obtainable data.

The SSI phenomenon still requires much further research to be fully understood and properly taken into consideration when designing and constructing new structures or planning future urban environments, especially in areas with high seismic risk. Understanding the dynamic interaction between existing buildings in the urban environment is therefore of high importance to minimize the impact that earthquakes may have on the urban built environment, and to minimize potential human and economic losses.

Bibliography

Aki, R. and Richards, P. (1981). *Quantitative seismology, theory and methods.* "University Science Books".

Amendola, C., de Silva, F., Vratsikidis, A., Pitilakis, D., Anastasiadis, A., and Silvestri, F. (2021). Foundation impedance functions from full-scale soil-structure interaction tests. *Soil Dynamics and Earthquake Engineering*, 141(August 2020):106523.

Astorga, A., Guéguen, P., and Kashima, T. (2018). Nonlinear elasticity observed in buildings during a long sequence of earthquakes. *Bulletin of the Seismological Society of America*, 108(3):1185–1198.

Bard, P.-Y., Guéguen, P., and Wirgin, A. (1996). A note on the seismic wavefield radiated from large building structures into soft soils. In *11th World Conference on Earthquake Engineering (WCEE).*

Bindi, D., Boxberger, T., Orunbaev, S., Pilz, M., Stankiewicz, J., Pittore, M., Iervolino, I., Ellguth, E., and Parolai, S. (2015a). On-site early-warning system for bishkek (Kyrgyzstan). *Annals of Geophysics*, 58(1).

Bindi, D., Parolai, S., Picozzi, M., and Ansal, A. (2010). Seismic input motion determined from a surface-downhole pair of sensors: A constrained deconvolution approach. *Bulletin of the Seismological Society of America*, 100(3):1375–1380.

Bindi, D., Petrovic, B., Karapetrou, S., Manakou, M., Boxberger, T., Raptakis, D., Pitilakis, K. D., and Parolai, S. (2015b). Seismic response of an 8-story RC-building from ambient vibration analysis. *Bulletin of Earthquake Engineering*, 13(7):2095–2120.

Braile, L. (2022). Seismic wave demonstrations and animations. Purdue University. `http://web.ics.purdue.edu/~braile/edumod/waves/WaveDemo.htm` (visited on 21/07/2022).

Brincker, R., Zhang, L., and Andersen, P. (2001). Modal identification of output-only systems using frequency domain decomposition. *Smart Materials and Structures*, 10(3):441–445.

Cardenas, M., Bard, P.-Y., Guéguen, P., and Chavez-Garcia, F. J. (2000). Soil-structure interaction in mexico city. wave field radiated away from jalapa building: Data and modelling. In *Proc. of the 12th World Conference on Earthquake Engineering.* 12 WCEE 2000, Auckland, New Zeland. Paper No. 385.

Chandra, J. and Guéguen, P. (2019). Nonlinear response of soil–structure systems using dynamic centrifuge experiments. *Journal of Earthquake Engineering*, 23(10):1719–1741.

Chávez-García, F. J. and Cárdenas-Soto, M. (2002). The contribution of the built environment to the 'free-field' ground motion in Mexico City. *Soil Dynamics and Earthquake Engineering*, 22(9-12):773–780.

Chazelas, J.-l., Central, L., and Abraham, O. (2001). Identification of Different Seismic Waves Generated by Foundation Vibration in the Centrifuge: Travel Time, Spectral and Numerical Investigations. In *International Conferences on Recent Advances in Geotechnical Earthquake Engineering and Soil Dynamics.*

CLARA project (2020). Clara WebGIS. `https://smartcities-matera-clara.imaa.cnr.it/`.

Clayton, R. W. and Wiggins, R. A. (1976). Source shape estimation and deconvolution of teleseismic bodywaves. *Geophysical Journal International*, 47(1):151–177.

Clotaire, M., Guéguen, P., and Bard, P.-Y. (2008). Dynamic parameters of structures extracted from ambient vibration measurements: an aid for the seismic vulnerability assessment of existing buildings in moderate seismic hazard regions. *Soil Dynamic and Earthquake Engineering*, pages 1–40.

Cremen, G. and Galasso, C. (2020). Earthquake early warning: Recent advances and perspectives. *Earth-Science Reviews*, 205(February):103184.

De Risi, R., Penna, A., and Simonelli, A. L. (2019). Seismic risk at urban scale: the role of site response analysis. *Soil Dynamics and Earthquake Engineering*, 123(May):320–336.

Ditommaso, R., Mucciarelli, M., Parolai, S., and Picozzi, M. (2012). Monitoring the structural dynamic response of a masonry tower: Comparing classical and time-frequency analyses. *Bulletin of Earthquake Engineering*, 10(4):1221–1235.

Dreossi, I. and Parolai, S. (2022). Robust estimation of 1D shear-wave quality factor profiles for site response analysis using seismic noise. *Soil Dynamics and Earthquake Engineering*, 161(June):107387.

Euro-Seistest (1995). An European Test-Site for Engineering Seismology, Earthquake Engineering and Seismology, Final Scientific Report. Technical report, EV.5V-CT93-0281, Vol. 1–5.

Fares, R., Santisi d'Avila, M. P., and Deschamps, A. (2019). Soil-structure interaction analysis using a 1DT-3C wave propagation model. *Soil Dynamics and Earthquake Engineering*, 120(February):200–213.

Gallipoli, M., Calamita, G., Tragni, N., Pisapia, D., Lupo, M., Mucciarelli, M., Stabile, T., Perrone, A., Amato, L., Izzi, F., La Scaleia, G., Maio, D., and Salvia, V. (2020). Evaluation of soil-building resonance effect in the urban area of the city of matera (Italy). *Engineering Geology*, 272:105645.

Gallipoli, M. and Lupo, M. (2012). Caratterizzazione dei terreni e risposta sismica locale dell'area urbana di Matera. Tecniche speditive per la stima dell'amplificazione sis- mica e della dinamica degli edifici Studi teorici ed applicazioni professionali a cura di Marco Mucciarelli (In Italian). *ARACNE editrice S.r.l.*, page 323–342.

Gazetas, G. (1980). Static And Dynamic Displacements of Foundations on Heterogeneous Multilayered Soils. *Geotechnique*, 30(2):159–177.

Gazetas, G. (1991). *Foundation Vibrations.* Springer US, Boston, MA.

Guéguen, P. and Bard, P.-Y. (2005). Soil-structure and soil-structure-soil interaction: Experimental evidence at the volvi test site. *Journal of Earthquake Engineering*, 9(5):657–693.

Guéguen, P., Bard, P.-Y., and Chavez-Garcia, F. J. (2002). Site-city seismic interaction in mexico city–like environments: An analytical study. *Bulletin of the Seismological Society of America*, 92(2):794–811.

Guéguen, P., Bard, P.-Y., and Oliveira, C. S. (2000). Experimental and Numerical analysis of Soil Motions caused by free vibrations of a building model. *Bulletin of the Seismological Society of America*, 90(6):1464–1479.

Guéguen, P., Johnson, P., and Roux, P. (2016). Nonlinear dynamics induced in a structure by seismic and environmental loading. *The Journal of the Acoustical Society of America*, 140(1):582–590.

Guéguen, P., Langlais, M., Roux, P., Schinkmann, J., and Douste-Bacqué, I. (2014). Frequency and damping wandering in existing buildings using the random decrement technique. *7th European Workshop on Structural Health Monitoring, EW-SHM 2014 - 2nd European Conference of the Prognostics and Health Management (PHM) Society*, pages 2076–2082.

Guéguen, P., Mercerat, D. E., and Alarcon, F. (2019). Parametric Study on the Interpretation of Wave Velocity Obtained by Seismic Interferometry in Beam-Like Buildings. *Bulletin of the Seismological Society of America*, 109(5):1829–1842.

Isbiliroglu, Y., Taborda, R., and Bielak, J. (2015). Coupled soil-structure interaction effects of building clusters during earthquakes. *Earthquake Spectra*, 31(1):463–500.

Isbiliroglu, Y. D., Taborda, R., and Bielak, J. (2013). Coupled soil-structure interaction effects of building clusters during earthquakes. *Earthquake Spectra*, 31(1):463–500.

Jaimes, N., Prieto, G. A., and Rodriguez, C. (2022). Detection of Building Response Changes Using Deconvolution Interferometry: A Case Study in Bogota, Colombia. *Seismological Research Letters*, 93(2):931–942.

Janusz, P., Perron, V., Knellwolf, C., and Fäh, D. (2022). Combining Earthquake Ground Motion and Ambient Vibration Recordings to Evaluate a Local High-Resolution Amplification Model—Insight From the Lucerne Area, Switzerland. *Frontiers in Earth Science*, 10(May):1–19.

Jennings, P. C. (1970). Distant motions from a building vibration test. *Bulletin of the Seismological Society of America*, 60(6):2037–2043.

Kaklamanos, J., Cabas, A., Parolai, S., and Guéguen, P. (2021). Introduction to the special section on advances in site response estimation. *Bulletin of the Seismological Society of America*, 111(4):1665–1676.

Kanai, K. (1965). Some new problems of seismic vibrations of a structure. In *Proceedings of the 3rd world conference on earthquake engineering*. Auckland and Wellington, New Zealand.

Kazemnia Kakhki, M., Mansur, W. J., and Peters, F. C. (2020). Rayleigh wave separation using high-resolution time-frequency polarization filter. *Geophysical Prospecting*, 68(7):2104–2118.

Kham, M., Semblat, J.-F., Bard, P.-Y., and Dangla, P. (2006). Seismic Site–City Interaction: Main Governing Phenomena through Simplified Numerical Models. *Bulletin of the Seismological Society of America*, 96(5):1934–1951.

Kitada, Y., Hirotani, T., and Iguchi, M. (1999). Models test on dynamic structure-structure interaction of nuclear power plant buildings. *Nuclear Engineering and Design*, 192(2):205–216.

Kohler, M. D., Heaton, T. H., and Bradford, S. C. (2007). Propagating waves in the steel, moment-frame factor building recorded during earthquakes. *Bulletin of the Seismological Society of America*, 97(4):1334–1345.

Konno, K. and Ohmachi, T. (1998). Ground-motion characteristics estimated from spectral ratio between horizontal and vertical components of microtremor. *Bulletin of the Seismological Society of America*, 88(1):228–241.

Kramer, S. L. (1996). *Geotechnical earthquake engineering.* Pearson Education India.

Kumar, N. and Narayan, J. P. (2017). Quantification of site–city interaction effects on the response of structure under double resonance condition. *Geophysical Journal International*, 212(1):422–441.

Kumar, N. and Narayan, J. P. (2019). Effects of site–city interaction and polarization of the incident S-wave on the transfer function and fundamental frequency of structures. *Natural Hazards*, 97(2):747–774.

Lanzo, G. and Silvestri, F. (2016). *Risposta sismica locale pocket. Teoria ed esperienze.* Hevelius.

Liang, J., Fu, J., Todorovska, M. I., and Trifunac, M. D. (2013a). Effects of site dynamic characteristics on soil-structure interaction (II): Incident P and SV waves. *Soil Dynamics and Earthquake Engineering*, 51(June 2019):58–76.

Liang, J., Fu, J., Todorovska, M. I., and Trifunac, M. D. (2013b). Effects of the site dynamic characteristics on soil–structure interaction (i): Incident sh-waves. *Soil Dynamics and Earthquake Engineering*, 44:27–37.

Manos, G. C., Demosthenous, M., Triamataki, M., Yasin, B., and Skalkos, P. (1995). Construction and instrumentation of a 5 storey masonry in- filled rc building at the volvi-thessaloniki euro-seistest site. cor- relation of measured and numerically predicted dynamic properties. In *Proc. of the Third International Conference on Earthquake Engineering*.

Massa, M., Marzorati, S., Ladina, C., and Lovati, S. (2010). Urban seismic stations: Soil-structure interaction assessment by spectral ratio analyses. *Bulletin of Earthquake Engineering*, 8(3):723–738.

Michel, C., Edwards, B., Poggi, V., Burjánek, J., Roten, D., Cauzzi, C., and Fäh, D. (2014). Assessment of site effects in alpine regions through systematic site characterization of seismic stations. *Bulletin of the Seismological Society of America*, 104(6):2809–2826.

Michel, C., Guéguen, P., Arem, S. E. L., Mazars, J., and Kotronis, P. (2010). Full Scale Dynamic Response of a Rc Building Under. *Earthquake Engineering and Structural Dynamics*, 39(4):419–441.

Michel, C., Guéguen, P., and Bard, P.-Y. (2008). Dynamic parameters of structures extracted from ambient vibration measurements: An aid for the seismic vulnerability assessment of existing buildings in moderate seismic hazard regions. *Soil Dynamics and Earthquake Engineering*, 28(8):593–604.

Mordret, A., Sun, H., Prieto, G. A., Toksöz, M. N., and Büyüköztürk, O. (2017). Continuous monitoring of high-rise buildings using seismic interferometry. *Bulletin of the Seismological Society of America*, 107(6):2759–2773.

Münchmeyer, J., Bindi, D., Leser, U., and Tilmann, F. (2021). The transformer earthquake alerting model: A new versatile approach to earthquake early warning. *Geophysical Journal International*, 225(1):646–656.

Nakata, N. and Snieder, R. (2013). Monitoring a Building Using Deconvolution Interferometry. II: Ambient-Vibration Analysis. *Bulletin of the Seismological Society of America*, 104(1):204–213.

Nakata, N., Snieder, R., Kuroda, S., Ito, S., Aizawa, T., and Kunimi, T. (2013). Monitoring a Building Using Deconvolution Interferometry. I: Earthquake-Data Analysis. *Bulletin of the Seismological Society of America*, 103(3):1662–1678.

Paolucci, R. (1993). Soil-structure interaction effects on an instrumented building in Mexico City. *European Earthquake Engineering*, 3:33–44.

Park, J. and Yu, Y. (1992). Anisotropy and coupled free oscillations: simplified models and surface wave observations. *Geophysical Journal International*, 110(3):401–420.

Park, J. and Yu, Y. (1993). Seismic determination of elastic anisotropy and mantle flow. *Science*, 261(5125):1159–1162.

Parolai, S. (2012). Investigation of site response in urban areas by using earthquake data and seismic noise. In Bormann, P., editor, *New Manual of Seismological*

Observatory Practice (NMSOP-2), pages 1 – 38. GFZ German Research Centre for Geosciences, Potsdam, Germany.

Parolai, S., Ansal, A., Kurtulus, A., Strollo, A., Wang, R., and Zschau, J. (2009). The ataköy vertical array (turkey): insights into seismic wave propagation in the shallow-most crustal layers by waveform deconvolution. *Geophysical Journal International*, 178(3):1649–1662.

Parolai, S., Bindi, D., Ansal, A., Kurtulus, A., Strollo, A., and Zschau, J. (2010). Determination of shallow S-wave attenuation by down-hole waveform deconvolution: A case study in Istanbul (Turkey). *Geophysical Journal International*, 181(2):1147–1158.

Parolai, S., Fäcke, A., Richwalski, S. M., and Stempniwski, L. (2005). Assessing the Vibrational Frequencies of the Holweide Hospital in the City of Cologne (Germany) by Means of Ambient Seismic Noise Analysis and FE modelling. *Natural Hazards*, 34(2):217–230.

Petrovic, B. and Parolai, S. (2016). Joint deconvolution of building and downhole strong-motion recordings: Evidence for the seismic wavefield being radiated back into the shallow geological layers. *Bulletin of the Seismological Society of America*, 106(4):1720–1732.

Petrovic, B., Parolai, S., Pianese, G., Dikmen, S. U., Moldobekov, B., Orunbaev, S., and Paolucci, R. (2018). Joint deconvolution of building and downhole seismic recordings: an application to three test cases. *Bulletin of Earthquake Engineering*, 16(2):613–641.

Piana di Toppo (2022). Piana di Toppo website. `https://www.ogs.trieste.it/en/content/geop-borehole-geophysics`.

Pianese, G., Petrovic, B., Parolai, S., and Paolucci, R. (2018). Identification of the nonlinear seismic response of buildings by a combined stockwell transform and deconvolution interferometry approach. *Bulletin of Earthquake Engineering*, 16:3103–3126.

Pinnegar, C. R. (2006). Polarization analysis and polarization filtering of three-component signals with the time–frequency s transform. *Geophysical Journal International*, 165(2):596–606.

Pitilakis, D. and Clouteau, D. (2010). Equivalent linear substructure approximation of soil-foundation-structure interaction: Model presentation and validation. *Bulletin of Earthquake Engineering*, 8(2):257–282.

Pitilakis, D., Dietz, M., Wood, D. M., Clouteau, D., and Modaressi, A. (2008). Numerical simulation of dynamic soil–structure interaction in shaking table testing. *Soil Dynamics and Earthquake Engineering*, 28(6):453–467.

Poletto, F., Petronio, L., Farina, B., and Schleifer, A. (2011). Seismic interferometry experiment in a shallow cased borehole using a seismic vibrator source. *Geophysical Prospecting*, 59(3):464–476.

Rahmani, M. and Todorovska, M. I. (2021). Structural health monitoring of a 32-storey steel-frame building using 50 years of seismic monitoring data. *Earthquake Engineering and Structural Dynamics*, 50(6):1777–1800.

Reinoso, E., Quinde, P., Contreras, M., and Gomez, D. (2022). Identification of the highest risk buildings in Mexico City. Technical report, United Nations Office for Disaster Risk Reduction.

Richart, F., Hall, J., and Woods, R. (1970). *Vibrations of Soils and Foundations.* Prentice-Hall international series in theoretical and applied mechanics. Prentice-Hall.

Schwan, L., Boutin, C., Padrón, L. A., Dietz, M. S., Bard, P.-Y., and Taylor, C. (2016). Site-city interaction: Theoretical, numerical and experimental crossed-analysis. *Geophysical Journal International*, 205(2):1006–1031.

Seed, H. B., Romo, M. P., Sun, J. I., Jamie, A., and Lysmer, J. (1988). The Mexico Earthquake of September 19, 1985—Relationships between Soil Conditions and Earthquake Ground Motions. *Earthquake Spectra*, 4(4):687–729.

Seed, R. B., Dickenson, S. E., and Idriss, I. M. (1991). Principal geotechnical aspects of the 1989 Loma Prieta earthquake. *Soils and Foundations*, 31(1):1–26.

Seismic, N. (2022). Survey geometries for passive seismic. `https://www.napaseismic.org/education/survey-geometries/`.

Semblat, J. F., Kham, M., and Bard, P.-Y. (2008). Seismic-wave propagation in alluvial basins and influence of site-city interaction. *Bulletin of the Seismological Society of America*, 98(6):2665–2678.

Silva, V., Pagani, M., Schneider, J., and Henshaw, P. (2019). Assessing Seismic Hazard and Risk Globally for an Earthquake Resilient World. Technical report, Contributing Paper to GAR 2019.

Singh, S. K., Mena, E., and Castro, R. (1988). Some aspects of source characteristics of the 19 September 1985 Michoacan earthquake and ground motion amplification in and near Mexico City from strong motion data. *Bulletin of the Seismological Society of America*, 78(2):451–477.

Skłodowska, A. M., Holden, C., Guéguen, P., Finnegan, J. P., and Sidwell, G. (2021). Structural change detection applying long-term seismic interferometry by deconvolution method to a modern civil engineering structure (new zealand). *Bulletin of Earthquake Engineering*, 19:3551 – 3569.

Snieder, R. (2009). Extracting the time-domain building response from random vibrations. In Schanz, T. and Iankov, R., editors, *Coupled site and soil-structure interaction effects with application to seismic risk mitigation*, pages 283–292. Springer, Dordrecht.

Snieder, R. and Şafak, E. (2006). Extracting the Building Response Using Seismic Interferometry: Theory and Application to the Millikan Library in Pasadena, California. *Bulletin of the Seismological Society of America*, 96(2):586–598.

Stein, S. and Wysession, M. (2003). An Introduction to Seismology, Earthquakes, Earth Structure.

Stewart, J., Crouse, C., Hutchinson, T., Lizundia, B., Naeim, F., and Ostadan, F. (2012). Soil-structure interaction for building structures.

Stewart, J. P., Fenves, G. L., and Seed, R. B. (1999). Seismic Soil-Structure Interaction in Buildings. I: Analytical Methods. *Journal of Geotechnical and Geoenvironmental Engineering*, 125(1):26–37.

Stockwell, R. G., Mansinha, L., and Lowe, R. P. (1996). Localization of the complex spectrum: the s transform. *IEEE Transactions on Signal Processing*, 44(4):998–1001.

Tanimoto, T. (2004). The azimuthal dependence of surface wave polarization in a slightly anisotropic medium. *Geophysical Journal International*, 156(1):73–78.

Todorovska, M. I. and Trifunac, M. D. (2008). Impulse response analysis of the Van Nuys 7-storey hotel during 11 earthquakes and earthquake damage detection. *Structural Control and Health Monitoring*, 15(1):90–116.

Varone, C., Lenti, L., Martino, S., and Semblat, J. F. (2020). Spatial variability of the urban ground motion in a highly heterogeneous site-city configurations. *Bulletin of Earthquake Engineering*, 19(1).

Vidale, J. E. (1986). Complex polarization analysis of particle motion. *Bulletin of the Seismological Society of America*, 76(5):1393–1405.

Wirgin, A. and Bard, P.-Y. (1996). Effects of buildings on the duration and amplitude of ground motion in Mexico City. *Bulletin of the Seismological Society of America*, 86(3):914–920.

Wolf, J. P. (1985). Dynamic soil–structure interaction.

Yanovskaya, T. B. and Savina, L. S. (2004). Quasi-Rayleigh waves in the transversely isotropic half-space with inclined axis of symmetry. *Studia Geophysica et Geodaetica*, 48(1):251–264.

Yoshida, K. and Sasatani, T. (2008). Seismic vertical array analysis for phase decomposition. *Geophysical Journal International*, 174(2):707–718.

Appendix A

Appendix

A.1 List of earthquakes

Table A.1: List of earthquakes from INGV database registered by the ground sensors installed during Piana di Toppo experiment.

Nb.	Date (UTC)	Lat.	Lon.	Depth [Km]	Mag	Location
A.1	2022-04-09 16:21:47.38	46.3115	12.8203	10.5	1.0	2 km E Tramonti di Sopra
A.2	2022-04-10 00:58:03.81	42.2838	20.1968	4.4	4.2	Albania [Land]
A.3	2022-04-11 08:17:42.16	44.6163	10.0365	27.1	2.3	4 km W Terenzo
A.4	2022-04-12 09:59:49.54	45.6418	10.4498	8.6	1.1	3 km SE Sabbio Chiese
A.5	2022-04-13 09:34:31.76	45.557	10.3018	6.2	1.3	2 km NW Botticino
A.6	2022-04-13 22:19:00.26	44.7923	10.7363	4.0	2.7	4 km NW Correggio
A.7	2022-04-22 06:21:03.45	43.7598	13.6242	36.7	2.1	Costa Marchigiana Anconetana (Ancona)
A.8	2022-04-22 21:07:49.68	42.9522	18.0797	9.5	5.5	Bosnia and Herz. [Land]
A.9	2022-04-23 00:59:09.32	43.0705	18.0193	10.0	3.9	Bosnia and Herz. [Land]
A.10	2022-04-23 02:20:27.64	43.0365	18.0243	6.5	4.4	Bosnia and Herz. [Land]
A.11	2022-04-23 02:34:22.49	42.9572	18.056	10.0	3.6	Bosnia and Herz. [Land]
A.12	2022-04-24 04:27:55.39	42.9617	18.0463	20.6	5.1	Bosnia and Herz. [Land]
A.13	2022-04-25 07:36:51.60	46.4603	12.0957	8.4	1.3	5 km E Selva di Cadore

Table A.2: List of earthquakes from RTS database registered by the ground sensors installed during Piana di Toppo experiment.

Nb.	Date (UTC)	Lat.	Lon.	Depth [Km]	Mag	Location
B.1	2022-04-09 16:21:48	46.3033	12.8105	7.28	1.1	2 km ESE di Tramonti di Sopra (Pordenone)
B.2	2022-04-10 19:44:02	46.2842	12.6142	8.31	1.0	8 km ENE di Claut (Pordenone)
B.3	2022-04-11 11:02:56	46.3768	13.671	6.51	0.7	4 km N di Soca (SLOVENIA)
B.4	2022-04-11 16:10:35	45.7185	13.8135	1	1.5	1 km ENE di Monrupino (Trieste)
B.5	2022-04-14 04:23:04	46.1533	12.2473	8.64	0.8	2 km ENE di Belluno (Belluno)
B.6	2022-04-14 09:29:33	46.6315	13.6308	3.29	1.2	0 km O di Bad Bleiberg (AUSTRIA)
B.7	2022-04-14 09:45:04	46.0872	14.2177	18.2	1.1	4 km SSE di Poljane nad Skofjo Loko (SLOVENIA)
B.8	2022-04-14 10:09:05	46.1857	11.2008	1	0.9	2 km NO di Cembra (Trento)
B.9	2022-04-14 11:59:03	46.0533	13.6402	1	1.1	2 km SE di Anhovo (SLOVENIA)
B.10	2022-04-23 02:15:53	46.4872	10.628	9.06	1.1	14 km SSE di Stelvio (Bolzano)
B.11	2022-04-25 07:36:52	46.4683	12.078	5.02	1.2	4 km ENE di Selva di Cadore (Belluno)
B.12	2022-04-25 09:45:46	45.9548	13.6542	6.41	1.3	1 km ESE di Nova Gorica (SLOVENIA)
B.13	2022-04-26 01:56:11	46.089	14.3385	6.37	1.0	3 km NNE di Polhov Gradec (SLOVENIA)
B.14	2022-04-26 06:54:50	45.7382	14.0725	1	1.1	3 km NE di Senozece (SLOVENIA)

A.2 Grid search uncertainties

In the wave propagation velocity estimation, the uncertainty is calculated as a propagating error in division operations ($z = x/y$).

$$\frac{\delta z}{z} = \frac{\delta x}{x} + \frac{\delta y}{y} \tag{A.1}$$

therefore

$$\delta z = z(\frac{\delta x}{x} + \frac{\delta y}{y}) \tag{A.2}$$

The wave propagation velocity, V, which is calculated as the ratio of the distance, h, and the time, t, i.e.

$$V = \frac{h}{t} \tag{A.3}$$

has uncertainty of δV estimated as

$$\delta V = V(\frac{\delta h}{h} + \frac{\delta t}{t}). \tag{A.4}$$

A.3 Polarization results

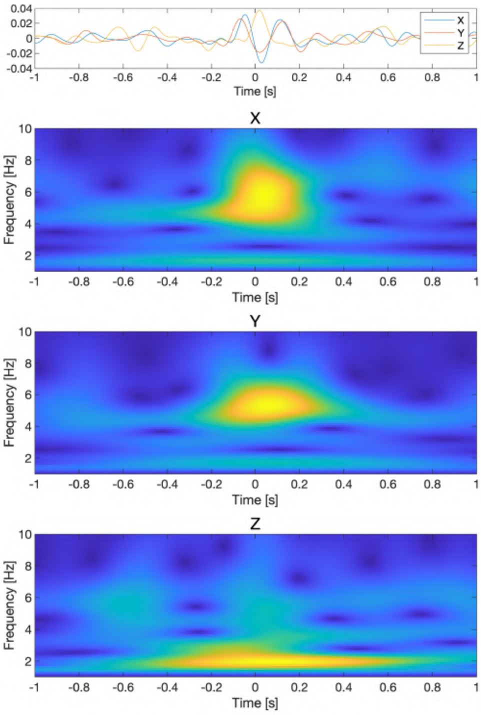

Figure A.1: S-transform of the earthquake deconvolved wavefield of three components (top panel) from sensor 104 in Array 1

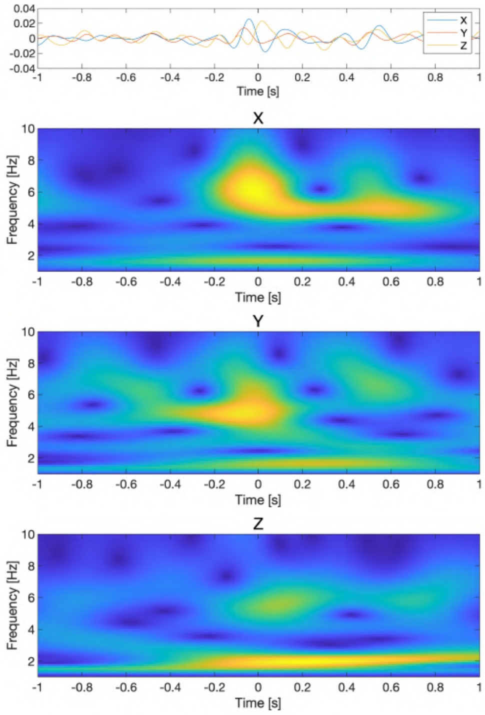

Figure A.2: S-transform of the earthquake deconvolved wavefield of three components (top panel) from sensor 105 in Array 1

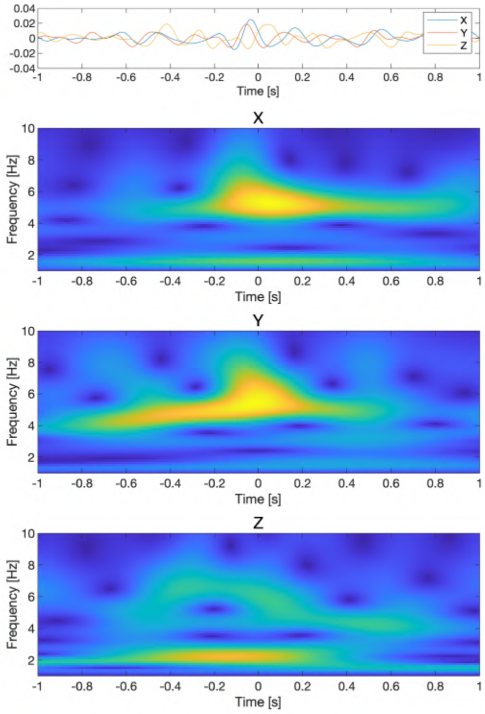

Figure A.3: S-transform of the earthquake deconvolved wavefield of three components (top panel) from sensor 205 in Array 2

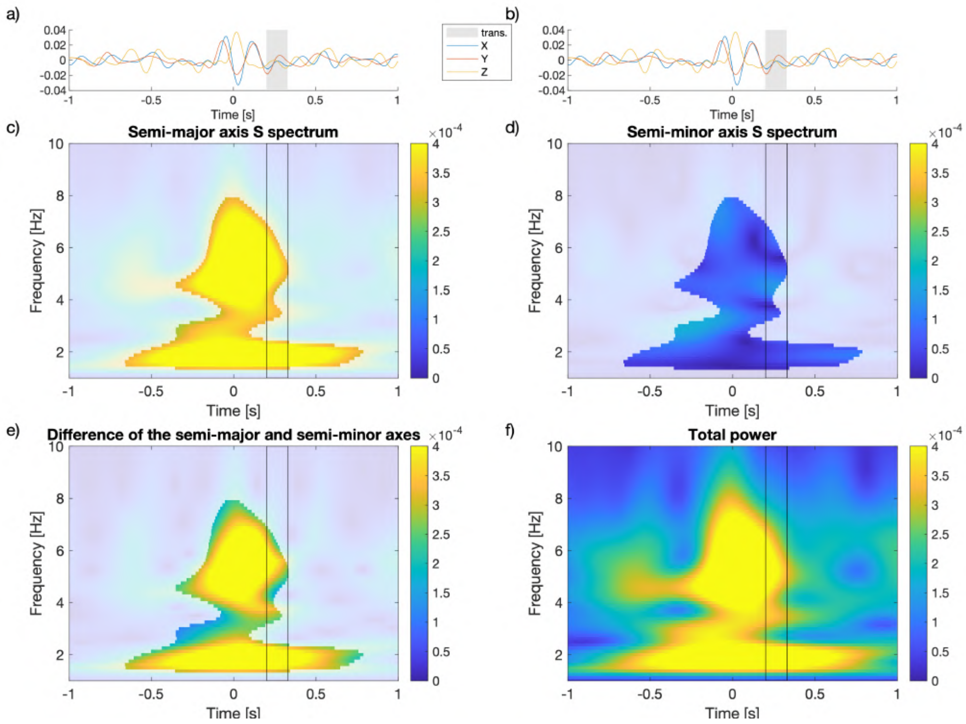

Figure A.4: The ellipse parameters for sensor 104 from Array 1. a-b) the three components of the deconvolved wavefield of the analyzed earthquake used for the analysis. The gray rectangle indicates the considered time interval, corresponding to the seismic phases related to the energy transmitted from the building to its surroundings. c) Semi-major axis S-spectrum. d) Semi-minor axis S-spectrum. e) S-spectrum of the difference between semi-major and semi-minor axes. f) Total power S-spectrum. In time-frequency plots, black thin lines indicate the time interval corresponding to the gray patch from a) and b). The more pronounced colors indicate values where the total power of the S-spectrum (f) is greater than 50 % of the maximum power.

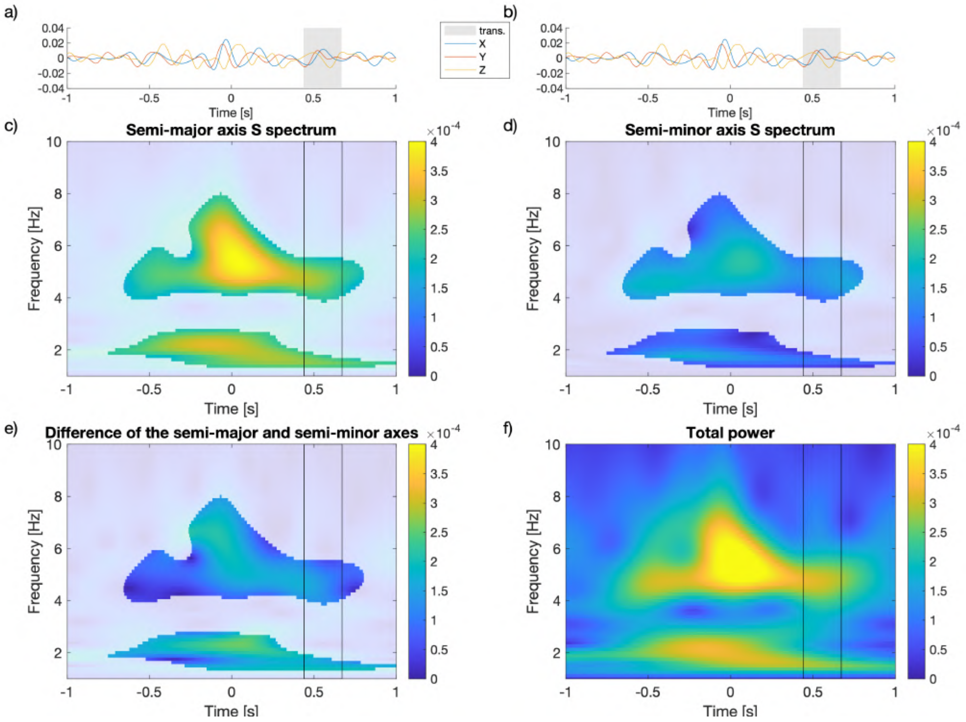

Figure A.5: The ellipse parameters for sensor 205 from Array 2. a-b) the three components of the deconvolved wavefield of the analyzed earthquake used for the analysis. The gray rectangle indicates the considered time interval, corresponding to the seismic phases related to the energy transmitted from the building to its surroundings. c) Semi-major axis S-spectrum. d) Semi-minor axis S-spectrum. e) S-spectrum of the difference between semi-major and semi-minor axes. f) Total power S-spectrum. In time-frequency plots, black thin lines indicate the time interval corresponding to the gray patch from a) and b). The more pronounced colors indicate values where the total power of the S-spectrum (f) is greater than 50 % of the maximum power.

A.4 Particle motion trajectory

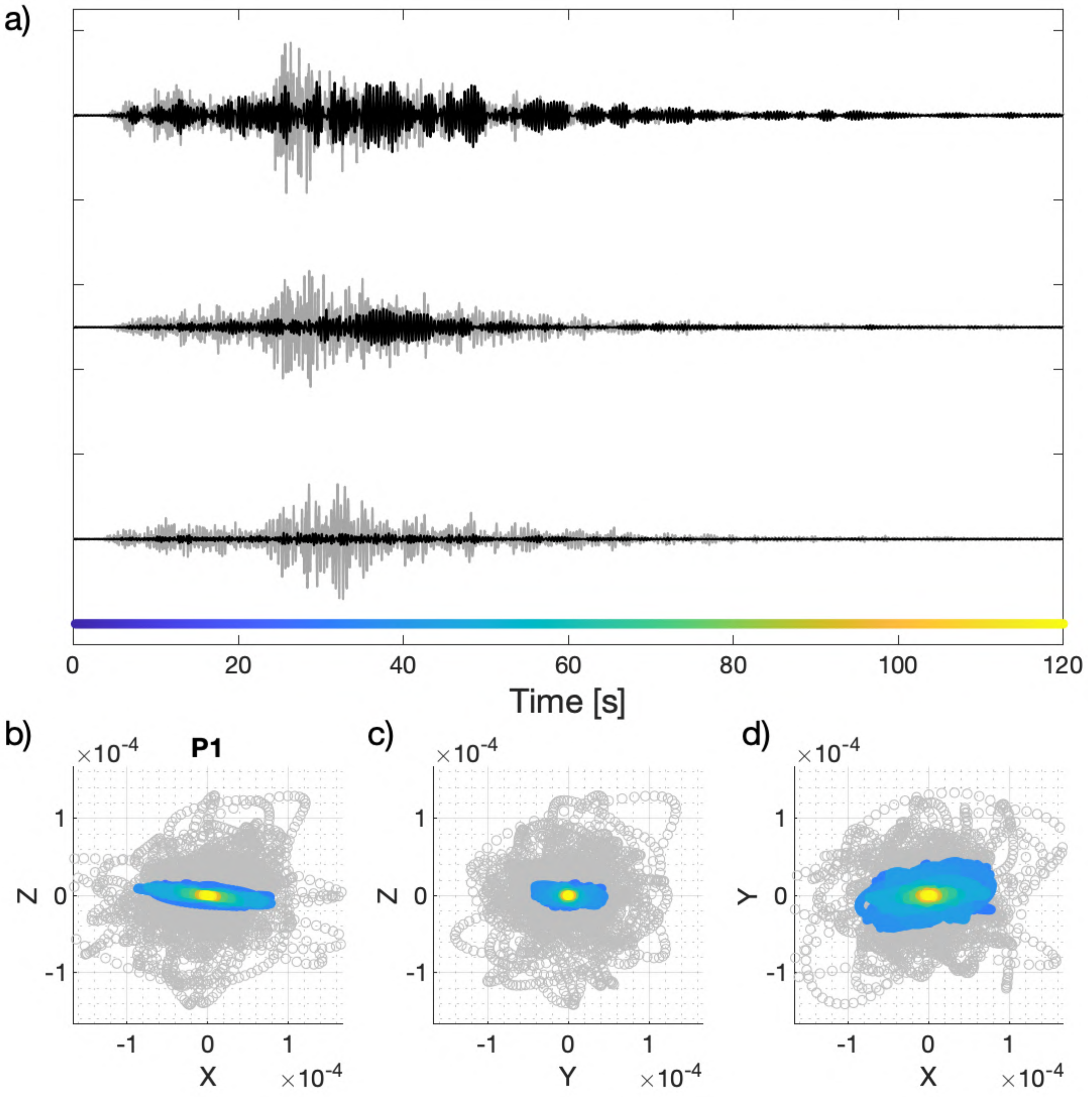

Figure A.6: Particle motion trajectory for sensor 105 from Array 1. a) Time histories of the recorded earthquake signal (gray) and the reconstructed signal radiated from the building to the athletic field (black). b) - j) particle motion in three planes - radial X-Z (b), transverse Y-Z (c), and horizontal X-Y (c). The color scale of the trajectory plots corresponds to the increment of time (from blue to yellow) indicated at the bottom of the time history plot. The gray scatter from b) to c) represents the trajectory of the recorded signal (gray traces in a)).

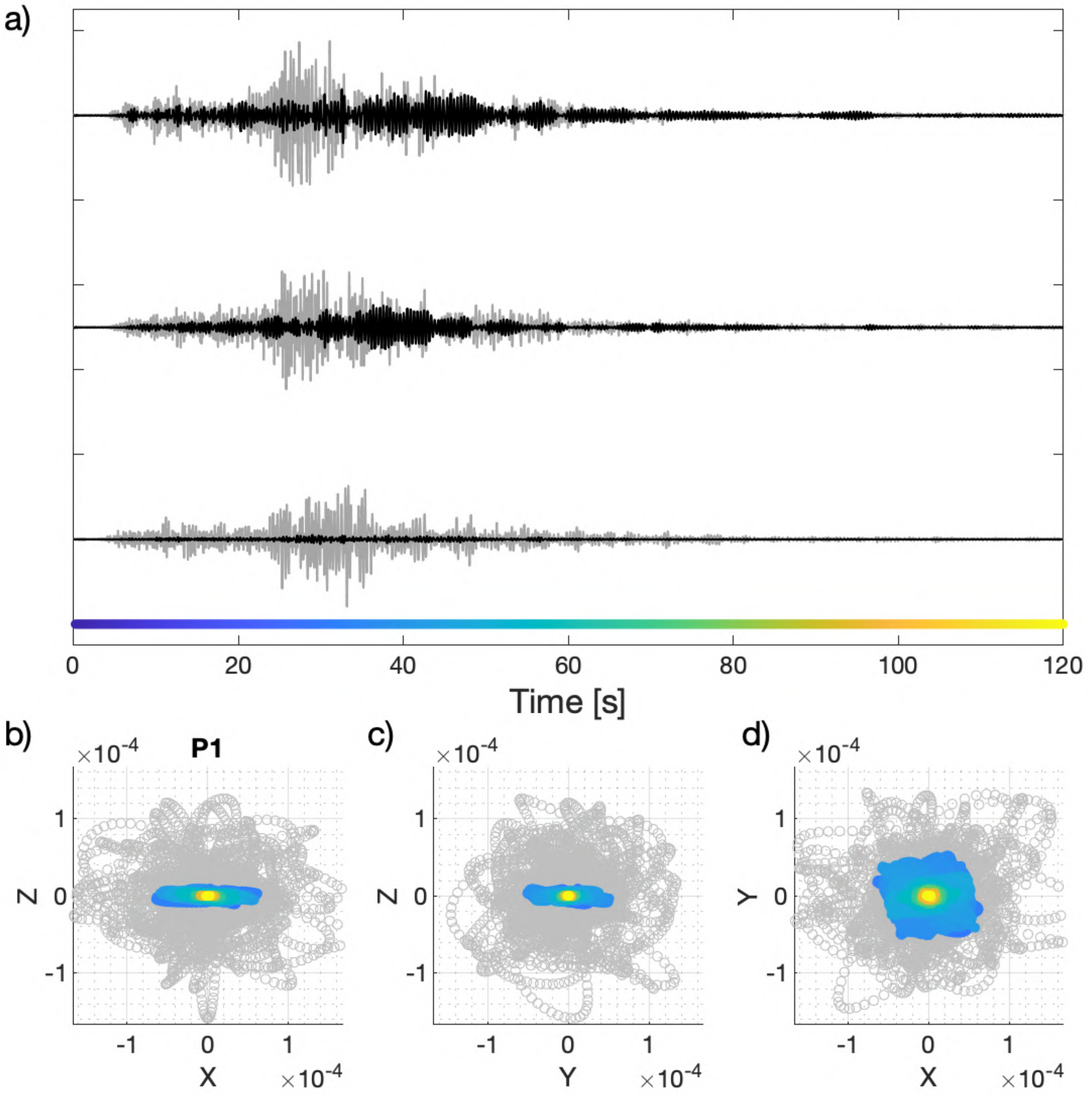

Figure A.7: Particle motion trajectory for sensor 205 from Array 2. a) Time histories of the recorded signal (gray) and the reconstructed signal radiated from the building to the athletic field (black). b) - j) particle motion in three planes - radial X-Z (b), transverse Y-Z (c), and horizontal X-Y (c). The color scale of the trajectory plots corresponds to the increment of time (from blue to yellow) indicated at the bottom of the time history plot. The gray scatter from b) to c) represents the trajectory of the recorded signal (gray traces in a))

A.5 Grid search - Piana di Toppo experiment

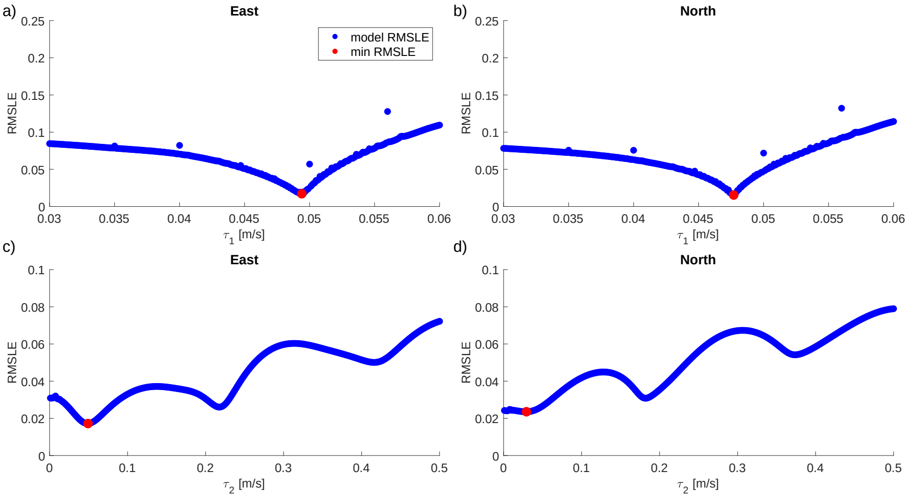

Figure A.8: The grid search results for the East (a,c) and North components (b,d) of sensor 9EAA$_E$ for earthquake A.9 of the Bosnia sequence. a) and b) show grid search of τ_1 from fitting Model 5.14. c) and d) show grid search of τ_2 from fitting Model 6.6. The τ_1 and τ_2 values providing minimum *RMSLE* are indicated with red dots.

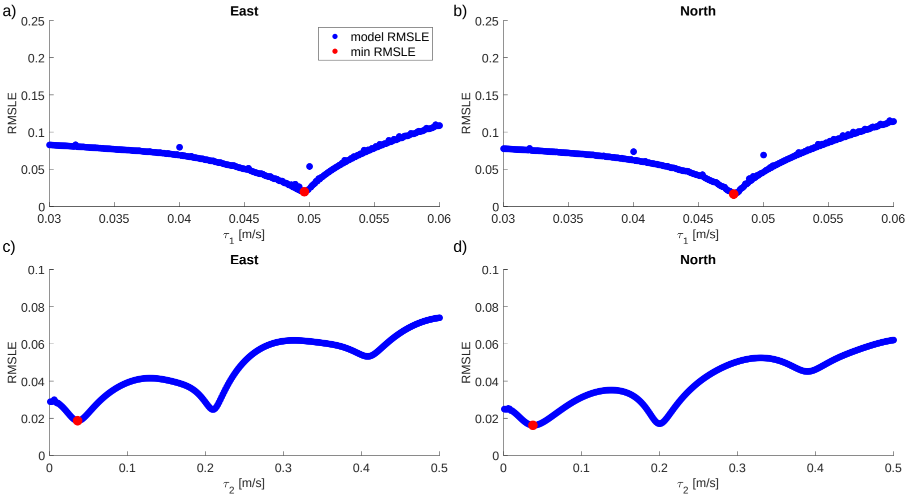

Figure A.9: The grid search results for the East (a,c) and North components (b,d) of sensor 9EAA$_E$ for earthquake A.10 of the Bosnia sequence. a) and b) show grid search of τ_1 from fitting Model 5.14. c) and d) show grid search of τ_2 from fitting Model 6.6. The τ_1 and τ_2 values providing minimum *RMSLE* are indicated with red dots.

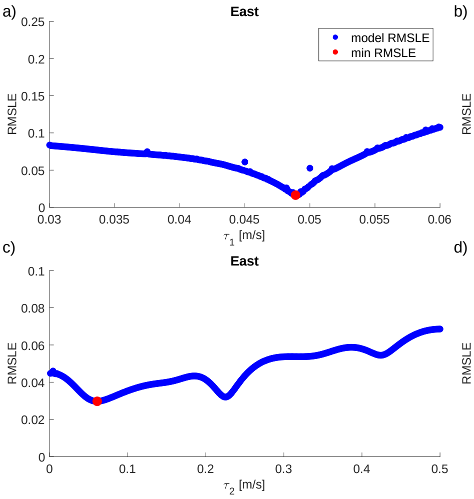

Figure A.10: The grid search results for the East (a,c) and North components (b,d) of sensor $9EAA_E$ for earthquake A.11 of the Bosnia sequence. a) and b) show grid search of τ_1 from fitting Model 5.14. c) and d) show grid search of τ_2 from fitting Model 6.6. The τ_1 and τ_2 values providing minimum $RMSLE$ are indicated with red dots.

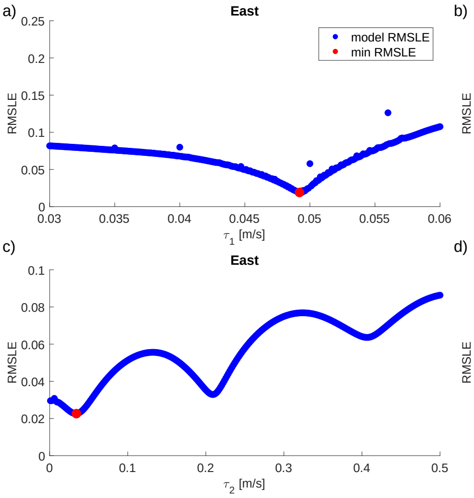

Figure A.11: The grid search results for the East (a,c) and North components (b,d) of sensor $9EAA_E$ for earthquake A.12 of the Bosnia sequence. a) and b) show grid search of τ_1 from fitting Model 5.14. c) and d) show grid search of τ_2 from fitting Model 6.6. The τ_1 and τ_2 values providing minimum $RMSLE$ are indicated with red dots.